

Scientific Research and Essays

Volume 9 Number 6 30 March 2014

ISSN 1992-2248



*Academic
Journals*

ABOUT SRE

The **Scientific Research and Essays (SRE)** is published weekly (one volume per year) by Academic Journals.

Scientific Research and Essays (SRE) is an open access journal with the objective of publishing quality research articles in science, medicine, agriculture and engineering such as Nanotechnology, Climate Change and Global Warming, Air Pollution Management and Electronics etc. All papers published by SRE are blind peer reviewed.

Submission of Manuscript

Submit manuscripts as e-mail attachment to the Editorial Office at: sre@academicjournals.org. A manuscript number will be mailed to the corresponding author shortly after submission.

The Scientific Research and Essays will only accept manuscripts submitted as e-mail attachments.

Please read the **Instructions for Authors** before submitting your manuscript. The manuscript files should be given the last name of the first author.

Editors

Dr. NJ Tonukari

*Editor-in-Chief
Scientific Research and Essays
Academic Journals
E-mail: sre.research.journal@gmail.com*

Dr. M. Sivakumar Ph.D. (Tech).

*Associate Professor
School of Chemical & Environmental Engineering
Faculty of Engineering
University of Nottingham
Jalan Broga, 43500 Semenyih
Selangor Darul Ehsan
Malaysia.*

Prof. N. Mohamed El Sawi Mahmoud

*Department of Biochemistry, Faculty of science,
King AbdulAziz university,
Saudia Arabia.*

Prof. Ali Delice

*Science and Mathematics Education Department,
Atatürk Faculty of Education,
Marmara University,
Turkey.*

Prof. Mira Grdisa

*Rudjer Boskovic Institute, Bijenicka cesta 54,
Croatia.*

Prof. Emmanuel Hala Kwon-Ndung

*Nasarawa State University Keffi Nigeria
PMB 1022 Keffi,
Nasarawa State.
Nigeria.*

Dr. Cyrus Azimi

*Department of Genetics, Cancer Research Center,
Cancer Institute, Tehran University of Medical Sciences,
Keshavarz Blvd.,
Tehran, Iran.*

Dr. Gomez, Nidia Noemi

*National University of San Luis,
Faculty of Chemistry, Biochemistry and Pharmacy,
Laboratory of Molecular Biochemistry Ejercito de los
Andes 950 - 5700 San Luis
Argentina.*

Prof. M. Nageeb Rashed

*Chemistry Department- Faculty of Science, Aswan
South Valley University,
Egypt.*

Dr. John W. Gichuki

*Kenya Marine & Fisheries Research Institute,
Kenya.*

Dr. Wong Leong Sing

*Department of Civil Engineering,
College of Engineering,
Universiti Tenaga Nasional,
Km 7, Jalan Kajang-Puchong,
43009 Kajang, Selangor Darul Ehsan,
Malaysia.*

Prof. Xianyi LI

*College of Mathematics and Computational Science
Shenzhen University
Guangdong, 518060
P.R. China.*

Prof. Mevlut Dogan

*Kocatepe University, Science Faculty,
Physics Dept. Afyon/ Turkey.
Turkey .*

Prof. Kwai-Lin Thong

*Microbiology Division,
Institute of Biological Science,
Faculty of Science, University of Malaya,
50603, Kuala Lumpur,
Malaysia.*

Prof. Xiaocong He

*Faculty of Mechanical and Electrical Engineering,
Kunming University of Science and Technology,
253 Xue Fu Road, Kunming,
P.R. China.*

Prof. Sanjay Misra

*Department of Computer Engineering
School of Information and Communication Technology
Federal University of Technology, Minna,
Nigeria.*

Prof. Burtram C. Fielding Pr.Sci.Nat.

*Department of Medical BioSciences
University of the Western Cape
Private Bag X17
Modderdam Road
Bellville, 7535,
South Africa.*

Prof. Naqib Ullah Khan

*Department of Plant Breeding and Genetics
NWFP Agricultural University Peshawar 25130,
Pakistan*

Editorial Board

Prof. Ahmed M. Soliman

*20 Mansour Mohamed St., Apt 51,
Zamalek, Cairo,
Egypt.*

Prof. Juan José Kasper Zubillaga

*Av. Universidad 1953 Ed. 13 depto 304,
México D.F. 04340,
México.*

Prof. Chau Kwok-wing

*University of Queensland
Instituto Mexicano del Petroleo,
Eje Central Lazaro Cardenas
Mexico D.F.,
Mexico.*

Prof. Raj Senani

*Netaji Subhas Institute of Technology,
Azad Hind Fauj Marg,
Sector 3,
Dwarka, New Delhi 110075,
India.*

Prof. Robin J Law

*Cefas Burnham Laboratory,
Remembrance Avenue Burnham on Crouch,
Essex CM0 8HA,
UK.*

Prof. V. Sundarapandian

*Indian Institute of Information Technology and
Management-Kerala
Park Centre,
Technopark Campus, Kariavattom P.O.,
Thiruvananthapuram-695 581, Kerala,
India.*

Prof. Tzung-Pei Hong

*Department of Electrical Engineering,
and at the Department of Computer Science and
Information Engineering
National University of Kaohsiung.*

Prof. Zulfiqar Ahmed

*Department of Earth Sciences, box 5070,
Kfupm, dhahran - 31261,
Saudi Arabia.*

Prof. Khalifa Saif Al-Jabri

*Department of Civil and Architectural Engineering
College of Engineering,
Sultan Qaboos University
P.O. Box 33, Al-Khod 123, Muscat.*

Prof. V. Sundarapandian

*Indian Institute of Information Technology & Management -
Kerala
Park Centre,
Technopark, Kariavattom P.O.
Thiruvananthapuram-695 581,
Kerala India.*

Prof. Thangavelu Perianan

*Department of Mathematics, Aditanar College,
Tiruchendur-628216 India.*

Prof. Yan-ze Peng

*Department of Mathematics,
Huazhong University of Science and Technology,
Wuhan 430074, P. R.
China.*

Prof. Konstantinos D. Karamanos

*Universite Libre de Bruxelles,
CP 231 Centre of Nonlinear Phenomena
And Complex systems,
CENOLI Boulevard de Triomphe
B-1050,
Brussels, Belgium.*

Prof. Xianyi Li

*School of Mathematics and Physics,
Nanhua University, Hengyang City,
Hunan Province,
P. R. China.*

Dr. K.W. Chau

*Hong Kong Polytechnic University
Department of Civil & Structural Engineering,
Hong Kong Polytechnic University, Hungghom,
Kowloon, Hong Kong,
China.*

Dr. Amadou Gaye

*LPAO-SF / ESP Po Box 5085 Dakar-Fann SENEGAL
University Cheikh Anta Diop Dakar
SENEGAL.*

Prof. Masno Ginting

*P2F-LIPI, Puspiptek-Serpong,
15310 Indonesian Institute of Sciences,
Banten-Indonesia.*

Dr. Ezekiel Olukayode Idowu

*Department of Agricultural Economics,
Obafemi Awolowo University,
Ife-Ife,
Nigeria.*

Fees and Charges: Authors are required to pay a \$550 handling fee. Publication of an article in the Scientific Research and Essays is not contingent upon the author's ability to pay the charges. Neither is acceptance to pay the handling fee a guarantee that the paper will be accepted for publication. Authors may still request (in advance) that the editorial office waive some of the handling fee under special circumstances.

Copyright: © 2012, Academic Journals.

All rights Reserved. In accessing this journal, you agree that you will access the contents for your own personal use but not for any commercial use. Any use and or copies of this Journal in whole or in part must include the customary bibliographic citation, including author attribution, date and article title.

Submission of a manuscript implies: that the work described has not been published before (except in the form of an abstract or as part of a published lecture, or thesis) that it is not under consideration for publication elsewhere; that if and when the manuscript is accepted for publication, the authors agree to automatic transfer of the copyright to the publisher.

Disclaimer of Warranties

In no event shall Academic Journals be liable for any special, incidental, indirect, or consequential damages of any kind arising out of or in connection with the use of the articles or other material derived from the SRE, whether or not advised of the possibility of damage, and on any theory of liability.

This publication is provided "as is" without warranty of any kind, either expressed or implied, including, but not limited to, the implied warranties of merchantability, fitness for a particular purpose, or non-infringement. Descriptions of, or references to, products or publications does not imply endorsement of that product or publication. While every effort is made by Academic Journals to see that no inaccurate or misleading data, opinion or statements appear in this publication, they wish to make it clear that the data and opinions appearing in the articles and advertisements herein are the responsibility of the contributor or advertiser concerned. Academic Journals makes no warranty of any kind, either express or implied, regarding the quality, accuracy, availability, or validity of the data or information in this publication or of any other publication to which it may be linked.

Scientific Research and Essays

Table of Contents: Volume 9 Number 6 30 March, 2014

ARTICLES

Research Articles

- Variational cartographic projections for the Slovak Republic territory** 114
Margita Vajsáblová and Daniel Szatmári
- Experimental study of anaerobic digestion of dog waste** 121
Okoroigwe, E. C., Ibetó, C. N. and Ezema, C. G.
- A Novel SPICE compatible behavioral model for molecular electronics having hysteresis effects** 128
Davoud Bahrepour and Mohammad Javad Sharifi
- Application of statistical techniques to evaluate the reliability of ultrasonic and rebound hammer measurements of compressive strength in the concrete of bridges** 136
C. H. Carvalho, J. B. Severo Junior, M. C. S. S. Macedo, S. Griza, C. E. C. de Andrade, A. A. dos Santos and L. S. Barreto
- Comparative osteometric differences in humerus of bari Goat and Dumbi Sheep** 145
Ghulam Murtaza Lochi, Muhammad Ghiasuddin Shah, Illahi Bux Kalhoro, Jameel Ahmed Gandahi, Muhammad Shoaib Khan, Abdul Haseeb, Sheeraz Mustafa Khushk, Ameet Oad and Mansoor Ibrahim Ansari
- Capacity enhancement of multicarrier code division multiple access (MCCDMA) using orthogonal complete complementary codes and adaptive constellations** 153
G. Senthilkumar and R. Amutha
- Sorption mechanism of some heavy metal ions from aqueous waste solution by polyacrylamide ferric antimonate** 162
I. M. El-Naggar, E. A. Mowafy, Y. F. El-Aryan and M. G. Abd El-Wahed

Full Length Research Paper

Variational cartographic projections for the Slovak Republic territory

Margita Vajsáblová and Daniel Szatmári

Department of Mathematics and Descriptive Geometry, Faculty of Civil Engineering, Slovak University of Technology, Bratislava, Slovak Republic.

Received 3 January, 2014; Accepted 5 March, 2014

Disadvantages of currently used Křovák's projection in Slovak Republic such as large scale distortion became evident after dividing of Czechoslovakia. The new proposal of the cartographic projection for the Slovak Republic (Lambert's conformal conic projection in normal position) was created in 2010. The aim of this paper is to define an optimal oblique position of map projections for the Slovak Republic territory and to design two cartographic projections in different positions (normal, oblique) using variational criteria modified for conformal projections for the Slovak Republic. Used calculus, the achieved scale distortions and their comparison with scale distortions of currently used map projections will be demonstrated.

Key words: Conformal cartographic projection, variational criteria, scale distortion, variational cartographic projection.

INTRODUCTION

The currently used cartographic projection in the Slovak Republic (and also in the Czech Republic) is the Křovák's projection which is an oblique case of a conformal conic projection based on two preserved parallels and was designed in 1922 by Josef Křovák strictly for Czechoslovakia. The Bessel's reference ellipsoid is transformed to a sphere using Gauss' conformal projection. Then, the sphere is transformed to a secant cone in oblique position. The coordinates are positive to the south and west (Srňka, 1986). Disadvantages of this projection such as large scale distortion became evident after dividing of Czechoslovakia. In 2010 a new

projection, Lambert's projection with parameters for Slovakia was designed at the request of the Geodesy, Cartography and Cadastre Authority of the Slovak Republic by Margita Vajsáblová. This new conformal projection uses a normal cone, secant to the reference ellipsoid GRS 1980 and was designed for the Slovak Republic territory (Vajsáblová, 2011). The reference ellipsoid is transformed directly on a secant cone in normal position. The coordinates are positive to the north and east.

One of the basic problems in cartography is the problem of optimal map projections, especially in the area

*Corresponding author. E-mail: margita.vajsablova@stuba.sk. Tel: +421 2 59274406

Author(s) agree that this article remain permanently open access under the terms of the [Creative Commons Attribution License 4.0 International License](https://creativecommons.org/licenses/by/4.0/)

of the creation of large-scale maps and partially medium-scale maps, that is, those projections of a given domain on a reference surface onto the plane under which the distortion is minimal. The most important factors of selection of map projection are shape, size and position of projected territory, also purpose and scaling factor of the map. The aim of this paper is to design two map projections in different positions (normal, oblique) using variational criteria modified for conformal projections for the Slovak Republic. Examples of using these criteria to derive and optimize map projections for other territories (Canada, Czech Republic) and their valuation and comparison are described in Frankich (1982), Bořík (1999) and Hojovec et al. (1975).

The optimal oblique position of cartographic projection for the Slovak Republic territory is defined in this paper and the aim is to design two cartographic projections in different positions (normal, oblique) using variational criteria modified for conformal projections for the Slovak Republic. Used calculus, the achieved scale distortions and their comparison with scale distortions of currently used map projections will be demonstrated.

Valuation of cartographic projections

The type of criteria for deciding the merits of map projections are as follow (Hojovec et al., 1987):

- a) Extremal and minimaximal,
- b) Variational (additive, integral) criteria.

In *extremal criteria* we evaluate conformal projection by:

- i. Maximal value of scale distortion: $|m - 1|_{max}$,
- ii. Maximal value of area distortion: $|m_{pl} - 1|_{max}$.

The equivalent projections are evaluated by maximal value of angle distortion: $|\Delta\omega|_{max}$.

Chebyshev's theorem for conformal projection, in which natural logarithm of scale distortion is the least different from zero, if scale distortion of closed boundary curve is constant (Chebyshev, 1962). These projections are called minimaximal type projections.

Meshcheryakov's theorem for Euler's type projections (orthogonal equivalent): the best of Euler's projection by minimaximal criterion is the projection in which image of the central meridian is a line and the scale distortion in every points holds, that scale distortion of meridian and parallel are equal to 1 (Meshcheryakov, 1968).

The most popularized variational type criteria for valuation of map projections are the following:

- i. The Airy's criterion (1861), where h^2 is mean quadratic scale distortion defined by extremal scale factors m_a, m_b :

$$h^2 = \frac{1}{2} [(m_a - 1)^2 + (m_b - 1)^2], \tag{1}$$

- ii. The Jordan's criterion, which characterizing scale distortion in a point by h^2 for all the azimuths A:

$$h^2 = \frac{1}{2\pi} \int_0^{2\pi} (m_A - 1)^2 dA, \tag{2}$$

in some case for several value of the azimuth A:

$$h^2 = \frac{1}{\mu} \sum (m_A - 1)^2, \tag{3}$$

where m_A is factor of scale distortion appertaining to direction with azimuth A, μ is number of these directions.

- iii. The Kavraiskii's criteria are modification of previous criteria by using the logarithmic values (Kavraiskii, 1959):
 - the Airy-Kavraiskii criterion:

$$h^2 = \frac{1}{2} [\ln^2 m_a + \ln^2 m_b], \tag{4}$$

- the Jordan-Kavraiskii criterion:

$$h^2 = \frac{1}{2\pi} \int_0^{2\pi} \ln^2 m_A dA, \tag{5}$$

$$h^2 = \frac{1}{\mu} \sum \ln^2 m_A. \tag{6}$$

Characteristic value of cartographic projection of domain Δ of reference surfaces is value of integral I:

$$I = \frac{1}{\Delta} \iint_{\Delta} h^2 \cos U dU dV, \tag{7}$$

or for n choices points:

$$I = \frac{1}{n} \sum h^2. \tag{8}$$

Mentioned criteria are possible to use in deriving of cartographic projection too, thereby we obtain variational type of projection (Urmaev, 1947).

The conformal projections are frequently applied in coordinate systems, because in this type of projection holds, that scale distortion is independent to azimuth, we

are able to simplify previous formulae in the next chapters.

Variational cartographic projections

We are concerned with creation of conformal map projections of territory with minimal scale distortion by variational Criterion (7), where we apply the Airy-Kavraisikii Criterion (4) modified for conformal projection ($m_a = m_b = m$):

$$h^2 = \ln^2 m. \tag{9}$$

Projected territory is situated on reference sphere between parallels with geographic latitude U_S, U_N and between meridians with geographic longitude V_W and V_E , where we use their relative value from central meridian V_0 :

$$V_0 = \frac{V_W + V_E}{2}. \tag{10}$$

In consideration of symmetry of spherical trapezium and after substitution of (9) to variational Criterion (7) we obtain:

$$I = \frac{1}{\Delta} \int_0^{V_1} \int_{U_S}^{U_N} \ln^2 m \cos U \, dU \, dV, \tag{11}$$

where V_1 is maximum of relative geographic longitude. We need to find function $\ln m$ from condition that value of I is minimal.

In conformal projection it holds (Hojovec et al. 1975):

$$\frac{\partial^2 u}{\partial Q^2} + \frac{\partial^2 u}{\partial V^2} = 0, \tag{12}$$

where:

$$u = \ln m \cos U \tag{13}$$

and Q is isometric latitude calculated by:

$$Q = \ln \operatorname{tg} \left(\frac{U}{2} + 45^\circ \right). \tag{14}$$

Solution of Equation (12) has a shape (Hojovec et al., 1975):

$$u = \sum_{j=0}^n (a_j \psi_j + b_j \tau_j), \tag{15}$$

where ψ_j and τ_j were determine by:

$$\psi_j + i\tau_j = (Q + iV)^j. \tag{16}$$

Two complex variables are equal than its imaginary and real components are equal, for ψ_j and τ_j we obtain ($j = 0$ to $j = 4$):

$$\begin{aligned} \psi_0 = 1, & \quad \psi_1 = Q, & \quad \psi_2 = Q^2 - V^2, & \quad \psi_3 = Q^3 - 3QV^2, & \quad (17) \\ \psi_4 = Q^4 - 6Q^2V^2 + V^4; & \quad \tau_0 = 0, & \quad \tau_1 = V, & \quad \tau_2 = 2QV, \\ \tau_3 = 3Q^2V - V^3, & & \quad \tau_4 = 4Q^3V - 4QV^3. & & \end{aligned}$$

Equation (15) is simplified for symmetric:

$$u = \sum_{j=0}^n a_j \psi_j. \tag{18}$$

After substitution Equations (13) and (18) to Airy-Kavraisikii criterion (11) we have:

$$I = \frac{1}{\Delta} \int_0^{V_1} \int_{U_S}^{U_N} \left(\sum_{j=0}^4 a_j \psi_j - \ln \cos U \right)^2 \cos U \, dU \, dV. \tag{19}$$

By minimalisation of (19) we obtain system of five equations for $j = 0$ to 4, where j is:

$$a_0 P_{j0} + a_1 P_{j1} + a_2 P_{j2} + a_3 P_{j3} + a_4 P_{j4} = F_j, \tag{20}$$

where functions P and F hold (Hojovec et al. 1975):

$$P_{jk} = \int_0^{V_1} \int_{U_S}^{U_N} \psi_j \psi_k \cos U \, dU \, dV, \quad F_k = \int_0^{V_1} \int_{U_S}^{U_N} \psi_k \cos U \ln \cos U \, dU \, dV. \tag{21}$$

The coefficients a_j are calculated for domain defined by marginal parallels U_S, U_N and meridians $0^\circ, V_1$. The factor of scale distortion is calculated by:

$$\ln m = \sum_{j=0}^4 a_j \psi_j - \ln \cos U. \tag{22}$$

Proposal of two variational cartographic projections for the Slovak Republic

The geographic coordinates φ, λ of the boundary points of the Slovak Republic on reference ellipsoid GRS 1980,

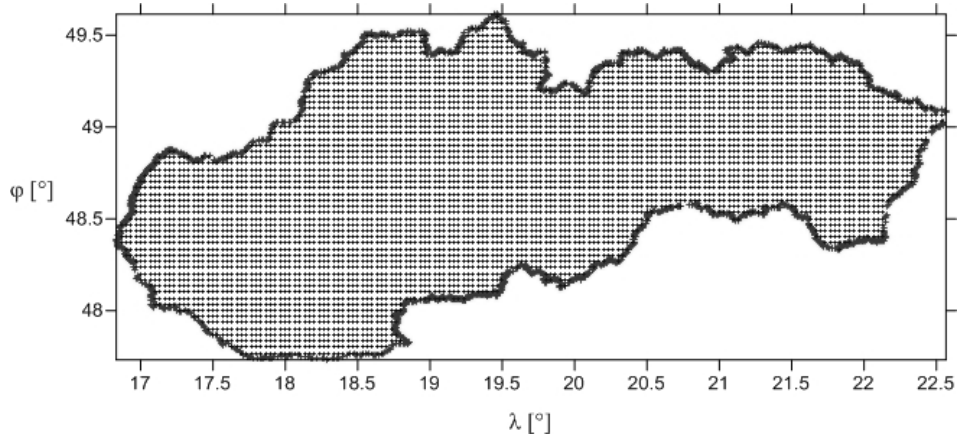


Figure 1. Test points for calculating the factor of scale distortion.

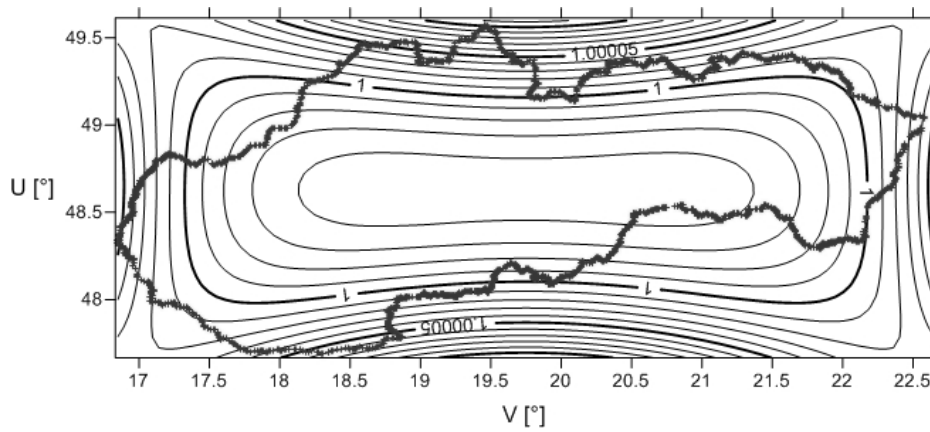


Figure 2. Curves of constant scale distortion – normal case of variational cartographic projection.

we have transformed on the spherical coordinates U, V by Gauss` conformal projection:

$$\operatorname{tg}\left(\frac{U}{2} + 45^\circ\right) = k \left[\operatorname{tg}\left(\frac{U}{2} + 45^\circ\right) \sqrt{\frac{1 - e \sin \varphi}{1 + e \sin \varphi}} \right]^\alpha, \quad V = \alpha \cdot \lambda. \quad (23)$$

with parameters: $\alpha = 1.000\ 640\ 596\ 750\ 5$ and $k = 1.003\ 315\ 995\ 637\ 3$.

Preserved parallel has geographic latitude $\varphi_0 = 48^\circ\ 40'\ 21.2520''$ and radius of the sphere is $R = 6\ 380\ 840.721\ 3\ \text{m}$.

The Slovak Republic is situated on this sphere between parallels with geographic latitude $U_S = 47^\circ\ 41'\ 27.0720''$, $U_N = 49^\circ\ 34'\ 15.7881''$ and between meridians with geographic longitude $V_W = 16^\circ\ 50'\ 32.3600''$ and $V_E = 22^\circ\ 34'\ 50.6852''$, where we have used their relative

values from central meridian V_0 calculated as the arithmetic mean (10).

Values of evaluated coefficients a_j for the first domain defined by marginal parallels U_S, U_N and meridians $0^\circ, V_1$ and with using Equations (11) to (21) are:

$$a_0 = +17.334734, \quad a_1 = -70.610239, \quad a_2 = +107.550822, \\ a_3 = -73.595801, \quad a_4 = +18.886817.$$

All of the calculus has been realized by system *Wolfram Mathematica 8*. We have calculated the factor of scale distortion for 5 424 points (Figure 1) by Equation (22), the curves of constant scale distortion have been visualized in *Surfer 9* (Figure 2).

The second variational projection is proposed in oblique position, therefore on domain defined on reference sphere between two cartographic parallels with

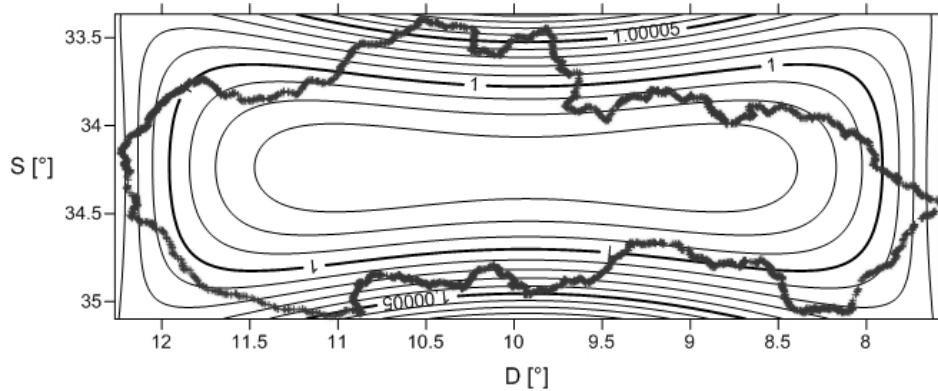


Figure 3. Curves of constant scale distortion – oblique case of variational cartographic projection.

cartographic latitude S_S, S_N and two cartographic meridians with cartographic longitude D_W, D_E . We have defined the values of this cartographic coordinates by consecutive steps:

1st We have chosen three points A, B, C on the south boundary of the Slovak Republic with geographic coordinates:

- $A [U_1 = 48^\circ 19' 49.9601'' , V_1 = 22^\circ 05' 58.6244'']$,
- $B [U_2 = 48^\circ 17' 28.5876'' , V_2 = 21^\circ 49' 51.4052'']$,
- $C [U_3 = 47^\circ 42' 47.2572'' , V_3 = 18^\circ 30' 50.1205'']$.

2nd We have approximated the cartographic parallel circle through the points A, B, C and have calculated the geographic coordinates U_K and V_K of cartographic pole K by equation:

$$\begin{aligned} \operatorname{tg} V_k &= \frac{(\cos U_1 \cos V_1 - \cos U_3 \cos V_3)(\sin U_1 - \sin U_2) - \dots}{(\cos U_1 \sin V_1 - \cos U_2 \sin V_2)(\sin U_1 - \sin U_3) - \dots} \\ &\dots \frac{-(\cos U_1 \cos V_1 - \cos U_2 \cos V_2)(\sin U_1 - \sin U_3)}{-(\cos U_1 \sin V_1 - \cos U_3 \sin V_3)(\sin U_1 - \sin U_2)}, \quad (24) \\ \operatorname{tg} U_k &= \frac{\cos U_2 \cos(V_k - V_2) - \cos U_1 \cos(V_k - V_1)}{\sin U_1 - \sin U_2}. \end{aligned}$$

from that $U_K = -5^\circ 53' 41.1964''$ and $V_K = 32^\circ 08' 18.5219''$.

3rd Then we have transformed geographic coordinates U, V of the points of Slovakia boundary on cartographic coordinates S, D . Extremal values of cartographic latitudes S_S, S_N and cartographic longitudes D_W, D_E are the coordinates of marginal parallels and marginal meridians of boundary trapezium. The Slovak Republic is situated on the sphere between parallels with

cartographic latitude $S_S = 35^\circ 05' 05.7509''$, $S_N = 33^\circ 23' 42.1307''$ and between meridians with cartographic longitude $D_W = 12^\circ 13' 59.6088''$, $D_E = 7^\circ 34' 55.6498''$, where we have used their relative values from central meridian D_0 calculated as the arithmetic mean:

$$D_0 = \frac{D_W + D_E}{2}, \quad (25)$$

from where the maximal value of relative cartographic longitude is D_1 . The interval of latitudes is $1^\circ 52' 48.7161''$ in normal position, $1^\circ 41' 23.6202''$ in oblique position.

The coefficients a_j have been evaluated for the second domain defined by marginal parallels S_S, S_N and meridians $0^\circ, D_1$ by Equations (11) to (21) where the following substitutions have been used:

$$U = S, \quad V = D, \quad U_S = S_S, \quad U_N = S_N, \quad V_1 = D_1. \quad (26)$$

Results of coefficients a_j :

$$\begin{aligned} a_0 &= +6.800198, \quad a_1 = -42.196398, \quad a_2 = +98.029304, \\ a_3 &= -102.608260, \quad a_4 = +40.284538. \end{aligned}$$

All the calculus have been realized by system *Wolfram Mathematica 8*. We have calculated the factor of scale distortion for 5 424 points (Figure 1) by Equation (22) where $U = S$, the curves of constant scale distortion have been visualized in *Surfer 9* (Figure 3).

We have compared these variational cartographic projections with the currently used projection defined by the law – Křivák’s projection (Srňka, 1986). The Křivák’s projection is an oblique case of conformal conic projection based on two preserved parallels designed in

Table 1. Extremal scale distortions in cartographic projections.

Cartographic projection	Scale distortion [cm/km]
Variational – normal	From -4.6 to +9.7
Variational – oblique	From -3.8 to +7.2
Křovák	From -10.0 to +11.0
Lambert	From -6.7 to +6.7

Table 2. Scale distortions and their quadratic values in cartographic projections by additive criterion.

Cartographic projection	Additive criterion	
	cm ² /km ²	\sqrt{I} [cm/km]
Variational – normal	8.667	2.944
Variational – oblique	6.076	2.465
Křovák	51.125	7.150
Lambert	25.489	5.049

Table 3. Scale distortions and their quadratic values in cartographic projections by integral criterion.

Cartographic projection	Integral criterion	
	cm ² /km ²	\sqrt{I} [cm/km]
Variational – normal	8.709	2.951
Variational – oblique	6.131	2.476
Křovák	48.375	6.955
Lambert	26.211	5.120

1922 by Josef Křovák. Used in the Czech Republic and Slovakia. In 2010 a new projection, Lambert's projection with parameters for Slovakia (Vajsáblová, 2011) was designed at the request of the Geodesy, Cartography and Cadastre Authority of the Slovak Republic. This new conformal projection uses a normal cone, secant to the reference ellipsoid and was designed for the Slovak Republic territory by Margita Vajsáblová. The results are demonstrated in Tables 1 to 3. The valuation of scale distortions and their quadratic values in the mentioned cartographic projections by additive criterion has been calculated by Equation (8) for $n = 5\,424$ points (Table 2) and by integral criterion by Equation (7), where region Δ is limited by boundaries of the Slovak Republic (Table 3).

Conclusions

Disadvantages of currently used Křovák's projection such as large scale distortion became evident after dissolution of Czechoslovakia. The maximal scale distortion of this projection is about 4.3 cm/km larger than scale distortion

of Lambert's projection with parameters for the Slovak Republic also about 3.8 cm/km larger than scale distortion of oblique variational projection. Valuation of these map projections by variational criteria (additive or integral) demonstrated in the Tables 2 and 3 also confirms their suitability.

The most suitable cartographic projection of territory of the Slovak Republic by extremal criteria is the Lambert's projection with parameters for the Slovak Republic. The most suitable map projection by variational criteria is the above described variational projection in oblique position.

Conflict of Interests

The author(s) have not declared any conflict of interests.

ACKNOWLEDGEMENT

This article is one of the outputs of the 1/1063/11 project

supported by the VEGA Grant Agency.

REFERENCES

- Airy GB (1861). Explanation of a projection by balance of errors for maps applying to a very large extent of the Earth's surface and comparison with other projections. *Philosophical Magaz. J. Sci.* 22:409-421.
- Bořík M (1999). Using of variational criteria for projection of CR. Map – product of geoinformatic technologies: Proceedings of the 13th Cartographic Conference. Bratislava. pp. 37-42.
- Chebyshev PL (1962). *Sur la construction des cartes géographiques. Oeuvres de P.L. Chebyshev.* Chelsea.
- Frankich K (1982). Optimization of geographic map projections for Canadian territory, Simon Fraser University, Canada.
- Hojovec V, Klášterka J, Rendlová H (1975). Using of Chebyshev's variational criterion in conformal projection. *Geodetic cartographic Rev.* 21(63):3-6.
- Hojovec V, Daniš M, Hájek M, Veverka B (1987). *Cartography.* Praha (Geodetic and Cartographic Enterprise).
- Kavraiskii VV (1959). *Collected works 2.* Moscow.
- Meshcheryakov GA (1968). *Theoretical foundations of mathematical cartography.* Moscow.
- Srnka E (1986). *Mathematical cartography.* Military Academy of Antonín Zápotocký, Brno.
- Urmaev NA (1947). *Methods for finding new cartographic projections.* Moscow.
- Vajsáblová M (2011). Proposal of new cartographic projection of Slovak Republic. *Geodetic and cartographic Rev.* 57(99):185-190.

Full Length Research Paper

Experimental study of anaerobic digestion of dog waste

Okoroigwe, E. C.*, Ibeto, C. N. and Ezema, C. G.

National Centre for Energy Research and Development, University of Nigeria, Nsukka, Enugu State, Nigeria.

Received 07 October, 2013; Accepted 10 March, 2014

Bioconversion of dog waste (dung) to energy as one of the ways for proper disposal of the waste was carried out through anaerobic digestion for biogas production. The 59-day experiment was performed within the slurry temperature range of 28 and 44°C using a 50 L metallic biodigester. Prior to charging the digesters, physico-chemical properties and microbial content of the waste were determined using standard methods. The results show that a cumulative gas production of 200 L was generated by 7 kg of the waste at the end of the test period while the microbial load decreased from 8.2×10^{14} at the beginning of the test to 4.2×10^8 at the end of the retention time. Five microorganisms were identified at the beginning of the charging period, four were identified at the 20th day when the gas began to burn due to methane production while only one microorganism was identified at end of the test. Even though it has longer retention period than most common animal wastes used for biogas production, its gas production rate is low. However, pathogen reduction through anaerobic digestion justifies its conversion to energy by this method.

Key words: Dog Waste, biogas, anaerobic digestion, renewable energy, biodigesters, microbial count.

INTRODUCTION

Proper waste management is an issue in developing countries. Diseases and sicknesses are associated with improper waste handling and disposal. One of the ways of preserving the environment which is being affected by global warming due to heavy consumption of fossil fuels is by use of alternative renewable energy fuels. By this, ground water contamination, diseases and sicknesses as well as air pollution are abated.

Biomass technology has become one of the sources of renewable energy fuels for the present and future energy use that will help reduce the level of environmental pollution resulting from use of fossil fuels and improper waste disposal. It is widely used as source of biomass energy for cooking, heating and electricity generation for

lighting and running of internal combustion (IC) engines.

Biomass is accumulation of solar energy on earth in the form of plant and animal materials. Dog waste (excreta) is easily found littering the environment in developing countries due to poor handling and ignorance of its usefulness in energy production. Dog rearing is common among individuals and organizations as pet and for security purposes.

Bacteria and pathogens are associated with dog wastes (Beck, 1979) which are harmful to human health (Unruh et al., 1973). Of greatest concern here are parasitic worms, round worms, hookworms and tape worms (Prociv and Croese, 1990).

Composting is discouraged as a method of disposal of

*Corresponding author. E-mail: edmund.okoroigwe@unn.edu.ng. Tel: +234-8057156223.

Author(s) agree that this article remain permanently open access under the terms of the [Creative Commons Attribution License 4.0 International License](http://creativecommons.org/licenses/by/4.0/)



Figure 1. Biodigester prototype used in the experiment.

dog waste due to its pathogen content. It contains bacteria and pathogens that are harmful to humans. Like other animal manures, dog manure has high nitrogen content which increases its carbon to nitrogen ratio hence affecting the decomposition process (Taylor, 2004). Rather than allowing dog dung waste away, its energy potential is being explored. Animal waste is being screened to see how it might be reused in a bid to making the environment clean. Usually, if dog waste is not tossed out, it is left where it falls and dissolves into the ground where it flows untreated into the water table. Another common method of its disposal is by scooping into compost bin alongside the yard waste which can be regarded as poor method of disposal due to its susceptibility to human disease.

In this work it is proposed that one of the ways to get rid of the menace of dog dung is by anaerobic digestion for medium energy fuel production. Anaerobic digestion is the microbial decomposition of biomass in the absence of oxygen. The major product of this bacterial activity is the release of biogas, a combustible gas that is rich in methane and contains carbon dioxide, water and hydrogen sulphide in trace quantity. Anaerobic digestion of different animal wastes has been carried out by many scholars. Abubakar and Ismail (2012) have carried out an investigation on biogas production potential of cow dung using a laboratory scale 10 L bioreactor. It was found that cow dung stands a promising feedstock for biogas production even at a laboratory scale. Three wastes types comprising cow dung, cowpea and cassava peels have also been subjected to anaerobic digestion (AD) investigation by Ukpai and Nnabuchi (2012). In their work cowpea produced highest percentage of methane followed by cow dung while the cassava peels produced the least. On cumulative scale, cow dung produced the highest cumulative biogas yield of 124.3 L/total mass of slurry. At domestic level, 11 m³ biodigester has been operated at National centre for Energy Research and Development, University of Nigeria Nsukka using cow

dung as feedstock (Eze et al., 2011). At full capacity, the biogas generated from cow dung using this digester is capable of producing energy required for up to 6 h of household continuous cooking. In Nepal, Singh et al. (2008) have demonstrated the use of poultry waste in biogas production. It was found that poultry droppings could provide additional energy required for the farm operation if anaerobic digestion is incorporated in the management of the wastes. Biogas generation from animal wastes is not limited to domestic or farm animals. Atanu et al. (2010) carried out laboratory experiment on biogas generation from AD of elephant droppings. It was found that this waste can produce biogas containing 48 to 60% methane even though biogas generation did not start until after 12 days of fermentation.

A survey of scholarly articles show several works done on biogas generation using plant, animal and industrial wastes with little or no information on use of dog wastes for energy production. In the review of current advances in biogas production, provided by Demirel et al. (2010), dog waste is not mentioned as one of the wastes that could generate energy. Among all the animal wastes used so far for biogas production at both laboratory and field experiments, AD of dog waste is scarcely reported. This may be partly because of the quantity of the waste or partly because of its susceptibility to pathogens. Therefore it becomes important that biogas production potential of this waste be investigated with a view to advising for its proper disposal. Anaerobic digestion of animal wastes has been found to have a long time benefit. In some cases Anaerobic digestion processes have often been applied for biological stabilization of solid and liquid wastes (Demirel et al., 2010). Similarly, it has been found that the slurry (effluent) can be used in crop production as biofertilizer which has better nutrient quality than the raw waste (Okoroigwe, 2007; Okoroigwe et al., 2008). The aim of this investigation is to determine the biogas production potential of dog waste. The work will understudy the bacterial count of the digested effluent with a view to advising for its proper disposal.

MATERIALS AND METHODS

In this study, the dog waste (dung) used was collected from the dog unit of University of Nigeria, Nsukka security post and Department of Veterinary Medicine while the anaerobic digestion experiment was carried out at the National Centre for Energy Research and Development, (NCERD), University of Nigeria Nsukka. Prior to biodigestion process, proximate analysis of the waste was carried out using standard methods to determine the moisture and ash content. Physicochemical properties such as pH, temperature, crude fibre, protein, fat etc were also determined prior and during the biodigestion period. The action of microorganisms in the decomposition process of the substrate is very important to determine the progress of biogas production. Hence, the microbial load of the substrate was determined at three different periods during the biodigestion process. This was determined using the surface viable count method outlined by Okore (2004). After determination of preliminary parameters of the substrate, the AD proceeded with the charging of the 50 L biodigester (Figure 1) with

Table 1. Result of proximate analysis.

Parameter	%
Moisture	74.8
Ash	1.50
Protein	2.19
Fat	0.15
Fibre	0.55
Total solids	25.2
Volatile solids	20.5
Potassium	1.50
Calcium	0.06
Magnesium	0.32
Phosphorus (mg/100 g)	0.48
Carbon	2.98
Nitrogen	0.175
C:N ratio	17.0
Onset of flammability	20 th day

7 kg of dog dung mixed in 21 kg of water. The set up was made airtight to ensure anaerobic condition and kept in an open space at the biomass digestion ground of NCERD. This was to ensure that the set up was operated at the normal prevailing environmental conditions of temperature and pressure. The 59 day experiment lasted from December 2008 to January 2009.

Biogas generated was measured daily at specific time of the day to ensure 24 h gas production period. The volume of gas in liters was measured by downward displacement of water in a trough calibrated in 0.5 L scale.

The gas production rate was calculated according to the relation:

$$S_g = \frac{V_g}{R_t} \quad (1)$$

Where, S_g = gas production ($L \cdot day^{-1}$); V_g = cumulative gas production (L), and R_t = retention time (days)

RESULTS AND DISCUSSION

Physico-chemical parameters

The physical and chemical parameters of the sample as determined through the analysis above are presented in Table 1.

C/N ratio

Among factors that affect biogas yield from AD of wastes are pH, Hydraulic Retention Time and C/N ratio (Oparaku et al., 2013; Yadvika et al., 2004). According to Wang et al. (2012), C/N ratio is an important indicator for controlling biological treatment systems. High C/N ratio indicates rapid nitrogen consumption by methanogens and leads to lower gas production while low C/N ratio

results in ammonia accumulation and an increase in pH values, which is toxic to methanogenic bacteria (Zhang et al., 2013). Usually, during anaerobic digestion, microorganisms utilize carbon 25 to 30 times faster than nitrogen (Yadvika et al., 2004). To meet this requirement, microbes need a 20 to 30:1 ratio of C to N). The characterization result of the dog waste sample shows that it contains a CN ratio of 17. This is small compared to the recommended ratio above. This could be responsible for the low gas production within the first 20 days of digestion (Figure 2). This is also responsible for the acidic nature of the slurry during the initial days (Figure 3).

Flammability/methane content

Flammability (evidence of methane content) started at the 20th day which presumes that ammonia production due to low CN ratio might be predominant at early digestion days. This delay period was also obtained by Ofoefule and Uzodimma (2009) in the blend of cassava peels waste with pig dung in anaerobic digestion process. The explanation is also based on large ammonia production from cassava peels digestion.

Effect of volatile solids and total solids (VS and TS)

The result also shows that the waste has a volatile solid concentration of 20.5% and total solid concentration of 25.2% in the dung (Table 1). This shows the amount of the dung convertible to gaseous element and providing nutrients to the microorganisms for their function. The low VS contributed, along other parameters, to the low gas yield recorded in the first 20 days since the microbes could not breakdown the substrate as easily as possible. Gas yield increased from the 25th day when there was a balance between the TS consumption and VS conversion to gas. The 25.2% TS and 74.2% moisture content of the dog waste are close to 20 and 80% respectively for human excreta due to the nature of diet dogs feed on.

Biogas yield

The biogas yield profile of the substrate (Figure 2) is typical of biogas production profile from anaerobic digestion of animal wastes. The profile is characterized by fluctuation in biogas production over time due to many factors which include complex microbial activities. The processes of AD are complex chemical reactions between the microorganisms and the substrates which are affected by a number of factors as indicated above and the prevailing climatic and environmental factors. Temperature affects the reaction resulting in changes in biogas yield. The result of the daily gas yield of the dog waste is shown in Figure 2 while the cumulative biogas

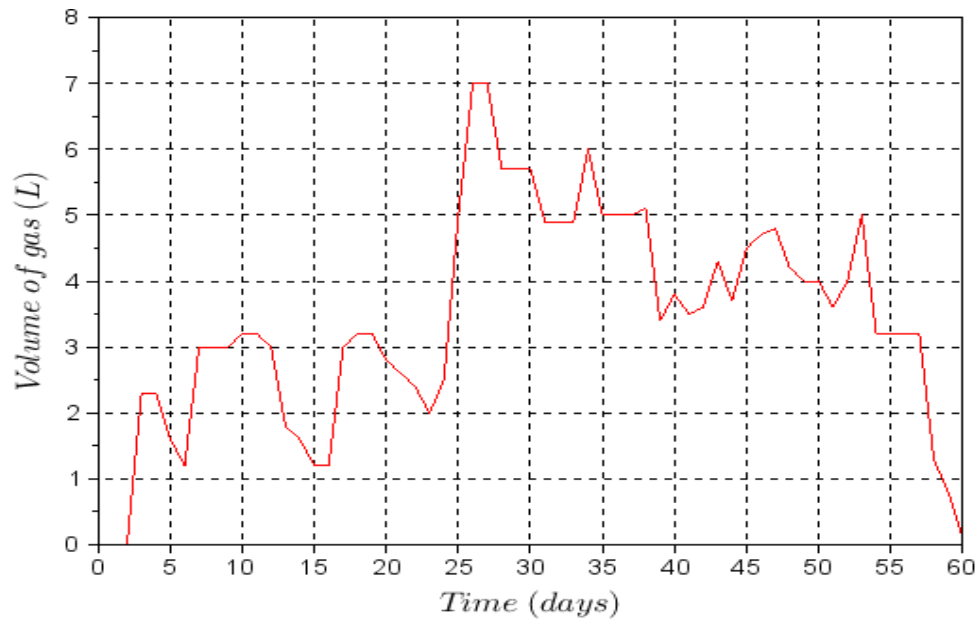


Figure 2. Daily biogas production from the dog waste.* is converted by authors from the original source.

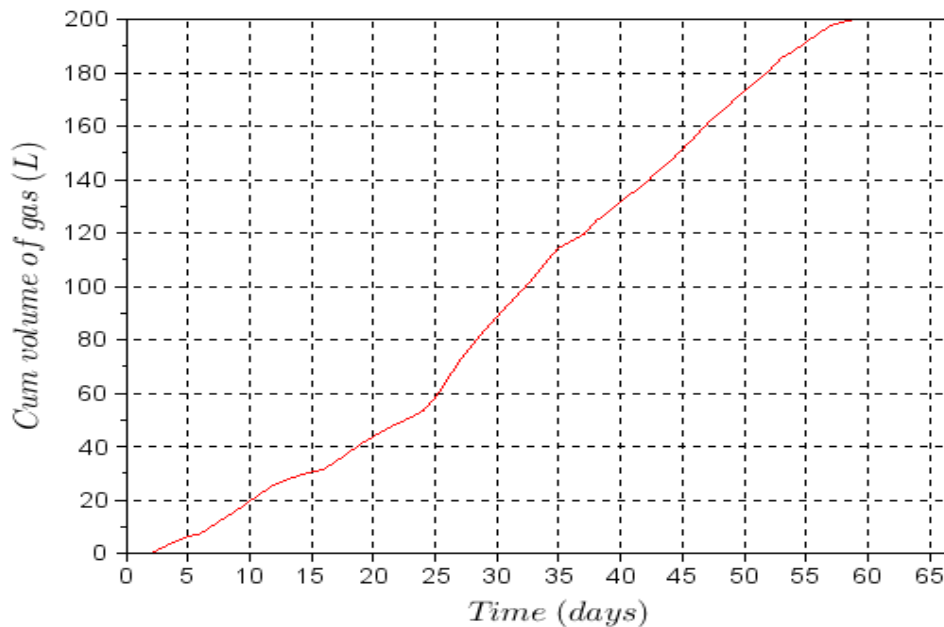


Figure 3. Cumulative biogas production of the dog waste.

production over the entire biodegradation period is shown in Figure 3. The gas production rate is calculated as 0.07 L/day using Equation (1). On unit mass of substrate, the gas production specific volume yield (SVY) is 28.57 L/kg, or 0.029 m³/kg. This value is similar to 0.028 m³/kg reported by Balasubramaniyam et al. (2008) for human excreta. This could be because both animal wastes type

have similar physico-chemical properties. The dog's biogas SVY is less than 0.3, 0.5 and 0.5 m³/kg reported by Ilaboya et al. (2010) for Cattle dung, Pig dung and Poultry droppings respectively. Since human waste has been used for biogas production, dog waste can be used also. An advantage of using dog dung for biogas production is on its long retention time as gas production

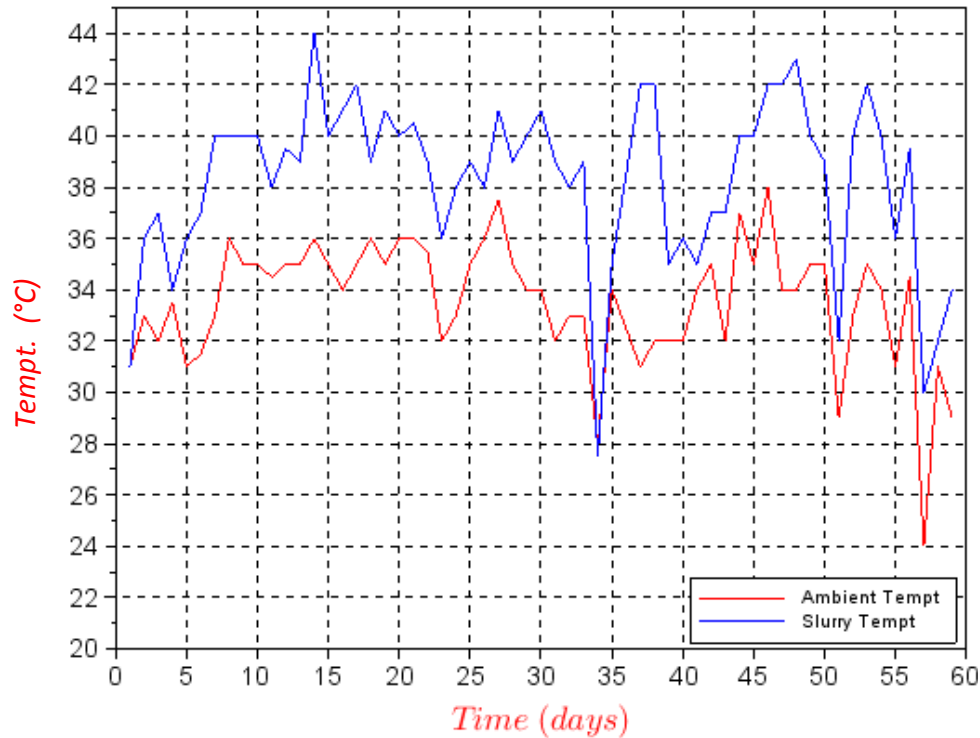


Figure 4. Temperature variation during the biodigestion period.

continued up to 59th day. The quantity of dog waste product is a limitation in using this for large biogas production.

For the 59-day testing of the wastes, a total of 200 L of gas were collected.

Temperature effect

Figure 4 shows the temperature variation during the test period. The slurry temperature was between 28 and 44°C which is the mesophilic temperature regime. There was no external influence of the slurry temperature as this was only affected by the activities of microorganisms. The external temperature (ambient) was only influenced by natural weather condition. The period was during the harmatan wind characterized by dryness and cold wind across Sahara. The highest ambient temperature was 38°C while the lowest was 24°C. This condition is favourable for biogas production during AD of animal wastes unlike adverse cold witnessed during winter in temperate climate when the temperature assumes negative values.

pH variation

The pH of the slurry ranged from 6.36 to 7.78 as shown in Figure 5. The microorganisms that are involved in

biodigestion processes are usually affected by the acidity of the medium. The activities of these acidogens and methanogens result in the variation of pH of the medium and subsequently affect biogas production. Optimum biogas production is usually obtained within the pH range of 6.5 to 7.5. Maximum gas production was obtained between the 25th and the 35th day (Figure 2) when the pH was near neutral (Figure 5).

Microbial load

Table 2 presents the type and number of microorganisms in the waste at major times of the analysis. It shows that the waste had higher microorganism content at the beginning which was a combination of aerobic and anaerobic organisms. At flaming period the organisms (*Butyrivibrio* sp.) were no longer present which was responsible for the decrease in the microbial count (TVC) of the identified organisms. These were responsible for aerobic activities that utilized initial oxygen trapped in the system at commencement of fermentation. When methane began to build up *Clostridium* sp., *Ruminococcus* sp., *Acetivibrio* sp. and *Eubacterium-cellulosolvens* were predominant. It could be affirmed that methane production could be hindered as long as *Butyrivibrio* sp. remains in the system. Identification of the quantity of each microorganism can explain better the role of each organism in production of flammable gas.

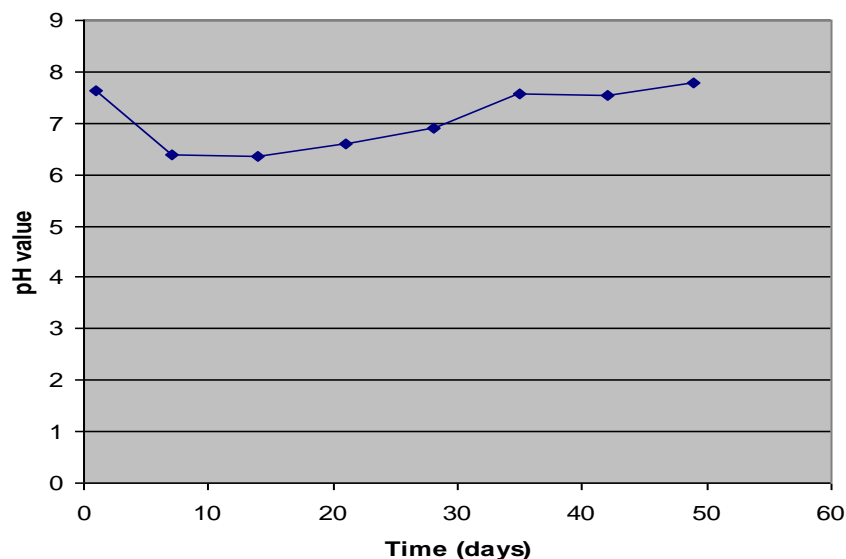


Figure 5. pH variation of the waste.

Table 2. Organisms/microbial species isolated and TVC at various stages of the anaerobic digestion of the dog faeces.

Organisms	At charging of waste	At flammability	At the end of gas production
Bacteria type	<i>Butyrivibrio</i> sp., <i>Clostridium</i> sp., <i>Ruminococcus</i> sp., <i>Acetivibrio</i> sp., <i>Eubacterium-Cellulosolvens</i> .	<i>Clostridium</i> sp., <i>Ruminococcus</i> sp., <i>Acetivibrio</i> sp., <i>Eubacterium- cellulosolvens</i>	<i>Clostridium</i> sp.
TVC	8.2×10^{14}	7.6×10^{11}	4.2×10^8

This further reveals the total disappearance of all the organisms at the end of the production stage leaving only the *Clostridium* sp. This conforms to the conclusion of Ofoefule et al. (2010) that AD does not completely eliminate microorganism in animal wastes. This probably implies that these bacteria were not involved in gas production or that the environment might not be conducive for their activity even though they accounted for 420 million of the identified organisms (Table 2). Decrease in microbial load over the period of biodigestion is a common phenomenon in microbial reactions. This has been observed by McGarvey et al. (2007) and Ofoefule et al. (2010).

Conclusion

Different biomass materials have different biogas generation potential. Whereas many have been tested to have high biogas viability, dog waste has low biogas production potential. From the results obtained, it can be

seen that dog waste has biogas generation potentials even though the production rate is very slow and with high retention time. Although gas yield was low, it can be used as inoculum for increasing the retention time of other biomass since it has high retention time. It is not however advisable to depend on dog waste alone for biogas production mainly due to the quantity of biomass is usually small and its biogas has long time to flame. Anaerobic digestion is a better option to composting in terms of pathogen handling and control.

Conflict of Interests

The author(s) have not declared any conflict of interests.

REFERENCES

- Abubakar BSUI, Ismail N (2012). Anaerobic Digestion of Cow Dung for Biogas Production. ARPN J. Eng. Appl. Sc. 7(2):169-172.
Atanu OS, Asere AA, Philips TK (2010). Biogas Generation From Anaerobic Digestion of Elephant Droppings. Nig. J. Solar Energy 21:145-148.

- Balasubramaniyam U, Lionel SZ, Niccoló M, Buysman V (2008). Biogas production in climates with long cold winters. Documentation Prepared by Wageningen University, the Netherlands for Women in Europe for a Common Future, WECF The Netherlands, pp. 1-68.
- Beck AM (1979). The Impact of the Canine Clean-up Law: Both Dogs and People Profit Environment. *Sci. Pol. Sustain. Dev.* 21(8):28-31. <http://dx.doi.org/10.1080/00139157.1979.9931200>
- Demirel B, Scherer P, Orhan Y, Turgut TO (2010). Production of Methane and Hydrogen from Biomass through Conventional and High-Rate Anaerobic Digestion Processes. *Crit. Rev. Environ. Sci. Tech.* 40:116-146. <http://dx.doi.org/10.1080/10643380802013415>
- Eze IS, Ofoefule AU, Uzodinma EO, Okoroigwe EC, Oparaku NF, Eze JI, Oparaku OU (2011). Characterization and Performance Evaluation of 11m³ Biogas Plant Constructed at National Centre for Energy Research and Development, University of Nigeria, Nsukka. *Cont. J. Renew. Energy* 2(1):1-6.
- Ilaboya IR, Asekham FF, Ezugwu MO, Eramah AA, Omofuma FE (2010). Studies on Biogas Generation from Agricultural Waste; Analysis of the Effects of Alkaline on Gas Generation. *World App. Sci. J.* 9(5):537-545.
- McGarvey JA, William GM, Ruihong Z, Yanguo M, Frank M (2007) Bacterial Population Dynamics in Dairy Waste during Aerobic and Anaerobic Treatment and Subsequent Storage. *Appl. Environ. Microbiol.* 73(1):193-202. <http://dx.doi.org/10.1128/AEM.01422-06>; PMID:17085701 PMCID:PMC1797099
- Ofoefule AU, Uzodinma EO (2009). Biogas production from blends of cassava (*Manihot utilissima*) peels with some animal wastes. *Int. J. Phys. Sci.* 4(7):398-402.
- Ofoefule AU, Uzodinma EO, Anyanwu CN (2010). Studies on the Effect of Anaerobic Digestion on the Microbial Flora of Animal Wastes 2: Digestion and Modeling of Process Parameters. *Trends Appl. Sci. Res.* 5(1):39-47.
- Okore VC (2004): Surface Viable Count Method. A standard laboratory technique in Pharmaceuticals and Pharmaceutical Microbiology. 2nd Edn. El'Demark Publishers, pp. 24-26.
- Okoroigwe EC. (2007). Application of Biomass Technology in Sustainable Agriculture. *Trends Appl. Sci. Res.* 2(6):549-553. <http://dx.doi.org/10.3923/tasr.2007.549.553>
- Okoroigwe EC, Eze JI, Oparaku OU (2008). Field Comparison of Biofertilizer and Chemical Fertilizer Application on Maize Production. *Nig. J. Solar Energy* 19(1):55-57.
- Oparaku NF, Ofomatah AC, Okoroigwe EC (2013). Biodigestion of Cassava Peels Blended with Pig Dung for Methane Generation. *Afr. J. Biotechnol.* 12(40):5956-5961.
- Prociv P, Croese J (1990). Human Eosinophilic Enteritis Caused by Dog Hookworm *Ancylostoma caninum*. *Lancet* 335(8701):1299-1302. [http://dx.doi.org/10.1016/0140-6736\(90\)91186-E](http://dx.doi.org/10.1016/0140-6736(90)91186-E)
- Singh R, Amrit BK, Jagan NS (2008). Production of Biogas from Poultry Waste. *Int. J. Renew. Energy* 3(1):11-20.
- Taylor L (2004). Poop, Scoop and Compost: Proposal to Explore the Feasibility of Composting Dog Waste in Public Parks.
- Ukpai PA, Nnabuchi MN (2012). Comparative study of biogas production from cow dung, cow pea and cassava peeling using 45 litres biogas digester. *Adv. Appl. Sci. Res.* 3(3):1864-1869.
- Unruh DHA, King JE, Eaton RDP, Allen JR (1973). Parasites of Dogs from Indian Settlements in Northwestern Canada: A Survey with Public Health Implications. *Can. J. Comp. Med.* 37:25-32. PMID:4265550 PMCID:PMC1319720
- Wang X, Yang G, Feng Y, Ren G, Han X (2012). Optimizing feeding composition and carbon-nitrogen ratios for improved methane yield during anaerobic co-digestion of dairy, chicken manure and wheat straw. *Bioresour. Technol.* 120:78-83. <http://dx.doi.org/10.1016/j.biortech.2012.06.058>; PMID:22784956
- Yadvika S, Sreekrishnan TR, Sangeeta K, Vineet R (2004). Enhancement of biogas production from solid substrates using different techniques – A review. *Bioresour. Technol.* 95 (1):1-10. <http://dx.doi.org/10.1016/j.biortech.2004.02.010>; PMID:15207286
- Zhang T1, Liu L, Song Z, Ren G, Feng Y, Han X, Yang G (2013). Biogas Production by Co-digestion of Goat Manure with Three Crop Residues. *PLOS ONE* 8(6):e66845. doi:10.1371/journal.pone.0066845.

Full Length Research Paper

A Novel SPICE compatible behavioral model for molecular electronics having hysteresis effects

Davoud Bahrepour* and Mohammad Javad Sharifi²

¹Mashhad Branch, Islamic Azad University, Mashhad, Iran.

²Faculty of Electrical and Computer Engineering, Shahid Beheshti University, Tehran, Iran.

Received 2 April, 2012; Accepted 4 April, 2013

Although molecular electronics is in its infancy, there are many significant advances in understanding and implementing computational functions based on molecular electronic devices. In order to evaluate a molecular electronic circuit, a model is needed. In existing literature, only a few models have been introduced for molecular electronics, all of which do not support the hysteresis phenomenon. To the best of the authors' knowledge, for the first time, this paper introduces a behavioral model in SPICE which is able to imitate hysteresis behavior in a desired molecular circuit. The proposed model is then modified in order to guarantee continuous behavior in its I/V curves. Some molecular electronic I/V curves from the literature are selected and by utilizing the proposed model, its correct operation are investigated.

Key words: Molecular electronics, behavioral model, hysteresis phenomenon, SPICE.

INTRODUCTION

During the last decades, the feature size of MOS-based circuits has dramatically decreased. The ever decreasing feature size will face serious challenges and alternative technologies should therefore be selected. Due to their performance and density, molecular electronics is a promising candidate for nanoelectronic applications. Molecular electronics has also been proposed as a pathway for high-density nanoelectronic devices (Seminario, 2005). Many efforts have been made by researchers to introduce and describe different structures and technologies based on molecular devices (Strukov and Likharev, 2005; Martin, 2009; Yuqing et al., 2011; Gimenez et al., 2009; Liu et al., 2011). Before manufacturing process of molecular electronic circuits, a model is needed in order to simulate the behavior of the circuit in a reasonable amount of time and with

acceptable accuracy. In this paper, a behavioral model for modeling the hysteresis phenomenon in molecular based circuits is proposed. The model is then implemented in SPICE and the correct operation of the model is investigated. Finally for achieving the most accuracy a modification in the proposed behavioral model is made.

MATERIALS AND METHODS

A brief survey of molecular electronics models

In general, there are two major categories for simulating electronic circuits: the physics-based models and the nonphysics-based models or behavioral models. Physics-based molecular device modeling is very difficult due to the unknown underlying physics

*Corresponding author. E-mail: bahrepour@ieee.org. Tel: +98 915 314 5203.

Author(s) agree that this article remain permanently open access under the terms of the [Creative Commons Attribution License 4.0 International License](http://creativecommons.org/licenses/by/4.0/)

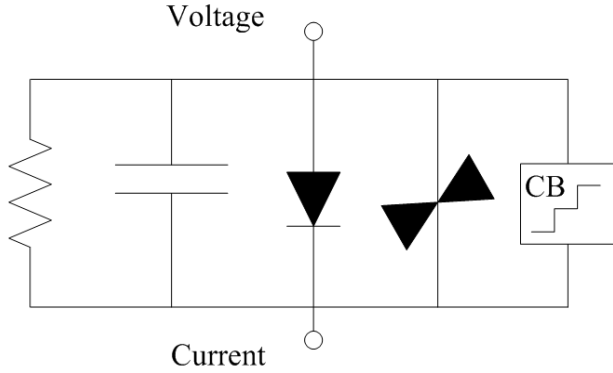


Figure 1. Two-terminal UDM. The main features of this model are capacitance, resistance, thermionic emission, NDR, and coulomb blockade.

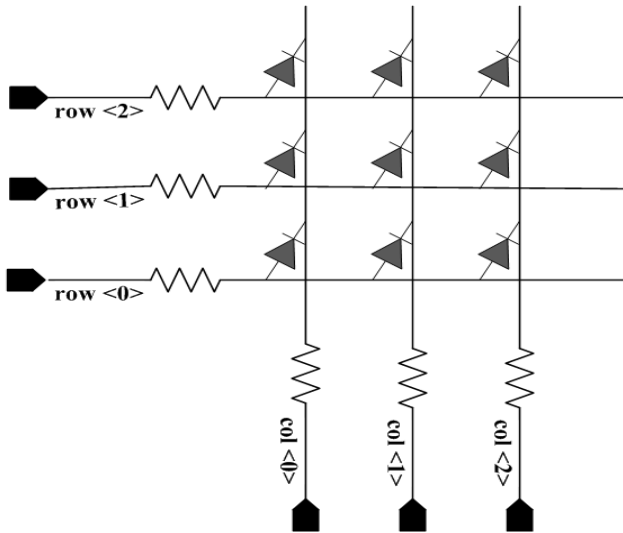


Figure 2. Equivalent circuit schematic of a crossbar technology.

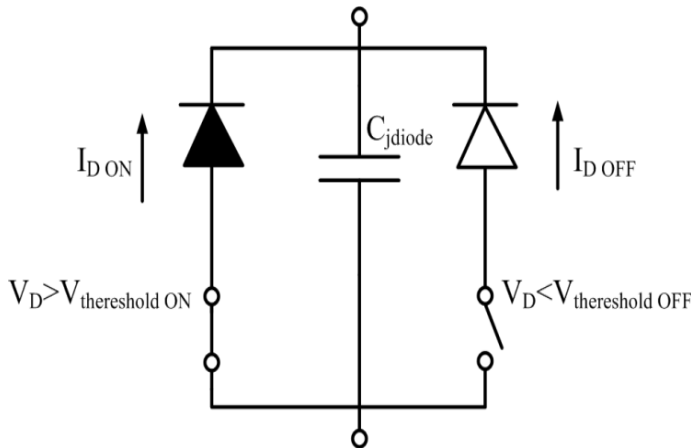


Figure 3. A device model for crossbar technology. Figure source: Ziegler and Stan (2003). Two diodes are used for showing the on-state and off-state of a cross bar junction.

and also the variety of applied materials. However, circuit designers need a model of these devices to evaluate their design performance. The behavioral models introduced for emerging devices have solved this problem and have helped circuit designers to easily design and verify the output of their circuits. In this regard, many efforts have been made (Yan et al., 1995; Yu et al., 1999; Bhattacharya and Mazumder, 2001; Sharifi and Bahrepour, 2009; Sharifi and Banadaki, 2010). For molecular devices three models have been proposed so far.

(i) Ziegler et al. (2002) proposed a circuit model for molecular devices called the universal device model (UDM) (Ziegler et al., 2002). This model is characterized in more detail in Stan et al. (2003), and Rose et al. (2004, 2007). The UDM concept uses empirical equations that describe each fundamental quantum and classical effect that may be relevant to an electronic device (Stan et al., 2003). As shown in Figure 1 the common sub-features used in the UDM are: resistive behavior (linear I - V curve), diode-like behavior (exponential I - V curve), coulomb-blockade behavior (step I - V curve), and tunneling behavior (peak I - V curve) for a DC characteristic. The UDM accepts a set of current and voltage data points, which are obtained theoretically or experimentally, and then it produces the appropriate coefficient for the mentioned UDM features. The current equation of a device is achieved by the use of the respective weight of each feature as:

$$I_{UDM}(V) = \alpha_R I_R(V) + \alpha_D I_D(V) + \alpha_T I_T(V) + \alpha_{CB} I_{CB}(V) \quad (i)$$

(ii) Ziegler et al. (2003) proposed a device model for a crossbar structure which is a main technology in molecular electronics (Ziegler and Stan, 2003). The crossbar technology sandwiches bistable molecules, for example, rotaxanes, between wires at each junction. Figure 2 shows the equivalent circuit of a typical crossbar technology. As shown in Figure 3, the presented model utilizes two diodes for representing the on-state and off-state of a crossbar junction, in parallel with a parasitic junction capacitance. If the applied voltage (V_D) is greater than the on-state threshold ($V_{thresholdON}$), the model switches to the on-state and if the applied voltage (V_D) is lower than the off-state threshold ($V_{thresholdOFF}$), the model switches to the off-state. In this model, the junction capacitance, current-voltage characteristics and switching threshold values should be selected in an appropriate manner in order to obtain a proper mimic of crossbar structure based devices (Ziegler and Stan, 2003).

(iii) Ci Lei et al. (2007) introduced a device model (Lei et al., 2007, 2008) in which the electron transport properties of a molecular system were studied by viewing it as a one electron elastic scattering problem. The Breit-Wigner resonance formula was used to model a general crossbar structure. In this model, the transmitted current (I) through the metal-molecule-metal junction is proportional to the transmission probability ($T(E)$) for a range of energy levels around the Fermi energy of the source lead and it is computed using Landauer's formula as Equation (2).

$$I(V) = \frac{2e}{h} \int_{-\infty}^{\infty} dET(E) \left(\frac{1}{\exp[(E - \mu_s)/kT] + 1} - \frac{1}{\exp[(E - \mu_d)/kT] + 1} \right) \quad (ii)$$

where μ_s and μ_d are the electro-chemical potentials of the source and drain respectively. In addition the transmission probability $T(E)$ used in the Landauer formula is approximated by the Breit-Wigner formula as follows.

$$T(E) = \frac{4\Gamma_1\Gamma_2}{(E - \varepsilon_0)^2 + (\Gamma_1 + \Gamma_2)^2} \quad (iii)$$

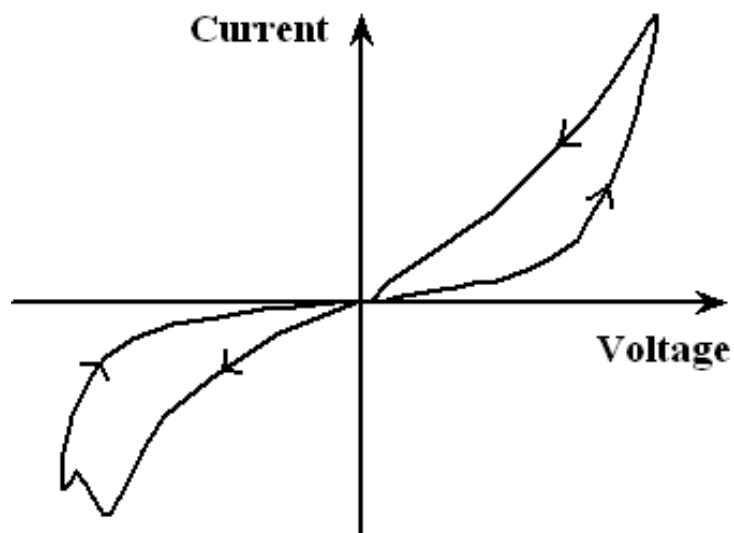


Figure 4. A generic I - V curve for a typical molecular hysteresis switch. Figure source: Rose and Stan (2007).

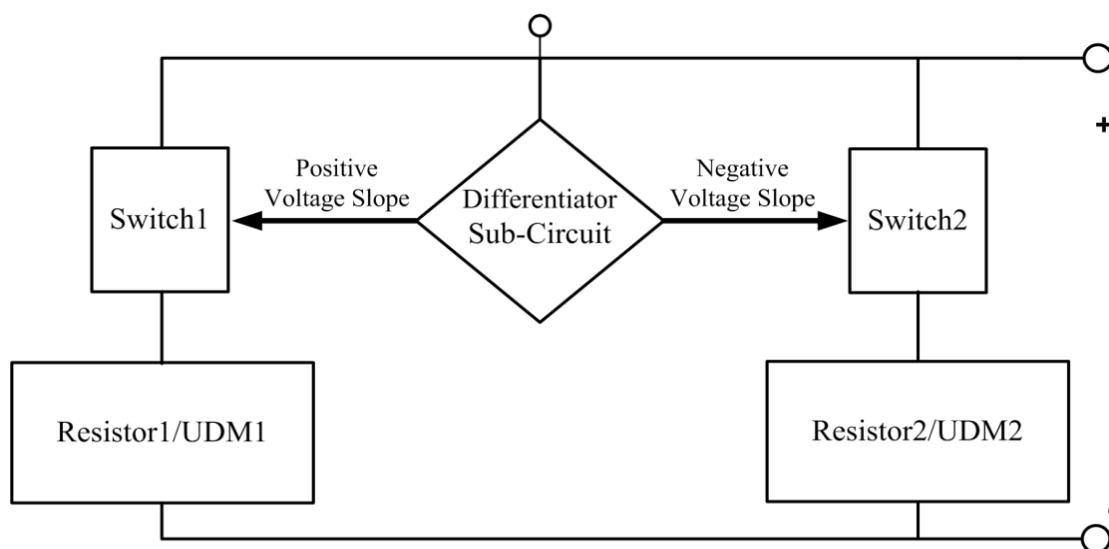


Figure 5. Block diagram for the proposed behavioral model. The differentiator sub-circuit selects one of the resistors/UDM modules. And the selected resistors/UDM modules generate appropriate current.

The hysteresis phenomenon

Hysteresis is a non classical behavior and refers to a device's ability to switch between stable behaviors. Hysteresis not only depends on the current environment but also depends on its past environment. To predict the future behavior of a hysteresis progress, either its internal state or its history must be known (Mielke and Roubicek, 2003). If a given input alternately increases and decreases, then the output tends to form a loop.

Although hysteresis curves have different shapes, many molecular switching devices have an I - V characteristic such as that presented in Figure 4 (Rose and Stan, 2007). This curve illustrates that, in general, molecular electronic I - V curves have hysteresis in the first and third quadrant. Also in each quadrant there are two different paths called reverse and forward paths which signifies

positive or negative voltage slope, respectively.

Introducing a behavioral model for hysteresis

Circuit designers need a complete and easy to use model for describing the behavior of a molecular electronic device used in a computational or memory circuit. Although the models mentioned before are applicable, they do not support hysteresis phenomenon. This paper bridges the existing gap by introducing a behavioral model for hysteresis phenomenon usually appeared in molecular electronic circuits. Figure 5 shows the proposed behavioral model which comprised of a differentiator sub-circuit for identifying the positive/negative slopes of a molecular device voltage and two resistor/UDM modules. As seen from Figure 5, the sign of the

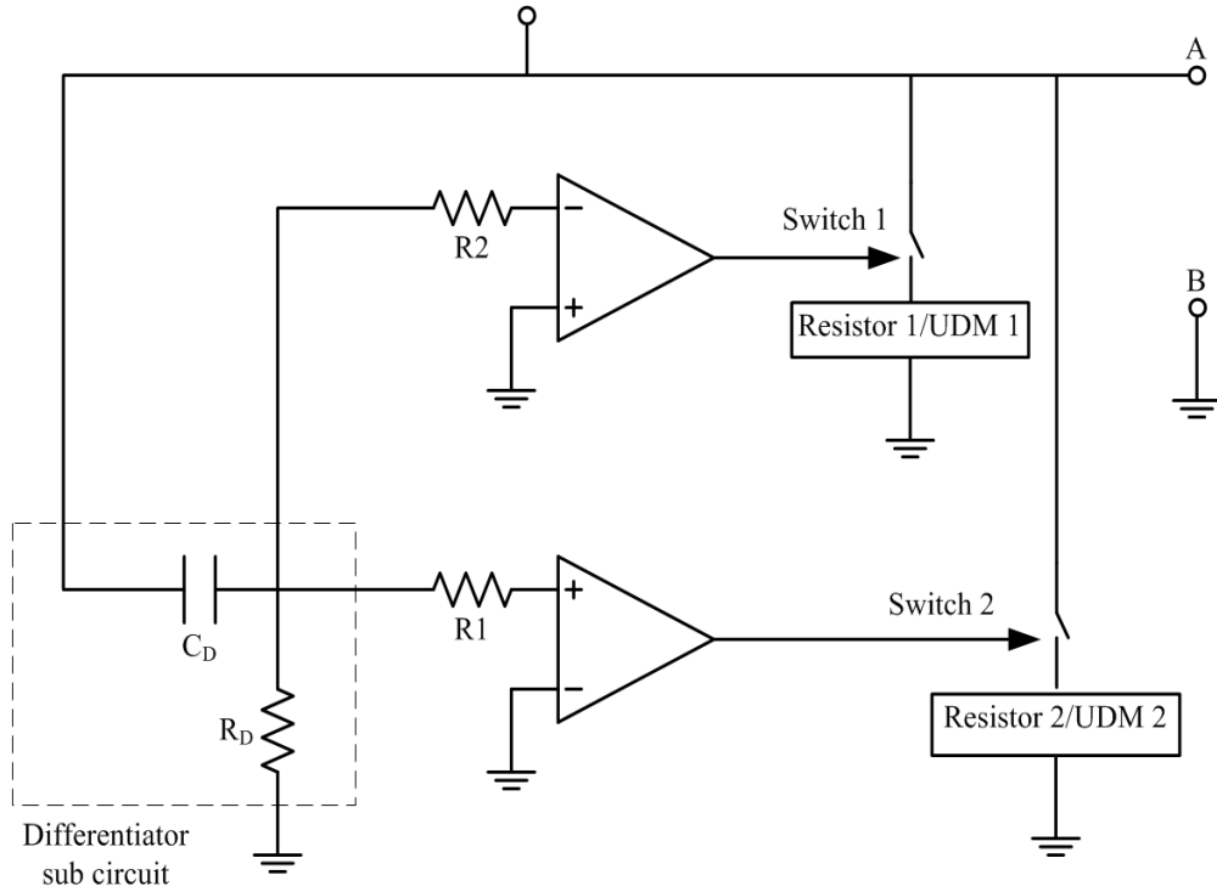


Figure 6. The proposed circuit model for imitating hysteresis behavior. This model consists of a differentiator sub-circuit, two switches and two resistor/UDM modules.

voltage slope is achieved using a differentiator sub-circuit which selects one of the resistor/UDM modules for producing the appropriate device current. The positive slope signifies increasing voltage that in the hysteresis curve means forward path and the negative slope indicates decreasing voltage that in the hysteresis curve means reverse path. The proposed circuit for the LHM and GHM is presented in Figure 6. As shown, this model utilizes simple circuit elements in order to generate hysteresis behavior in molecular electronics circuit.

RESULTS

By considering the proposed behavioral model for hysteresis phenomenon in previous section, there are two different approaches for implementing the model: i) the linear hysteresis model (LHM) and ii) the general hysteresis model (GHM). The LHM uses two different resistors for generating appropriate current values and hence, it has minimum possible complexity. In Figure 6 the Resistor 1 and Resistor 2 values may be approximated by the average of the forward and reverse slope values appeared in the first and third quadrants of given I/V curves. In fact this model imitates the I/V characteristics of a device in linear format. Figure 7(a)

shows I/V curves for the ZnO/aluminum stack (Lüssem, 2006) and a dashed line in Figure 7(b) depicts the simulation outputs using the LHM. This approach has two main drawbacks: i) it eliminates the details of the reverse or forward paths and changes them to two simple lines with different slopes and ii) since the amount of slopes in the first and third quadrant of a specific curve may be different in the forward or reverse paths, this model replaces these amounts by their average values which means less accuracy. In the GHM, the resistors are replaced with proper UDMs; hence, the simulation output is more accurate. This approach helps to save the details of I/V curves with more precision. The solid line in Figure 7(b) shows the simulation output of the I/V curve for the ZnO/aluminum stack using the GHM. As another example, the $I-V$ curve for the ITO/aluminum stack (Lüssem, 2006) is selected (Figure 8(a)). In Figure 8(b) the dashed line and solid line depict the simulation outputs using the proposed LHM and GHM respectively. As depicted in Figures 7(b) and 8(b) there is a very good agreement between the GHM and the original I/V curves. For modeling the ZnO/aluminum and ITO/aluminum stack curves the applied characteristics in the proposed circuit are: $C_D=1$ nF, $R_D=100$ K Ω and $R_2=R_3=1$ K Ω .

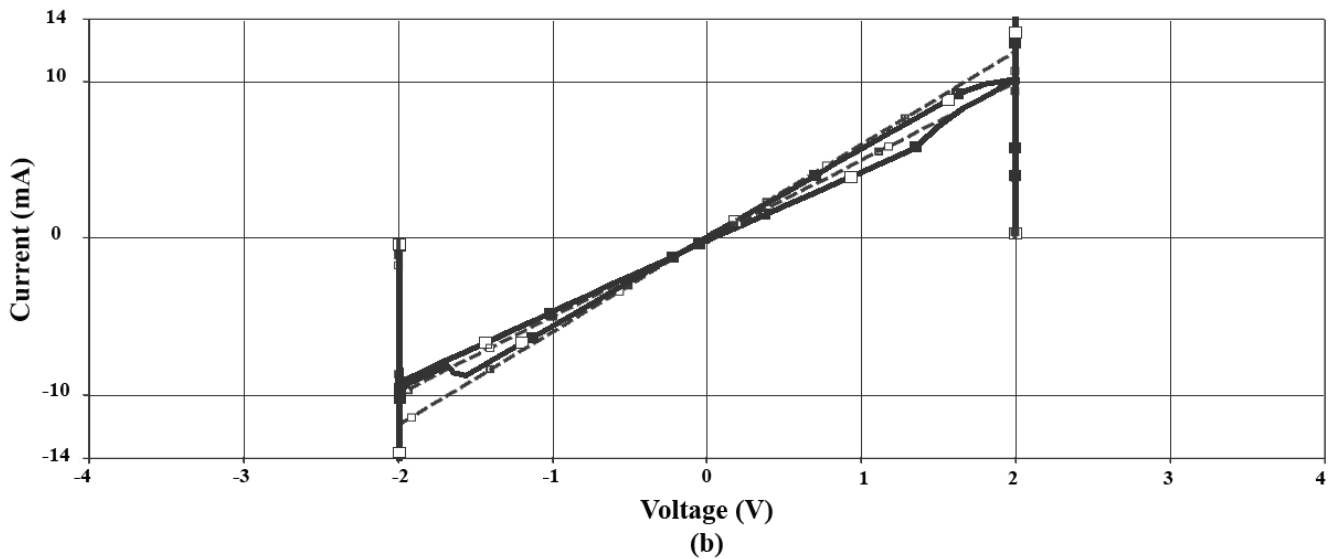
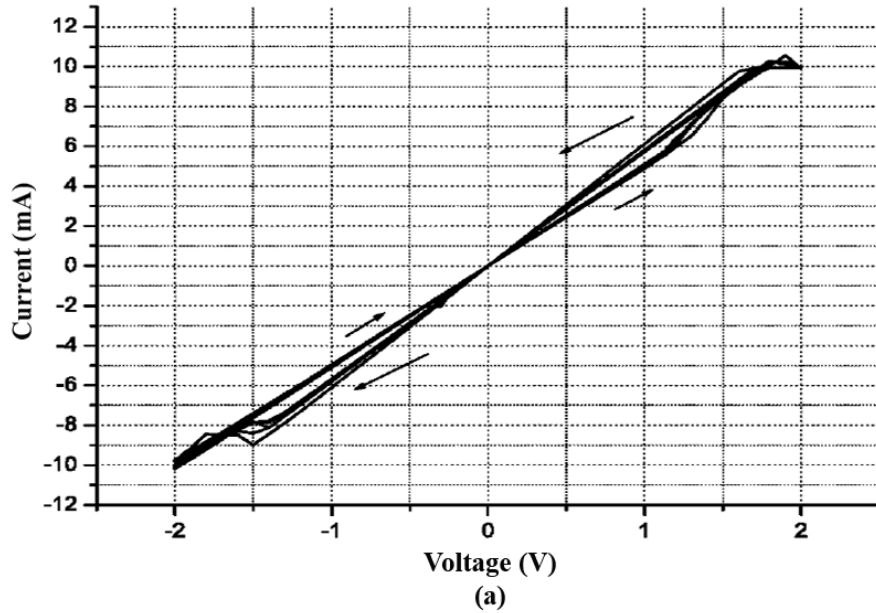


Figure 7. (a) *I-V* characteristic of the ZnO/aluminum stack which shows hysteresis behavior. Figure source:Lüsse (2006). (b) The simulation result curves by the use of the LHM (dashed line) and GHM (solid line). For achieving the LHM output the forward and reverse slope values are specified by utilizing two different resistors (166 Ω and 200 Ω respectively).

DISCUSSION

The proposed behavioral model is easy to use and operates in a short period of time and with very good accuracy. However, the model has a main disadvantage in that it cannot produce a smooth and continuous output when the input signal changes its direction (rising and or falling points). However, for overcoming this disadvantage this model is modified by adding a simple integrator circuit (Figure 9) to points A and B of the proposed circuit model. The effect of this modification is found in Figure 10. Figure 10(a) provides the applied

voltage to the device which its *I/V* curve was previously shown in Figure 7(a); Figure 10(c) and (b) demonstrate the response of the device to the applied voltage with and without utilizing the proposed integrator circuit, respectively. As mentioned before, utilizing two resistors in the LHM instead of the GHM leads to more simplicity. However, in the forward and reverse paths the discontinuous behavior is appeared (Figure 10(b)). As seen in Figure10(c), exploiting a simple integrator circuit makes these points disappear. As an instance, in the appendix, the SPICE NETLIST of the proposed hysteresis circuit model for Figure 7 is presented.

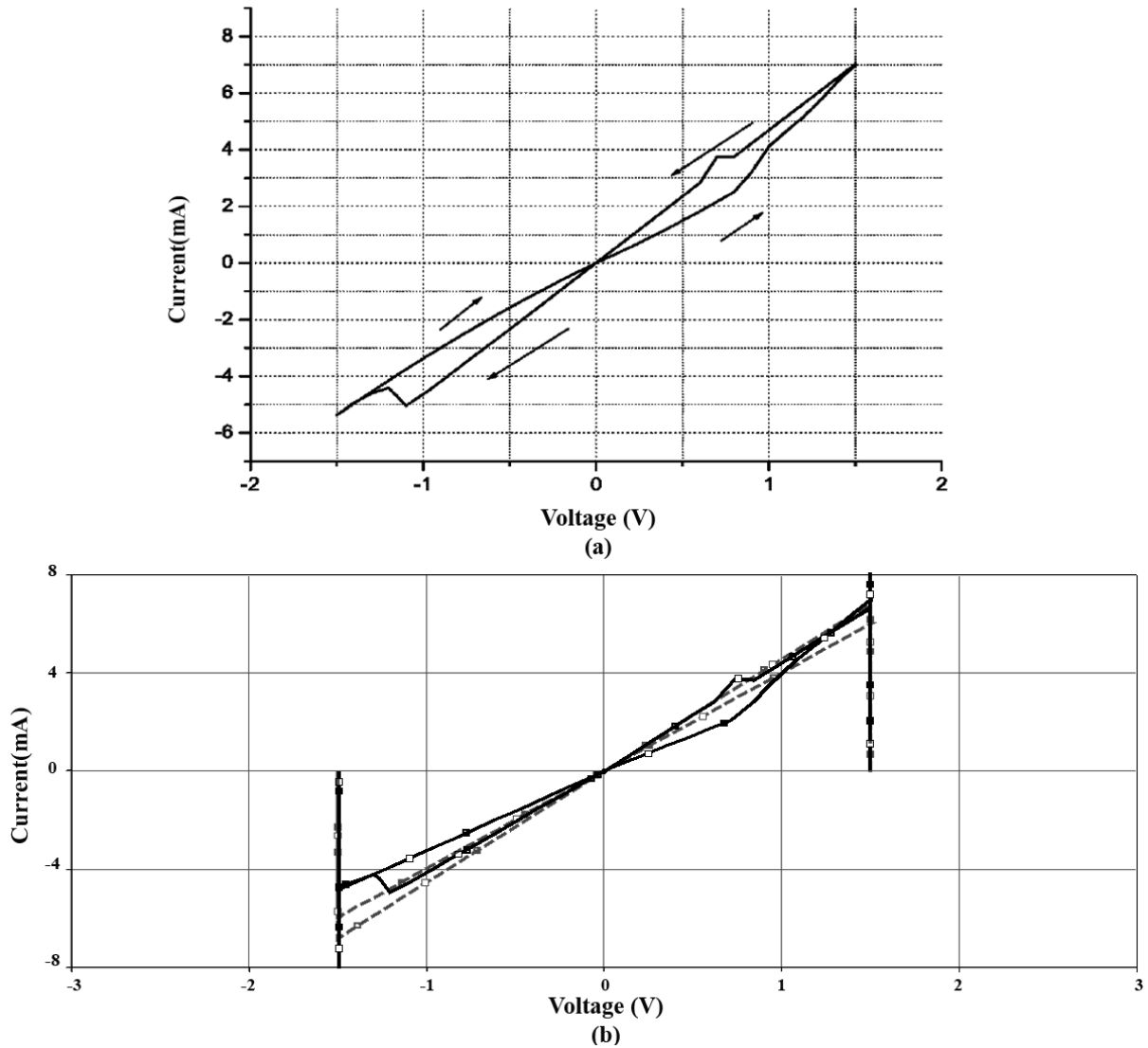


Figure 8. (a) I - V characteristic of the ITO/aluminum stack which shows hysteresis behavior. Figure source: Lüssem, (2006). (b) The simulation result curves by the use of the LHM (dashed line) and GHM (solid line). For achieving the LHM output the forward and reverse slope values are specified by utilizing two different resistors (250Ω and 219Ω respectively).

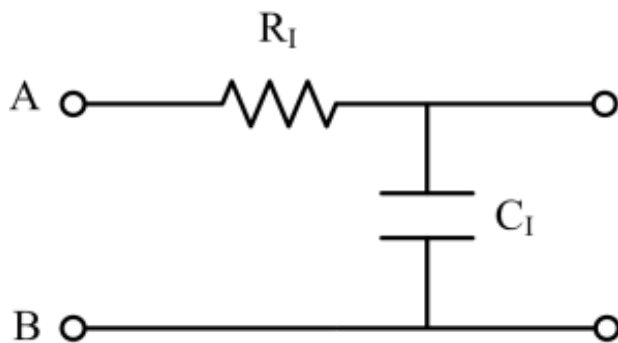


Figure 9. Applying simple integrator circuit helps to achieve continuous curves in the output.

Conclusions

Since molecular electronics attracts much attention in literature; some effort has been made to model molecular electronic behavior. However, all of the proposed models do not support the hysteresis phenomenon. To the best of the authors' knowledge, for the first time, this paper proposes a behavioral model for the hysteresis phenomenon in simulating molecular electronic devices. The proposed behavioral model is implemented in SPICE with two different approaches (the LHM and GHM) and the correct operation of each approach is investigated. The proposed model is then modified by adding a simple integrator circuit for solving the discrete points' problem.

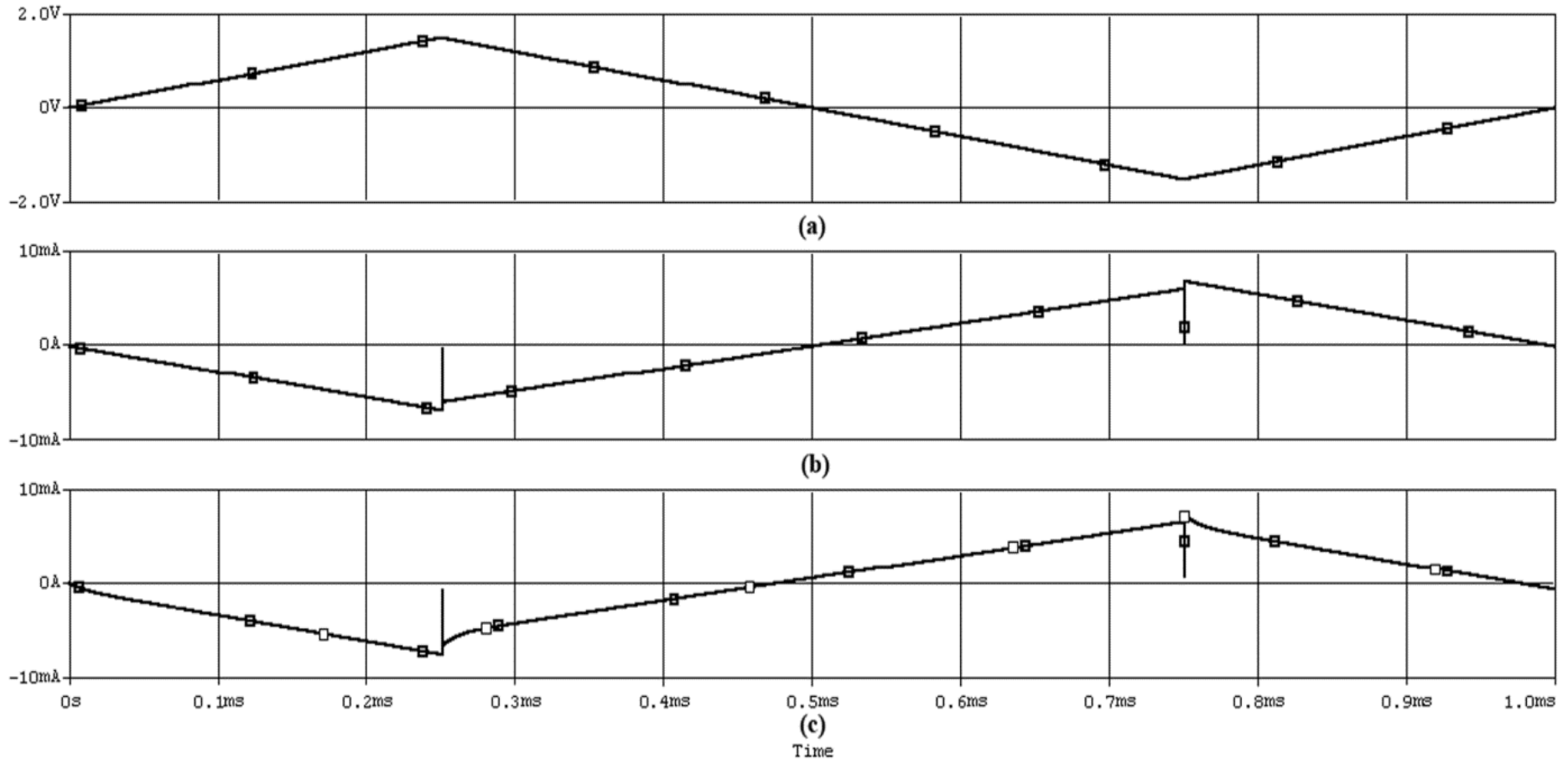


Figure 10. The effect of using integrator circuit in the proposed circuit for modeling the Figure 7 I/V curve. (a) Applied voltage. (b) Current curve without exploiting the integrator circuit. (c) Current curve after modification and with exploitation of the integrator circuit. The applied characteristics are: $C_f=100$ nF and $R_f=0.1$ K Ω .

This model helps the circuit designer to evaluate a design with more simplicity and accuracy.

APPENDIX

In this appendix, a SPICE NETLIST for the

simulation result of Figure 7 curve is demonstrated. This simulation uses the modified GHM approach.

C_C21 N34624 N34628 1n
 R_R2 0 N34754 20
 C_C1 N09392 N11976 1n

R_R1 0 N11976 1k
 R_R3 0 N09392 100k
 X_S2 N59306 0 N09392 N24506
 SCHEMATIC1_S2
 V_V1 N09392 0
 +PWL 0 0 250us 2 750us -2 1000us 0
 G_G220 N34754 N24506 TABLE {V(N34754,

```

N24506})
+ [(0,0) (1.25,6 m) (1.4,8 m) (1.5,8.5 m) (1.75,10 m)]
R_R5      N627581 N09392 1k
C_C11     N24506 N34754 1n
C_C2      0 N627581 10n
R_R4      N34628 0 10
C_C12     N24506 N34754 1n
G_G230    N34754 N24506 TABLE {V(N34754,
N24506)}
+ [(-2, -10 m) (0, 0)]
E_U2      N23820 0 VALUE {LIMIT(V(N11976, 0)*1E6, -
1V, +1V)}
E_U1      N59306 0 VALUE {LIMIT(V(N11976, 0)*1E6, -
1V, +1V)}
G_G130    N34628 N34624 TABLE {V(N34628, N34624)}
+ [(-2,-10m) (-1.6, -8.2 m) (-1.5, -9 m) (0, 0)]
G_G120    N34628 N34624 TABLE {V(N34628, N34624)
}
+ [(0, 0) (1.5, 9 m) (1.75, 10 m)]
X_S1      0 N23820 N34624 N09392 SCHEMATIC1_S1
C_C22     N34624 N34628 1n
.subckt SCHEMATIC1_S2 1 2 3 4
S_S2      3 4 1 2 Sbreak
RS_S2     1 2 1G
.ends SCHEMATIC1_S2
.subckt SCHEMATIC1_S1 1 2 3 4
S_S1      3 4 1 2 Sbreak
RS_S1     1 2 1G
.ends SCHEMATIC1_S1

```

Conflict of Interests

The author(s) have not declared any conflict of interests.

REFERENCES

- Bhattacharya M, Mazumder P (2001). Augmentation of SPICE for simulation of circuits containing resonant tunneling diodes. *IEEE Trans. Computer-Aided Des.*, 20(1):39-50.
- Gimenez AJ, Luna-Barcenas G, Seminario JM (2009). Analysis of nano and molecular arrays of negative differential resistance devices for sensing and electronics. *Sensors J.* 9(9):1136-1141. <http://dx.doi.org/10.1109/JSEN.2009.2026003>
- Lei C, Pamunuwa D, Bailey S, Lambert C (2007). Molecular Electronics Device Modeling for System Design. *IEEE International Conference on Nanotechnology*, Hong Kong, Aug. pp. 1116-1119.
- Lei C, Pamunuwa D, Bailey S, Lambert C (2008). Application of Molecular Electronics Devices in Digital Circuit Design. *Third International Conference on Nano-Networks*, pp. 60-64.
- Liu YS, Hong XK, Feng JF, Yang XF (2011). Fano-Rashba effect in thermoelectricity of a double quantum dot molecular junction. *Nanoscale Res. Lett.* 6:618-628. <http://dx.doi.org/10.1186/1556-276X-6-618>; PMID:22151740 PMID:PMC3258288
- Lüsse B (2006). Molecular Electronic Building Blocks Based on Self-Assembled Monolayers. *Forschungszentrum Jülich GmbH*.
- Martin ZL, Majumdar N, Cabral MJ, Gergel-Hackett N, Camacho-Alanis F, Swami N, Bean JC, Harriott LR, Yao Y, Tour JM, Long D, Shashidhar R (2009). Fabrication and Characterization of Interconnected Nanowell Molecular Electronic Devices in Crossbar Architecture. *IEEE Trans. Nanotechnol.* 8(5):574-581. <http://dx.doi.org/10.1109/TNANO.2009.2021161>
- Mielke A, Roubicek T (2003). A Rate-Independent Model for Inelastic Behavior of Shape-Memory Alloys. *Multiscale Model. Simul.* 1(4):571-597. <http://dx.doi.org/10.1137/S1540345903422860>
- Rose GS, Stan MR (2007). A programmable majority logic array using molecular scale electronics. *IEEE Trans. Circuits Syst. I*, 54(11):2380-2390. <http://dx.doi.org/10.1109/TCSI.2007.907860>
- Rose GS, Ziegler MM, Stan MR (2004). Large-signal two-terminal device model for nanoelectronic circuit analysis. *IEEE Trans. Very Large Scale Integration (VLSI) Systems*, 12(11):1201-1208.
- Seminario JM (2005). Molecular electronics: approaching reality. *Nature Mater*, 4:111-113. <http://dx.doi.org/10.1038/nmat1313>; PMID:15689945
- Sharifi MJ, Banadaki YM (2010). General spice models for memristor and application to circuit simulation of memristor-based synapses and memory cells. *World Sci. J. Circuits Syst. Comput.* 19:407-424. <http://dx.doi.org/10.1142/S0218126610006141>
- Sharifi MJ, Bahrepour D (2009). A new XOR structure based on resonant-tunneling high electron mobility transistor. *VLSI Design*, 2009.
- Stan MR, Franzone PD, Goldstein SC, Lach JC, Ziegler MM (2003). Molecular electronics: From devices and interconnect to circuits and architecture. *Proceedings of the IEEE*, 91(11):1940-1957. <http://dx.doi.org/10.1109/JPROC.2003.818327>
- Strukov DB, Likharev KK (2005). CMOL FPGA: A reconfigurable architecture for hybrid digital circuits with two-terminal nanodevices. *Nanotechnol.* 16:888-900. <http://dx.doi.org/10.1088/0957-4484/16/6/045>
- Yan Z, Deer MJ (1995). New RTD large-signal DC suitable for PSPICE. *IEEE Trans. Computer Aided Des.* 14(2):167-172.
- Yu YS, Jung YI, Park JH, Hwang SW, Ahn D (1999). Simulation of single-electron/CMOS hybrid circuits using SPICE macromodeling. *J. Korean Phys. Soc.* 20(35):S991-S994.
- Yuqing X, Changfeng F, Bin C, Guomin J, Yaxin Z, Desheng L (2011). Gated electronic currents modulation and designs of logic gates with single molecular field effect transistors. *Appl. Phys. Lett.* 99:043304-043304. <http://dx.doi.org/10.1063/1.3615691>
- Ziegler MM, Rose G, Stan M (2002). A universal device model for nanoelectronic circuit simulation. *IEEE Conf. Nanotechnol*, pp. 83-88.
- Ziegler MM, Stan MR (2003). CMOS/nano co-design for crossbar-based molecular electronic systems. *IEEE Trans. Nanotechnol.* 2(4):217-230. <http://dx.doi.org/10.1109/TNANO.2003.820804>

Full Length Research Paper

Application of statistical techniques to evaluate the reliability of ultrasonic and rebound hammer measurements of compressive strength in the concrete of bridges

C. H. Carvalho^{1*}, J. B. Severo Junior², M. C. S. S. Macedo³, S. Griza³, C. E. C. de Andrade³, A. A. dos Santos³ and L. S. Barreto³

¹Federal Institute of Sergipe, Graduate Program in Materials Science and Engineering of the Federal University of Sergipe – UFS, Brazil.

²Department of Chemical Engineering, Federal University of Sergipe – UFS, Brazil.

³Department of Materials Science and Engineering, Federal University of Sergipe – UFS. Federal University of Sergipe, Marechal Rondon ave, Jardim Rosa Elze, São Cristovão, Zip Code: 49100-000, Sergipe, Brazil.

Received 22 December, 2013; Accepted 10 March, 2014

In order to assess the uncertainties in the experimental measurements, the use of statistical error analysis is essential for a reliable technical diagnosis on structural safety in reinforced concrete of bridges. Two non-destructive techniques (ultrasound and rebound hammer) were performed, resulting in conflicting technical diagnostics when analyzed without the study of the variability of experimental errors. It was evident that physically the only use of arithmetic average means nothing. The obtained results also demonstrated the lack of correlations between those ones driven by the ultrasound and the impact hammer on the four tested bridges.

Key words: Rebound hammer, ultrasound, compressive strength, nondestructive tests, statistical error analysis.

INTRODUCTION

Nowadays, reinforced concrete is globally the most widely used construction material, and the use of Non-Destructive Testing (NDTs) to measure its properties *in situ*, without causing damage, and to monitor structural integrity, is employed to determine the useful lifespan of structures (Hamidian et al., 2012). The use of a combination of nondestructive methods can improve the reliability of results, which are then closer to the true

values when compared with measurements made using individual tests alone (Shariati et al., 2011; Breyse, 2009, 2012; Sbartai et al., 2012). Such combined methods have a long history of use for investigating damage, cracks, fissures, void spaces, decreased mechanical strength, and other defects related to the deterioration of concrete (Shariati et al., 2011). Some of the available technical guidelines (ABNT, 1995; BS, 1986) suggest that the



Figure 1. Illustration of the rectangular network used for measurements by impact hammer and ultrasound in a region of maximum stress of a bridge stringer.

compressive strength of concrete can be estimated using curves describing the correlation between the values obtained from Non-Destructive Testing (NDTs) and destructive compressive tests. Although the mechanical strength of concrete shows no direct relationship with surface hardness or ultrasound propagation velocity, empirical models have been developed using regression techniques to describe the correlations between strength and the results obtained using the two techniques (Hamidian et al., 2012; Shariati et al., 2011; Machado et al., 2009; Mature, 2011; Almeida, 1993; Mohammed et al., 2011). This is because the strength of concrete is well correlated to the stiffness and the surface hardness of concrete. The relation between ultrasound, rebound hammer and compressive strength is then indirect relation. The rebound hammer method has been used in other areas such as in saligna eucalyptus wood pieces to assess trends of correlations between compressive strength to normal and parallel to the fibers (Soriano et al., 2011).

Comparison of the results of experimental measurements requires confidence in the reliability of the data obtained, especially when it is proposed to combine techniques that are very different, such as ultrasound and rebound hammer. This, together with interpretation of the measurements, can be achieved by combining experimental procedures with appropriate statistical techniques. Even when experiments are repeated under the same conditions, the results may not be identical or even comparable. The existence of experimental error is systematic or random, may lead to values that vary widely (Taylor, 2012; Box et al., 2005; Severo et al., 2011). In all areas of knowledge, including that of Non-Destructive Testing (NDTs), it is common to find studies in which adequate statistical treatment of the data has not been applied, in many cases leading to erroneous

conclusions (Cerqueira et al., 1999; Larenti, 2003). Straightforward statistical techniques that are available for this purpose include the Student's t-test and Fisher's F-test (Nguyen et al., 2013). Although simple, these tests can provide reliable interpretation of the extent of any experimental errors (Cerqueira et al., 1999; Larentis et al., 2003).

In the present work, measurements employing ultrasound and rebound hammer, together with statistical tests to evaluate the reliability of the results, were employed to determine the mechanical compressive strength of reinforced concrete at four bridges located in the city of Aracaju (Sergipe State, Brazil).

METHODOLOGY

Measurement procedures

A total of 1360 ultrasound measurements and 680 impact measurements were made at pillars and stringers of the four bridges, at structurally strategic locations with maximum internal loadings. The guidelines used as references in the test procedures were NBR 7584/95 (ABNT, 1995), NM 78:96 (Mercosur, 1996), and ASTM C 805-85, (ASTM, 1993) for surface hardness, and NBR 8802 (ABNT, 1994) and ASTM C 597, (ASTM, 2002) for the propagation of ultrasound in concrete. The equipment used for the impact tests was a SilverSchmidt-type mechanical hammer with impact energy of 2.2 Nm, while the ultrasound tests employed a USLab instrument equipped with a pair of flat 54 KHz transducers. The impact tests were made horizontally and perpendicularly to the surfaces of the concrete, and the ultrasound tests used direct transmission between opposite faces. The use of all equipment followed standardized calibration routines.

Prior to beginning the final tests, possible local interferences were minimized by performing scans to locate reinforcements underlying the locations that were subsequently tested, and by cleaning the sampling regions in order to smooth the surfaces and reduce surface deposits of carbonates. A manual Profoscope metal reinforcement detector was used. Figure 1 illustrates the

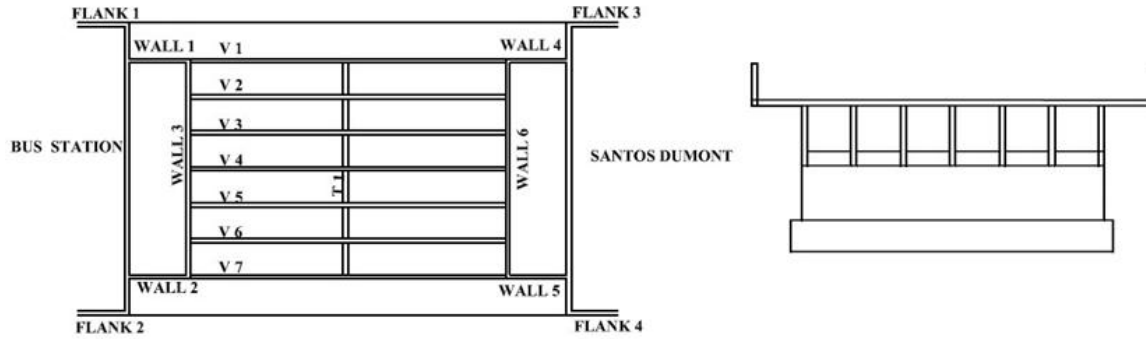


Figure 2. Illustration of structural design for one of the bridges.

demarcation of a rectangular network of 10 points, and Figure 2 shows a schematic of the structural characteristics of one of the bridges tested.

The ultrasound and impact measurements were made at the same 10 points of each network. Two measurement methods were used in this case study: (1) Single ultrasound and rebound hammer measurements at each point of the network, as recommended in NBR 7584/95 (ABNT, 1995), totaling a set of 20 measurements in each network of 10 points; (2) Measurements at each of the 10 points of a series of rectangular networks, with 10 replicates in the ultrasound tests and five replicates in the impact tests, totaling a set of around 150 measurements.

Due to the concrete being a heterogeneous material, the reapplication of ultrasound and rebound hammer measurements were made aiming to increase the reliability of outcomes, since only one measurement at each point would be equivalent to consider it homogeneous, which does not correspond to the actual characteristics of the concrete. The maximum number of impacts was established after compatibilizing the rigidity of the structural part of the test with the impact energy of the hammer. The ten measurements with ultrasound at each point were set to reliably assess the experimental operator errors, mainly because of the various influences of concrete.

Data analysis

The data obtained using Method (1) were analyzed considering only the arithmetic average, following the recommended guidelines (ABNT, 1995). In the case of Method (2), the data were statistically analyzed using the Student's t-test and Fisher's F-test (Schwaab and Pinto, 2007). The objective of the t-test was to identify the existence of a common measurement interval, hence generating a statistical level of confidence for the measurement. The confidence interval for each measurement was calculated using the following equation (Schwaab and Pinto, 2007):

$$t_{N-1} = \frac{\bar{x} - \mu}{\frac{s}{\sqrt{N}}} \tag{1}$$

where N is the number of replicates or experiments, \bar{x} is the sampling mean, s is the standard deviation, and t_{N-1} is the value of the t distribution with $N-1$ degrees of freedom and a 95% confidence level.

Using the variances of the measurements performed by the two techniques, the behavior of the errors was analyzed by applying the

F-test, described by:

$$F_{xy}^* = \frac{\sigma_x^2}{\sigma_y^2} \tag{2}$$

where F_{xy}^* is the calculated value of F, and σ_x^2 and σ_y^2 are the variances of the sampling groups. The value of F_{xy}^* obtained was then compared with the limits established using:

$$\left(\frac{1}{F_{100-p\%}}, v_2, v_1 \right) < F^* < (F_{p\%}, v_1, v_2) \tag{3}$$

where v_1 and v_2 represent the degrees of freedom of the sampling sets analyzed, and $F_{p\%}$ and $F_{100-p\%}$ are the tabulated values of F for a 95% confidence level. Hence, for a 95% level of confidence ($p = 2.5\%$), if the value of F^* (the calculated F value) was greater than $F_{0.025}$ or smaller than $\frac{1}{F_{0.975}}$, and therefore lay outside the

tabulated limit, the errors were not equivalent. It should be pointed out that in all these statistical tests, it was assumed that the experimental data showed normal distributions (Almeida, 1993).

RESULTS

Using measurement method (1)

The measurements made using the rebound hammer and ultrasound techniques at one of the bridges are shown in Figure 3(a and b) and 4 (a and b), respectively. For each pillar, the mean value was calculated from single measurements made at each of the ten sampling points in the network. Similar results were obtained for the other three bridges.

Using measurement method (2)

Figures 5 to 7 show the values obtained for the pillars

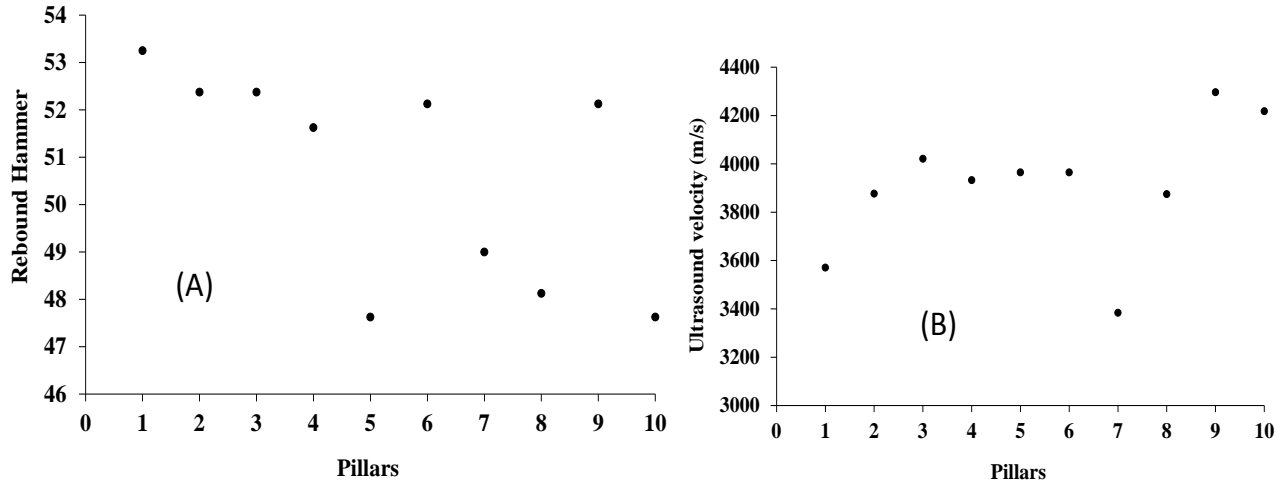


Figure 3. Mean values using data from the method (1) at Bridge 1: (a) Rebound impact; (b) Ultrasound.

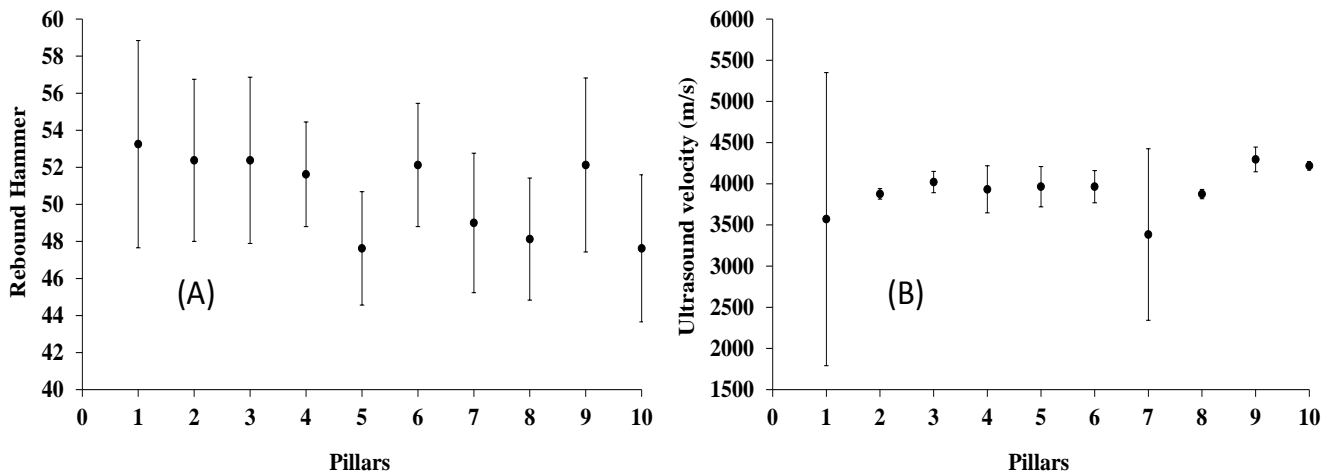


Figure 4. Mean values and confidence intervals with application of the Student's t-test using data from the method (1) at Bridge 1: (a) Rebound impact; (b) Ultrasound.

and stringers of the bridges tested, using ten ultrasound measurements at each of the ten points of the sampling network, followed by five impact measurements at each sampling point, instead of only a single measurement at each point as recommended in the guidelines (ABNT, 1995; Mercosur, 1996). The five impact measurements at each point disobeyed the ABNT NBR 7584 guideline (subsection 4.3.5), which states: "more than one impact at the same point is not permitted. If this occurs, the second reading should not be considered in calculation of the results". In the present case, the pillars and stringers were highly rigid, and the impact energy delivered by the hammer did not cause phenomena such as resonance and vibration, or any significant dissipation of energy. After each impact at the same point, the mark left on the surface was checked for any significant fractures or fissures, as described in subsection 5.6.5 of NM 78:96

(Mercosur, 1996). No such features were observed. Figure 5(e) is the following legend to Figures 5 to 7, relating to items (c) and (d), and the P-X-Y notation means the value of the pillar F calculated between X and Y, in the respective figures. The red and black bars represent the tabulated values of the F test.

DISCUSSION

Using measurement method (1)

The measurements made using the rebound hammer and ultrasound techniques at one of the bridges are shown in Figure 3(a) and (b), respectively. The rebound hammer measurements exceeded an index value of 47 for all pillars. According to the correlation curve for the

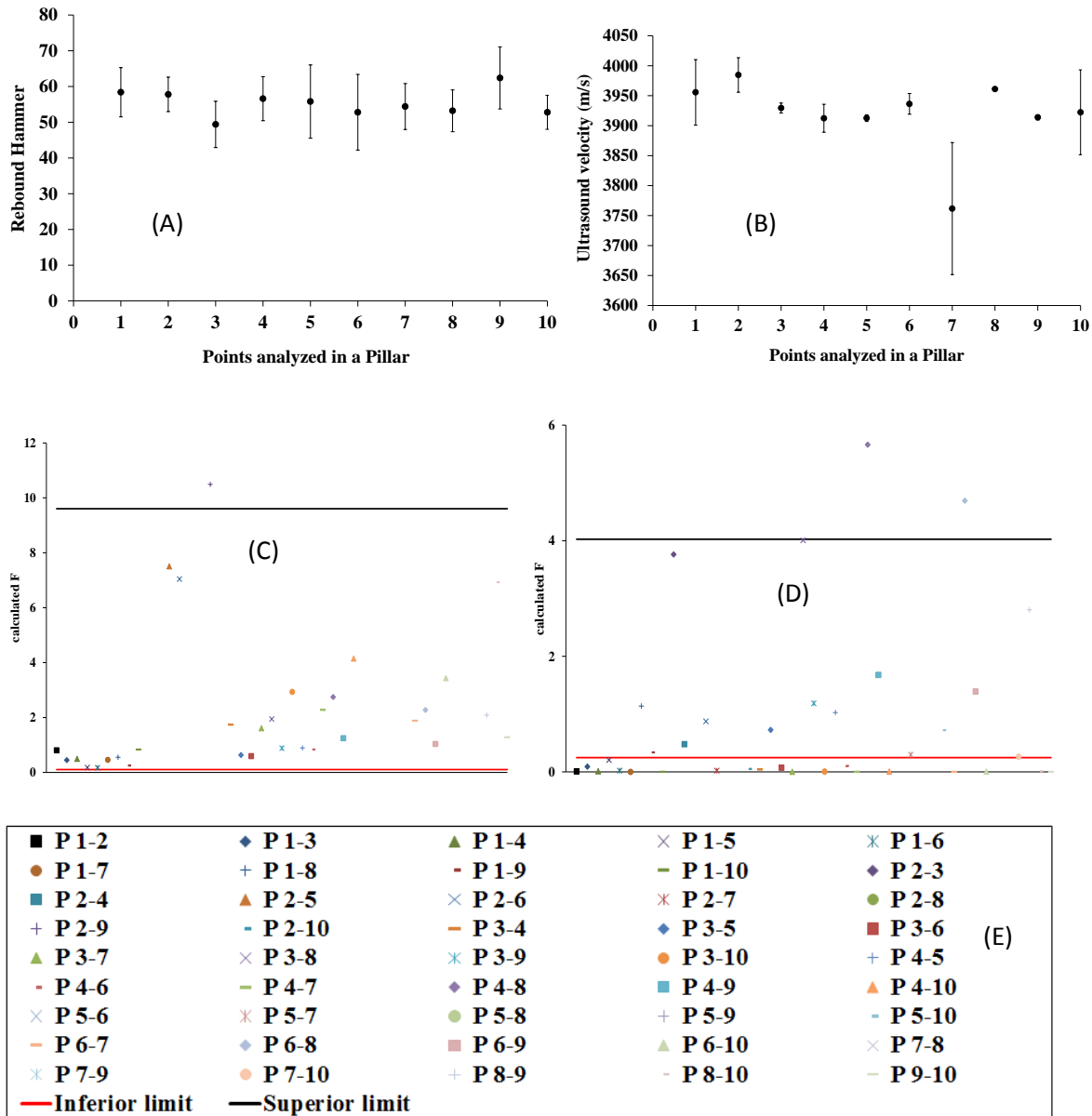


Figure 5. Measurements at a pillar of Bridge 1 for the method 2. a) Rebound Impact; b) Ultrasound; Application of the F-test to the impact (c) and ultrasound (d) data; e) Legend to Figures 5 to 7, relating to items (c) and (d), where the P-X-Y notation means the value of the pillar Fcalculated

instrument, this represented a compressive strength that exceeded 50 MPa. This level of resistance is highly satisfactory in terms of the mechanical performance of the structures tested.

In the case of the ultrasound measurements, no correlation curve was available for the relationship between the resistance and ultrasound velocity. Nonetheless, a mean sound wave propagation velocity of between 3800 and 4000 m/s could be classified as excellent, according to the scale proposed by Cánovas (1998), reflecting high strength of the concrete to compression (higher ultrasound velocity corresponds to

greater mechanical resistance).

The results obtained from the combined use of the two nondestructive techniques, rigorously following technical guidelines, indicated that the quality of the structures and their mechanical resistance to compression were satisfactory in terms of structural safety. However, considerable care must be taken in using mean values alone during the analysis of results. Although this practice is widely reported in the literature, and is common sense in professional activities, the mean does not necessarily represent the most probable experimental value and may not accurately reflect physical reality. Taken alone, the

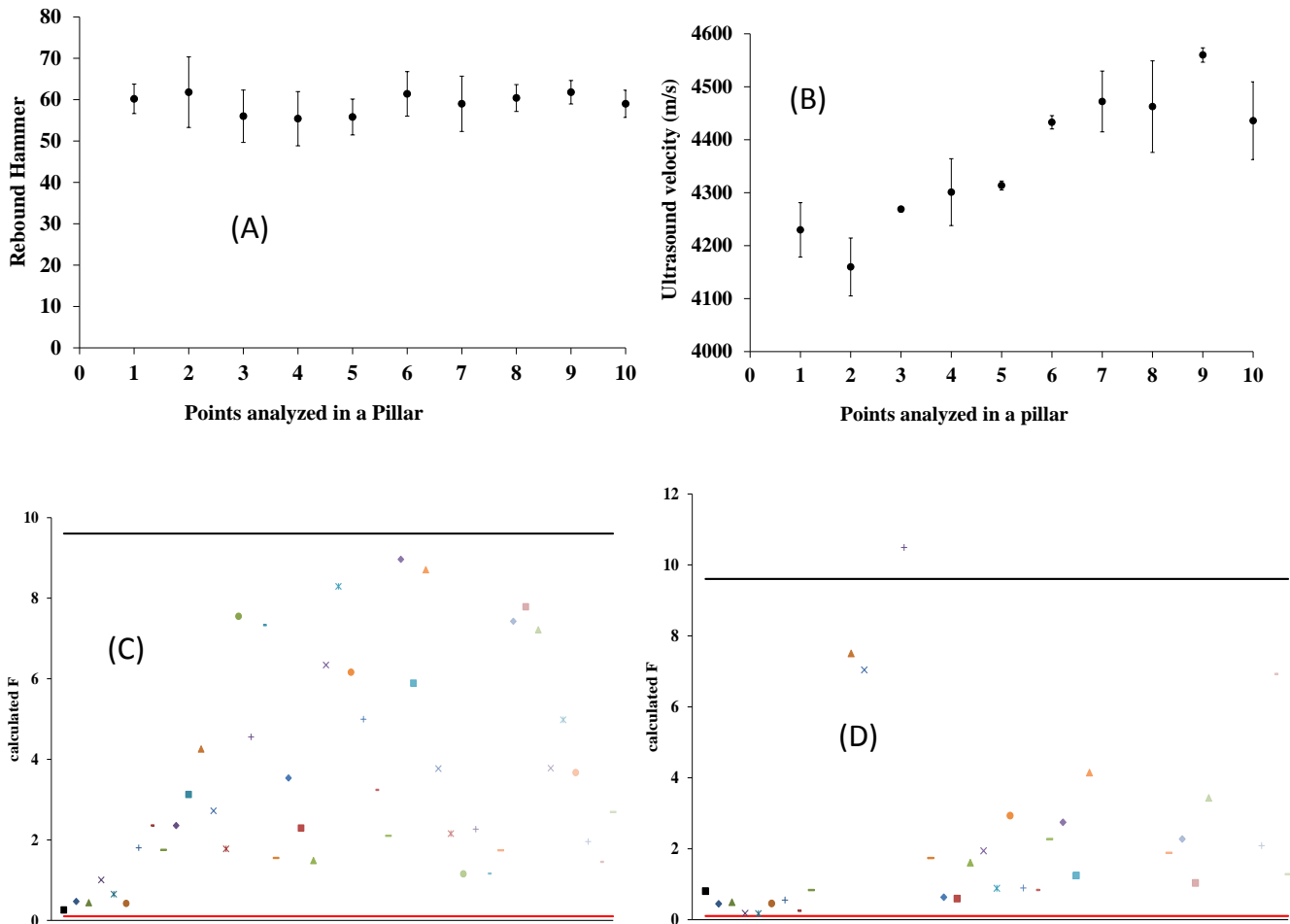


Figure 6. Measurements at a pillar of Bridge 2 for the method 2. a) Rebound Impact; b) Ultrasound; Application of the F-test to the impact (c) and ultrasound (d) data; Legend is available in the Figure 5(e).

mean value has no significance; the associated error must also be taken into consideration (Schwaab and Pinto, 2007). When the same results were analyzed considering the confidence intervals (Figures 4(a) and (b)), there were clear implications for the quality of the concrete of the pillars. The ultrasound results obtained considering only the mean (Figure 3(b)) were indicative of optimum ultrasound velocities (Cánovas, 1998). Meanwhile, observation of the variability of the measurements around the mean (the confidence interval) for pillars 1 and 7 (Figure 4(b)) revealed that in these cases, the quality of the concrete could be classified as being between optimum and satisfactory, according to the scale given by Cánovas (1998). Despite the importance of considering uncertainties in the measurements, in day-to-day practice these are often ignored (Taylor, 2012), which can lead to interpretations that are erroneous.

In addition to the obvious consequences that could occur when results are analyzed using only mean values, the Method 1 has another failing: it considered the sum of

the values for the sampling network. For the procedure adopted it would not be possible to use the values sum, the mean and the confidence interval, which demand a homogeneous sample. It could not provide a statistical guarantee that the values obtained throughout the sampling network were the same, especially because is unlikely that concrete could be homogeneous throughout the pillar or stringer.

In order to use the sum of these measurements, they should be repeated at each point in the sampling network, in order to permit subsequent use of statistical procedures (t-tests and F-tests) to evaluate the homogeneity of the means and the errors (this is discussed below for the results obtained using the second measurement protocol). Analysis of the quality of concrete can therefore be compromised either by adopting a surface measurement technique, such as rebound impact tests or even by failing to apply a simple statistical analysis. At the present case rebound impact indicated similar mechanical behavior for all the pillars (Figure 4(a)), while the ultrasound data clearly identified

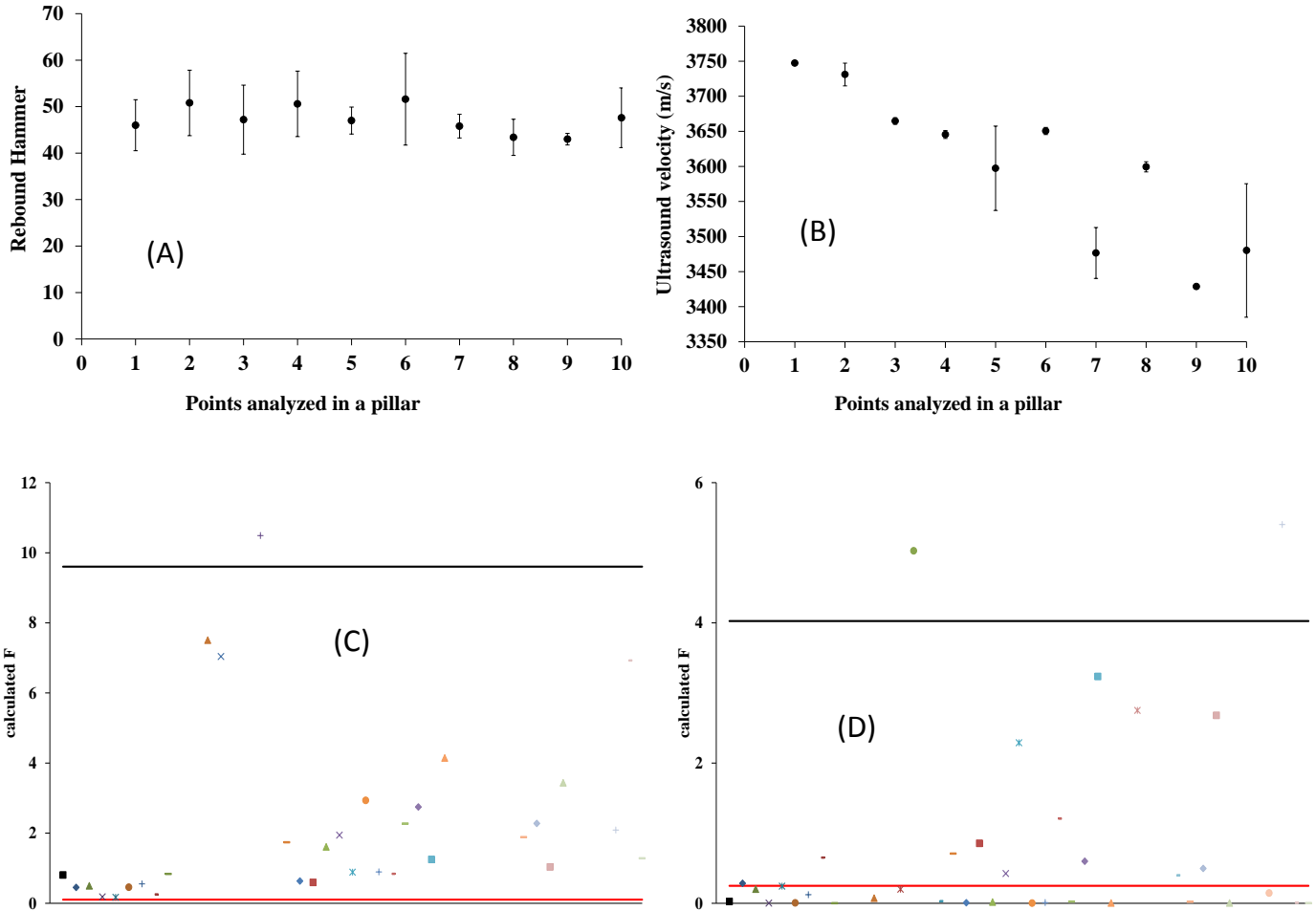


Figure 7. Measurements at a pillar of Bridge 3 for the method 2. a) Rebound Impact; b) Ultrasound; Application of the F-test to the impact (c) and ultrasound (d) data; Legend is available in the Figure 5 e).

problems in the quality of the concrete in pillars 1 and 7, compared to the other pillars (Figure 4(b)). The limitations of the Method 1 were the motivation to propose a different set of measurements, Method 2, to obtain a statistical guarantee for the results.

Using measurement method (2)

In the case of the rebound hammer measurements, the confidence intervals of the means overlapped (Figures 5(a), 6(a), and 7(a)). Based on the t-test with 95% confidence, it could therefore be concluded that the measurements at the different pillars were equivalent in terms of the mean. Nonetheless, in using the sum of all the values obtained for the sampling network, it was necessary to evaluate the errors using the F-test (Figures 5(c), 6(c), and 7(c)). The values of $F_{calculated}$ lay within the tabulated limits (Figure 8), indicating that the errors were equivalent, so it was therefore possible to use the sums of all the measurements.

The ultrasound results showed a very different behavior compared to the rebound hammer data, as shown in Figures 5(b), 6(b), and 7(b). The measurements at the different points of the sampling network were clearly not homogeneous. Considering only a single repetition of each measurement was not possible to sum all the ultrasound results to obtain a representative mean. In addition to the means not being equivalent for the ultrasound data, the errors also showed the same behavior. It can be seen from Figures 5(d), 6(d), and 7(d) that the calculated values of F lay outside the tabulated limits, indicating that the variability was different for each point on the pillar. According to the impact data, the concretes were homogeneous, with satisfactory performance in terms of structural safety and quality of the construction. The conclusion of the technical diagnosis would be that the structures were acceptable without interventions. On the other hand, the ultrasound results revealed divergent behavior, highlighting the fact that the structures were not homogeneous throughout their composition. Internal defects that can lead to

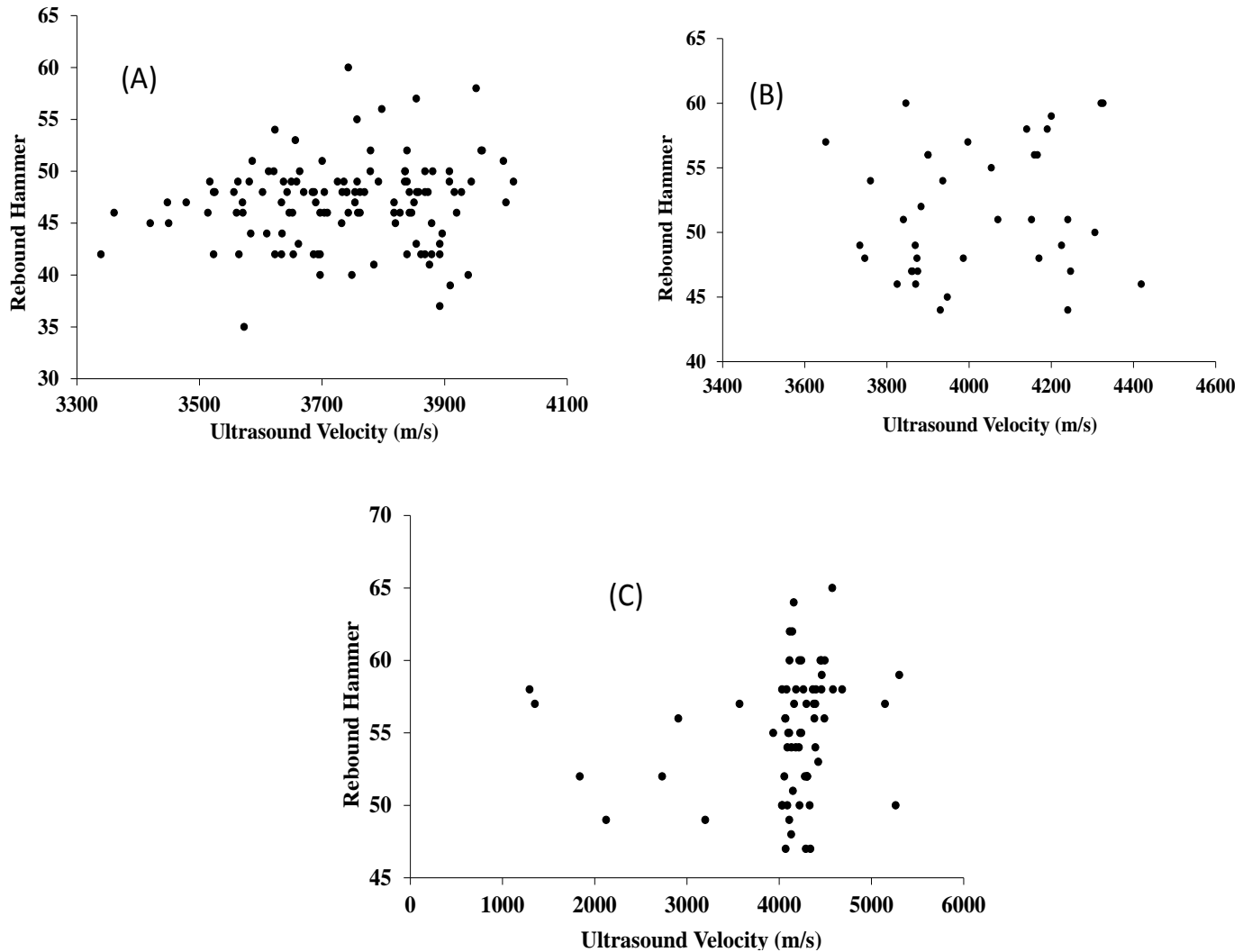


Figure 8. Scatter plots of the means obtained using ultrasound and rebound hammer measurements at the three bridges: bridge 1 (a); bridge 2 (b) and bridge 3 (c).

unsatisfactory structural conditions include the presence of void spaces, cracks, and corrosion. The analysis of experimental errors substantiate this conclusion.

Analysis of the correlation between the rebound hammer and ultrasound data

The distributions of the points representing the means for the measurements made at the bridges using ultrasound and rebound are shown in Figure 8. In contrast to earlier findings (Almeida, 1993), the distributions obtained here using real field measurements at four bridges indicated that it was not possible to establish a correlation model describing the relation between the rebound hammer and ultrasound techniques. In previous field measurements, Hamidian et al., (2012) obtained correlation coefficients (R^2) of 0.0275 and 0.0115, indicating a lack of correlation

between ultrasound and rebound hammer methods. This lack of correlation can largely be explained by the obvious differences between the principles of the techniques and the physical properties measured, together with the errors and uncertainties inherent in any method, whose variability during the course of measurements should not be ignored in order to avoid compromising the reliability of the results.

Conclusions

The use of combined nondestructive techniques in concrete quality evaluation is recommended, as this procedure can increase the reliability of results in the presence of variable experimental errors. Meanwhile, consideration should be given to the fact that experimental errors can vary significantly across the areas tested. The

results presented here demonstrate that it is not possible to achieve a reliable technical evaluation, whether using ultrasound or rebound, without taking into account the variability of the uncertainties (errors) during the course of the test procedures. Failure to consider these uncertainties, could lead to erroneous conclusions during the evaluation of concrete quality and an inability to predict the safety of structures.

In contrast to other studies, no correlation was observed between the results of measurements of conventional concretes made using rebound and ultrasound. Certain aspects of the NBR 7584 (ABNT, 1995) and NM 78:96 (Mercosur, 1996) guidelines concerning surface hardness may require reappraisal, especially concerning the use of arithmetic means and the drawing of conclusions from tests employing impact hammers to determine the compression resistance of concrete. The present findings suggest that the use of the impact technique should be restricted to the analysis of the surface characteristics of concrete. The method is unable to provide a reliable evaluation of the mechanical properties of structural components as a whole, especially in the absence of statistical tools to determine the levels of uncertainty.

Conflict of Interest

The author(s) have not declared any conflict of interests.

ACKNOWLEDGEMENTS

The authors are grateful for the support provided by the Brazilian agencies: PRONEX/CNPq/FAPITEC, CAPES/PROENGENHARIA/PROCADA and INOVATEC/FINEPE for their financial support.

REFERENCES

- Almeida IR (1993). Employment rebound hammer and ultrasound to effect a qualitative evaluation of high performance concrete. Brazil Federal Fluminense University. PhD Thesis, 139 p.
- American Society for Testing and Materials (1993). Test for rebound number of hardened concrete. ASTM C 805-85.
- American Society for Testing and Materials (2002). Standard test method for pulse velocity through concrete. ASTM C 597.
- Brazilian Association of Technical Standards (1994). Hardened concrete - Determination of the propagation speed of the ultrasonic wave. ABNTNBR 8802.
- Brazilian Association of Technical Standards (1995). Evaluation of surface hardness. ABNT NBR 7584.
- Breyse D, Soutsos M, Felicetti R, Krause M, Lataste JF, Moczko A (2009). How to improve the quality of concrete assessment by combining several NDT measurements. Nantes, France NDTCE'09, Non-destructive Testing in Civil Engineering. June 30th–July 3rd.
- Breyse AD (2012). Non-destructive evaluation of concrete strength: A historical review and new perspective by combining NDT methods. *Constr. Build. Mater.* 33:39-163. <http://dx.doi.org/10.1016/j.conbuildmat.2011.12.103>
- British Standards (1986). Recommendations for surface hardness tests by the rebound hammer. BS 1881: Part 202.
- Box GEP, Hunter WG, Hunter JS (2005). *Statistics for Experimenters*. New York John Wiley & Sons. 2nd edition. PMID:PMC1273458
- Cánovas MF (1998). *Pathology and Therapy of Concrete*. Brazil Ed. PINI. 522 p.
- Cerqueira HS, Rawet R, Pinto JC (1999). The influence of experimental errors during laboratory evaluation of FCC catalysts. *Applied Catalysis A*. 181:209-220. [http://dx.doi.org/10.1016/S0926-860X\(99\)00004-6](http://dx.doi.org/10.1016/S0926-860X(99)00004-6)
- Hamidian M, Shariati A, Khanouki MMA, Sinaei H, Toghroli A, Nouri K (2012). Application of Schmidt rebound hammer and ultrasonic pulse velocity techniques for structural health monitoring. *Sci. Res. Essays* 7(21):1997-2001.
- Larentis AL, Bentes Jr. AMP, Resende NS, Salim VMM, Pinto JC (2003). Analysis of experimental errors in catalytic tests for production of synthesis gas. *Appl. Catal. A*. 242:365-379. [http://dx.doi.org/10.1016/S0926-860X\(02\)00525-2](http://dx.doi.org/10.1016/S0926-860X(02)00525-2)
- Machado MD, Shehata LCD, Shehata IAEM (2009). Correlation curves to characterize concretes used in Rio de Janeiro- Brazil by means of non-destructive tests. *Brazil Ibracon Struct. Mater. J.* 2(2):100-123.
- Mahure NV, Vijh GK, Sharma P, Sivakumar N, Ratnam M (2011). Correlation between pulse velocity and compressive strength of concrete. *Int. J. Earth Sci. Eng.* 4(6):871-874.
- Mercosur Committee for Standardization (1996). Hardened concrete - Evaluation of surface hardness by rebound hammer. NM 78:96.
- Mohammed BS, Azmi NJ, Abdullahi M (2011). Evaluation of rubbercrete based on ultrasonic pulse velocity and rebound hammer tests. *Constr. Build. Mater.* 25:1388-1397. <http://dx.doi.org/10.1016/j.conbuildmat.2010.09.004>
- Nguyen NT, Sbartaï ZM, Lataste JF, Breyse D, Bos F (2013). Assessing the spatial variability of concrete structures using NDT techniques- laboratory tests and case study. *Constr. Build. Mater.* 49:240-250. <http://dx.doi.org/10.1016/j.conbuildmat.2013.08.011>
- Schwaab M, Pinto JC (2007). *Analysis of Experimental Data 1: Fundamentals of Statistics and Parameter Estimation*. E-papers. Brazil, Rio de Janeiro. [http://translate.googleusercontent.com/translate_c?depth=1&hl=en&rev=/search%3Fq%3DSchwaab,%2BM.,%2BPinto,%2BJ.C%2B\(2007\)&rurl=translate.google.com.ng&sl=pt-BR&u=http://www.e-papers.com.br/produtos.asp%3Fcodigo_produto%3D1253&usg=ALkJrh1vpzKPVpgYT2j-PMoScdvnFVDtw](http://translate.googleusercontent.com/translate_c?depth=1&hl=en&rev=/search%3Fq%3DSchwaab,%2BM.,%2BPinto,%2BJ.C%2B(2007)&rurl=translate.google.com.ng&sl=pt-BR&u=http://www.e-papers.com.br/produtos.asp%3Fcodigo_produto%3D1253&usg=ALkJrh1vpzKPVpgYT2j-PMoScdvnFVDtw)
- Severo Jr. JB, Pinto JC, Ferraz HC, Alves TLM (2011). Analysis of experimental errors in bioprocesses. 1. Production of lactobionic acid and sorbitol using the GFOR (glucose-fructose oxidoreductase) enzyme from permeabilized cells of *Zymomonas mobilis*. *J. Industr. Microbiol. Biotechnol.* 38:1575-1585. <http://dx.doi.org/10.1007/s10295-011-0948-1>; PMID:21328074
- Shariati M, Ramli-Sulong NH, Arabnejad KHMM, Shafiqh P, Sinaei H (2011). Assessing the strength of reinforced concrete structures through ultrasonic pulse velocity and Schmidt rebound hammer tests. *Sci. Res. Essays* 6(1):213-220.
- Soriano J, Gonçalves R, Bertoldo C, Trinca AJ (2011). Applications rebound hammer test pieces *Saligno eucalyptus*. Brazil. *J. Agric. Environ. Eng.* 9(3):322-328.
- Taylor JR (2012). *Introduction to Error Analysis - The Study of Uncertainties in Physical Measurements*. Bookman (2nd ed).
- Sbartaï ZM, Breyse D, Larget M, Balayssac JP (2012). Combining NDT techniques for improved evaluation of concrete properties. *Cement and Concrete Composites.* 34:725-733. <http://dx.doi.org/10.1016/j.cemconcomp.2012.03.005>

Full Length Research Paper

Comparative osteometric differences in humerus of bari Goat and Dumbi Sheep

Ghulam Murtaza Lochi^{1*}, Muhammad Ghasuddin Shah¹, Illahi Bux Kalhoro¹, Jameel Ahmed Gandahi¹, Muhammad Shoaib Khan¹, Abdul Haseeb¹, Sheeraz Mustafa Khushk², Ameet Oad³ and Mansoor Ibrahim Ansari⁴

¹Department of Anatomy and Histology, Faculty of Animal Husbandry and Veterinary Sciences, Sindh Agriculture University, Tandojam, Pakistan.

²Department of Animal Reproduction, Faculty of Animal Husbandry and Veterinary Sciences, Sindh Agriculture University, Tandojam, Pakistan.

³Department of Surgery and Obstetrics, Faculty of Animal Husbandry and Veterinary Sciences, Sindh Agriculture University, Tandojam, Pakistan.

⁴Faculty of Animal Husbandry and Veterinary Sciences, Sindh Agriculture University, Tandojam, Pakistan.

Received 24 January, 2014; Accepted 12 March, 2014

Morphological studies were conducted on the Humerus of 60 clinically healthy animals (30 Bari goat and 30 Dumbi sheep) of both sexes, slaughtered at Tandojam and Tando Allahyar abattoirs. For comparative study, animals were divided in three age groups viz., lambs/kids (6-9 months), yearlings (13-21 months) and adult (21-24 months). The estimated age was determined through dental formula, whereas, the body weight was obtained using spring balance. For collection and preparation of specimen standard procedures were adopted. The weight (Mean± SEM) of right and left humerus of three age groups of Bari goat and Dumbi sheep is found to be 26.66±0.23, 34.06±0.33, 46.44±0.44, 31.29±0.83, 47.20±1.27, 53.62±0.66, 26.54±0.34g, 34.87±0.40, 46.47±2.64, 31.32±0.83, 47.56±0.60 and 53.57±0.53 g, respectively. Statistical analysis revealed significant difference (p<0.05) between the kid/lamb and yearling groups but no significant difference between adult groups of both species. It is further revealed that the bones of sheep are generally heavier than goat. The mean ± SEM length of right and left humerus from three age groups of goat and sheep calculated as 11.51±0.92, 13.77±0.08, 16.61±0.11, 10.08±0.15, 12.93±0.13 and 14.63±0.12cm, respectively. The statistical analysis revealed a highly significant difference (P<0.01) between kid/lamb and yearling groups, but no statistical difference (p>0.05) in between and among the adult groups of both species. The Bari goat possess relatively longer humerus than those of the Dumbi sheep. Mean values for breadth of proximal end (Bpe), breadth of distal end (Bde) and circumference of right and left humerus from three age groups of Bari goat and Dumbi sheep showed statistical differences between the age groups but no statistical difference was noted among two species and sexes.

Key words: Osteometric, differences, humerus, Bari goat, Dumbi sheep.

INTRODUCTION

Livestock represents an important component of the agricultural sector in Pakistan (Mohammad, 2007). It

*Corresponding author. E-mail: drgmlochi@gmail.com

Author(s) agree that this article remain permanently open access under the terms of the [Creative Commons Attribution License 4.0 International License](http://creativecommons.org/licenses/by/4.0/)

accounts 55.1% of the agriculture value added and 11.5% to gross domestic production (GDP) during 2010-12. Livestock has witnessed a marginally higher growth of 4.0% against the growth of 3.97 percent last year (Anonymous, 2011-12).

The domestic goat (*Capra aegagrus hircus*) is a subspecies of wild goat of Southwest Asia and Eastern Europe (Hrist and Kris, 2008). Pakistan is rich in goat genetic resource and it is the third largest goat producing country in the World after China and India (Anonymous, 2010-11).

Pakistan has about 34 goat breeds (Isani and Baloch, 1996; Khan and Ashfaq 2012). The major objective of goat rising is meat, while milk obtained from goat is consumed by human being and hairs are used domestically for producing rugs by poor or needy families (Khan et al., 2008). Goat population of Pakistan is 63.1 million and breeds are generally categorized as meat, dairy and hairy types (Anonymous, 2011-12). Sindh Province includes Bari, Chhappar, Kamori, Sindh Desi, Bujri, Jattan, Kacchan, Kurri, Kurri, Lohri, Lehri, Pateri, Tapri or Lappi, Tharki or Tharri in Sindh (Anonymous, 2003-04).

There are 30 breeds of sheep in Pakistan (Isani and Baloch, 1996). Sheep population of Pakistan is about 28.4 million heads (Anonymous, 2011-12). Sheep is an important source of food (meat and milk) as well as of other products of high economic value, such as wool and leather (Tariq et al., 2011). Most famous breeds of sheep include Dumbi, Kachhi and Kooka in Sindh province (Anonymous, 2003-04). The total milk production is around 46.4 million tons and out of this, sheep contribute 0.04 million tons (Anonymous, 2010-11). Wool yield per head is 1.4 kg per annum (Shah et al., 2001).

Bari (Barbari) breed is predominantly utilized as meat and milk purpose especially in Sindh and Punjab. The population of Bari goat is 2.3 million heads. This breed of goat is found in Hyderabad, Dadu, Larkana Khairpur, Nawabshah and Jacobabad districts of Sindh. A compact body, pointed horns, head with a long narrow snout, small, straight and erect ears are prominent features of this breed. The body color of goat is usually white and brown or spotted. Body weight of adult male and female is 23 and 20 kg, respectively and the milk yield is 100 L / lactation of 110 days (Shah et al., 2001; Khan et al., 2008).

The skeletal system stands out as one of the body structures has been used for the characterization of different species of animals (Guintard and Lallemand, 2003). The natural morphological development of bones and joints is very important for the diagnosis of skeletal diseases in young animals (Makkaway et al., 1988). The development morphology of animals shows considerable variation with respect to breed, age, sex, nutritional situation and environmental factors among others (Outram and Conwy, 1998). Some researchers depended on limb bone length to estimate the late fetal and prenatal age (Schewers et al., 1980). The study of the appearance of

limb ossification centers provide great aids in age estimation during prenatal life and assessment of fetal bone maturation and helps in the detection of some fetal abnormalities (Oishi et al., 1996). Morphologically examination of long bones provides rather significant insights into intra-species as well as interspecies differences.

MATERIALS AND METHODS

The findings of the present study will provide baseline data because osteological characteristics are often used to identify animal species rather in three different stages in a cheap and rapid manner. Further present study will also be helpful in performing orthopedic surgery in small ruminants.

Specimen collection

This experimental study was performed on the 60 clinically healthy animals (30 Bari goat 30 Dumbi sheep) of either sex slaughtered at Tandojam and Tando Allahyar abattoirs Sindh Pakistan abattoirs during 2011-12. These animals were divided in three (10 animals in each group) groups according to the age. The estimated age was noted through dental formula (Vatta et al., 2006) and body weight was determined by using spring balance. Physical examination of all animals was conducted for any sign of deformity before the right and left pectoral or forelimbs were harvested.

Preparation of specimen for maceration

The soft tissues attached to the long bones of forelimbs such as muscles, fascia, tendons and ligaments were removed with scalpel and scissors. The long bones such as humerus, radius and ulna and metacarpal from forelimbs of both species were separated. The specimens were then arranged into two macerating buckets, one for goat and the other for sheep. Tap water was added to submerge the specimen. This process was allowed to stay bones for 3 days after which the water was changed. Further, 1 to 1.5 Mol of Potassium Hydroxide (KOH) was added to facilitate total removal of remaining soft tissues from bones. This process is known as maceration. The macerated bones were dried for 2 to 3 days after which they were boiled for 5 to 6 h with detergent until unless to remove bone marrow and fat. The bones were allowed to dry for the second time for 2 to 3 days on sunlight.

Measurement of the bones

Weight of the bones was obtained in grams by using a sensitive electronic balance. Length and other measurements of the long bones was measured by using a measuring tape as revealed by Salami et al. (2011). Diameter of the bone extremities and the mid shaft was measured in millimeters using Vernier calliper (Siddiqui et al., 2008). The result thus obtained was converted to centimeters.

The circumferences of the bones were taken using a thread. The weight, breadth of proximal end (Bpe), breadth of distal end (Bde), depth of olecranon (Do), depth of process anconaeus (Dpa), circumference (Cr), and length of all long bones were measured. All recorded weights, lengths and diameters were expressed as mean \pm SEM (Standard Error of Mean) and further statistically analyzed by using Statistical Package for Social Sciences (SPSS) version 17.0. For paired samples t-test at 95 and 99% confidence interval

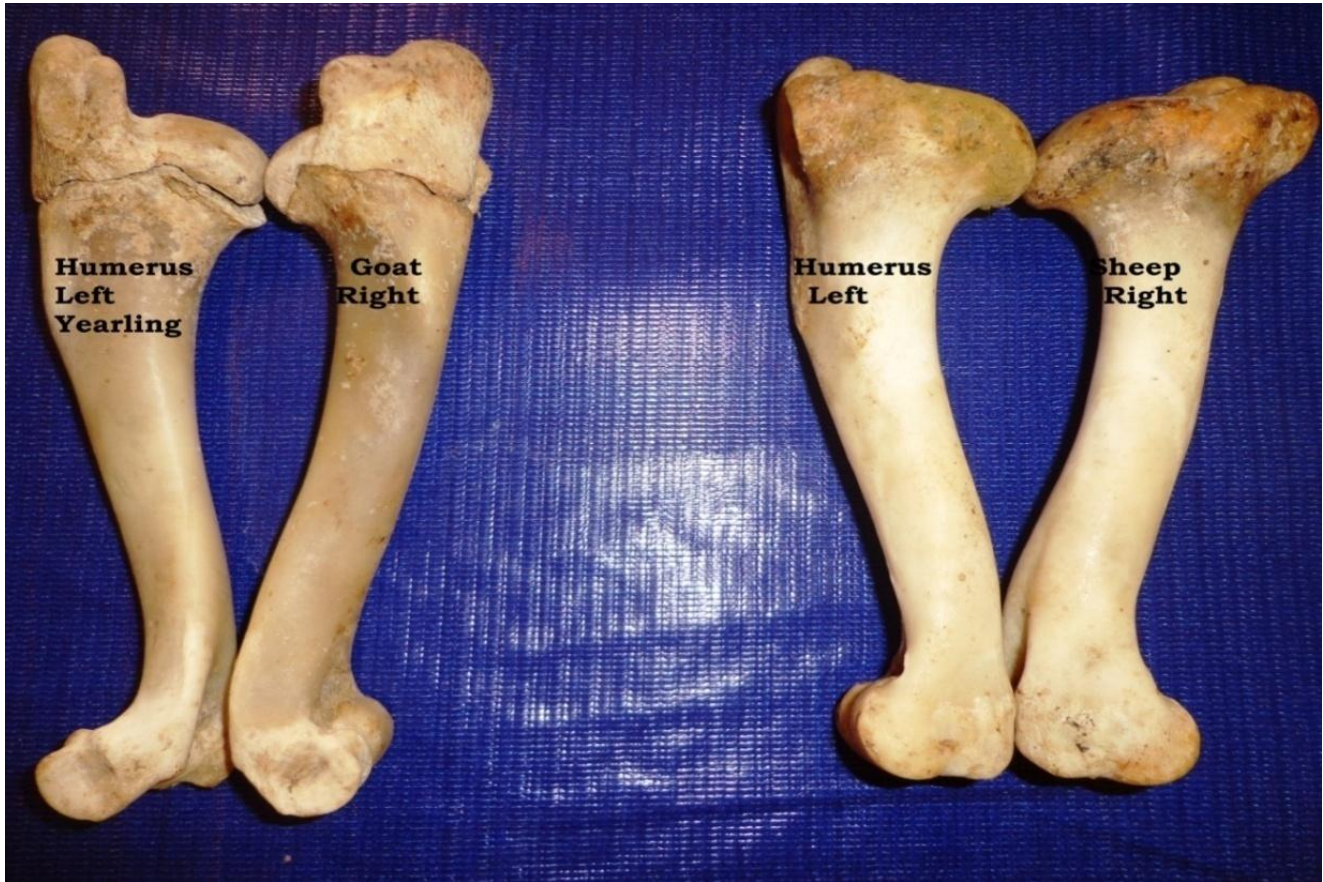


Plate 1. Left and right humerus of Bari goat and Dumbi sheep (Lateral view).

was used to determine the level of significance between the three age groups of two species.

RESULTS

Present study addresses morphological and osteometric data of long bones of pectoral limb from 30 Bari goat and 30 Dumbi sheep. The studied animals of both species were divided in three age groups namely lambs/ kids, yearling and adults. The weight, Breadth of proximal end (Bpe), breadth of distal end (Bde), depth of olecranon (Do), depth of process anconaeus (Dpa), circumference (Cr), and length of all long bones were measured. All recorded weights, lengths and diameters were expressed as mean \pm SEM (Standard Error of Mean) and further statistically analyzed by using Statistical Package for Social Sciences (SPSS) version 17.0. For paired samples t-test at 95 and 99% confidence interval was used to determine the level of significance between the three age groups of two species.

Morphometry of long bones

The right and left humerus of Bari goat and Dumbi sheep

were observed in study. Bones were collected randomly from both sexes.

Weight

The humerus is one of the long bones situated in proximal end of forelimb at an angle downward and backward; forms shoulder joint proximally with the scapula and elbow joint distally with the radius and ulna (Plate 1). The weight (Mean \pm SEM) of right humerus of three age groups of Bari goat and Dumbi sheep is shown in Figure 1, as 26.66 \pm 0.23, 34.06 \pm 0.33, 46.44 \pm 0.44, 31.29 \pm 0.83, 47.20 \pm 1.27, and 53.62 \pm 0.66 g, respectively. Statistical analysis revealed significant difference ($p < 0.05$) between the kid/lamb and yearling groups but no significant difference between adult groups of both species. It is further revealed that the bones of sheep are statistically heavier than goat.

The differences calculated in the mean weight of left humerus (Figure 2) of three age groups of Bari goat and Dumbi sheep were, kids 26.54 \pm 0.34 g, yearling 34.87 \pm 0.40 g and adults 46.47 \pm 2.64 g and lambs 31.32 \pm 0.83 g, yearling 47.56 \pm 0.60 g and adult 53.57 \pm 0.53 g, respectively.

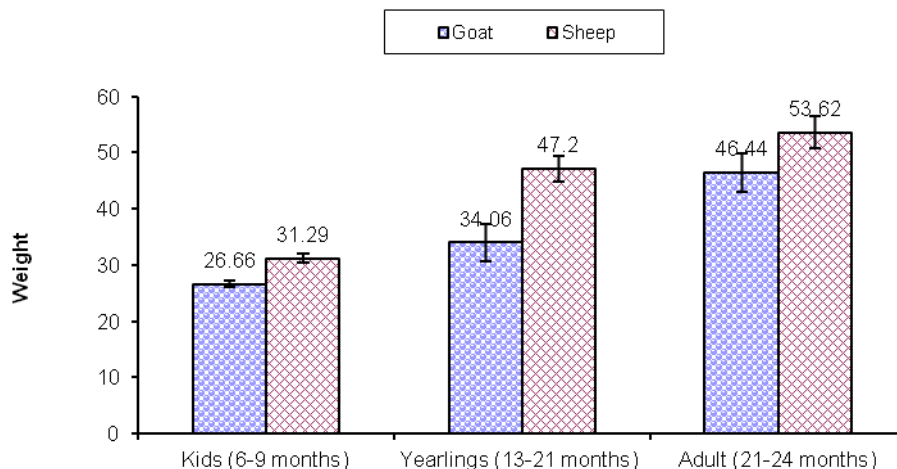


Figure 1. Mean \pm SEM of absolute weight of right humerus (g) of different age groups in Bari goat and Dumbi sheep.

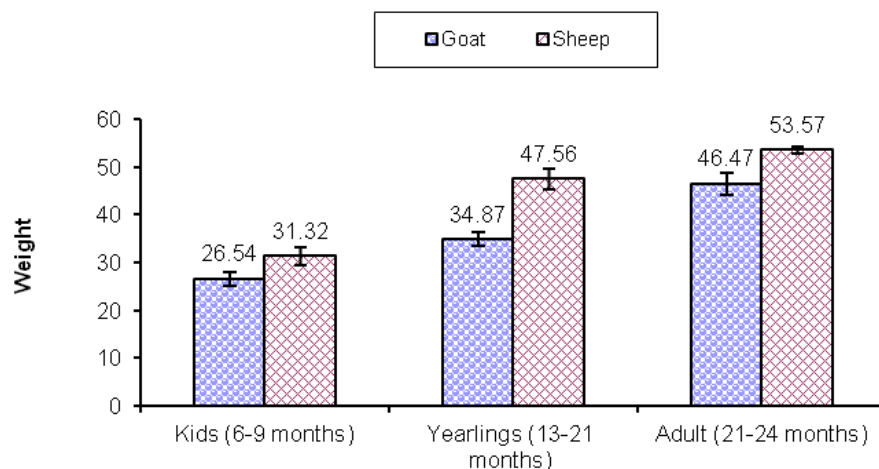


Figure 2. Mean \pm SEM of absolute weight of left humerus (g) of different age groups in Dumbi sheep and Bari Goat.

Statistically significant difference ($P < 0.05$) was observed in between kid/lamb and yearling groups. However, no statistical difference was calculated between adults groups of both species.

Breadth of proximal end (Bpe)

Mean values for breadth of proximal end (Bpe) of right humerus of kid, yearling and adult are 2.55 ± 0.06 , 3.48 ± 0.05 and 3.74 ± 0.10 cm, respectively and that of sheep are 2.74 ± 0.12 , 3.38 ± 0.06 and 3.88 ± 0.05 cm, respectively. The statistical analysis proved that there is no significant difference in between yearling and adult groups of two species. However, a significant difference ($P < 0.05$) is noted among kid/lamb group (Table 1).

Whereas, the Bpe measurements (Mean \pm SEM) of left humerus of goat and sheep are measured as 2.51 ± 0.09 , 3.40 ± 0.06 , 3.71 ± 0.06 and 2.78 ± 0.12 , 3.73 ± 0.09 and 3.86 ± 0.06 cm, respectively (Table 1). Statistically no significant difference is found in between the adult group, but significant difference ($P < 0.05$) revealed among kid/lamb and yearling age groups of two species.

Breadth of distal end (Bde)

The breadth (mean \pm SEM) of distal end of right humerus in three age groups of both species were found to be 2.39 ± 0.07 , 2.70 ± 0.04 , 2.82 ± 0.06 cm and 2.52 ± 0.11 , 2.83 ± 0.08 and 2.89 ± 0.12 cm, respectively. Statistical observation shows that there was no significant

Table 1. Osteometric values (Mean \pm SEM) of right and left humerus of Bari goat and Dumbi Sheep.

Variable	Right Humerus		Left Humerus	
	Bari Goat	Dumbi sheep	Bari Goat	Dumbi Sheep
Weight (g)				
Kid	26.66 \pm 0.23 ^a	31.29 \pm 0.83 ^b	26.54 \pm 0.34 ^a	31.32 \pm 0.83 ^b
Yearling	34.06 \pm 0.33 ^a	47.20 \pm 1.27 ^b	34.87 \pm 0.40 ^a	41.56 \pm 0.60 ^b
Adult	46.44 \pm 0.44 ^a	53.62 \pm 0.66 ^b	46.47 \pm 2.64 ^a	53.57 \pm 0.53 ^b
Bpe				
Kid	2.55 \pm 0.06 ^a	2.74 \pm 0.12 ^b	2.51 \pm 0.09 ^a	2.78 \pm 0.12 ^b
Yearling	3.48 \pm 0.05 ^a	3.38 \pm 0.06 ^a	3.40 \pm 0.06 ^a	3.37 \pm 0.09 ^a
Adult	3.74 \pm 0.10 ^a	3.88 \pm 0.05 ^a	3.71 \pm 0.06 ^a	3.86 \pm 0.06 ^a
Bde				
Kid	2.39 \pm 0.07 ^a	2.52 \pm 0.11 ^b	2.35 \pm 0.05 ^a	2.52 \pm 0.11 ^b
Yearling	2.70 \pm 0.04 ^a	2.83 \pm 0.08 ^a	2.70 \pm 0.06 ^a	2.81 \pm 0.10 ^a
Adult	2.82 \pm 0.06 ^a	2.89 \pm 0.12 ^a	2.84 \pm 0.04 ^a	2.92 \pm 0.08 ^a
Circumference				
Kid	3.63 \pm 0.09 ^a	3.76 \pm 0.07 ^a	3.65 \pm 0.13 ^a	3.75 \pm 0.15 ^a
Yearling	4.58 \pm 0.03 ^a	4.88 \pm 0.03 ^a	4.61 \pm 0.12 ^a	4.88 \pm 0.04 ^a
Adult	5.36 \pm 0.10 ^a	6.22 \pm 0.14 ^b	5.37 \pm 0.16 ^a	6.26 \pm 0.10 ^b

Means with different superscripts in the same row differ ($P < 0.05$); Bpe=Breadth of proximal extremity; Bde=Breadth of distal extremity.

difference in between yearling and adult age groups, but a highly significant difference ($P < 0.01$) is calculated among kid/lamb and adult groups (Table 1).

Whereas, the values for left humerus of kid, yearling and adult is found to be 2.55 \pm 0.05, 2.70 \pm 0.06 and 2.84 \pm 0.04cm respectively and in sheep 2.52 \pm 0.11, 2.81 \pm 0.10 and 2.92 \pm 0.08 cm, respectively. Statistical analysis showed no significant difference present in between kid/lamb and adult groups, but a highly significant difference ($P < 0.01$) is found among yearling groups of two species as indicated in the Table 1.

Length

From the present study, it is observed that the mean \pm SEM length of right humerus from three age groups of goat are 11.51 \pm 0.92, 13.77 \pm 0.08, 16.61 \pm 0.11 cm, respectively, whereas, that of sheep are 10.08 \pm 0.15, 12.93 \pm 0.13 and 14.63 \pm 0.12cm, respectively. The statistical analysis revealed a significant difference ($P < 0.05$) between kid/lamb group and highly significant difference ($P < 0.01$) between yearling, but no statistical difference in adults group of both species. The Bari goat possess relatively longer humerus than those of the Dumbi sheep (Figure 3).

The values regarding mean \pm SEM length of left humerus of both goat and sheep are to be 11.51 \pm 0.23, 13.76 \pm 0.04 and 16.06 \pm 0.17 cm, and 10.75 \pm 0.15, 12.98 \pm 0.14 and 14.20 \pm 0.20 cm, respectively. Statistical analysis revealed significant difference ($P < 0.05$) in kid/lamb and yearling groups whereas no statistical difference was found in adult groups of Bari goat and Dumbi sheep as depicted in the Figure 4.

Circumference

The data regarding circumference at mid shaft of right humerus is presented in Table 1. The mean \pm SEM values for three groups in Bari goat found to be 3.56 \pm 0.09, 4.58 \pm 0.03 and 5.36 \pm 0.10 cm, respectively. Whereas, in sheep it is calculated to be 3.76 \pm 0.07, 4.88 \pm 0.03 and 6.22 \pm 0.14 cm, respectively. The statistical analysis revealed no significant difference ($P > 0.05$) in between the kid/lamb and yearling groups. However, a significant difference was observed among the adult groups of goat and sheep.

The values (mean \pm SEM) for circumference at mid shaft of left humerus is calculated to be 3.65 \pm 0.13, 4.61 \pm 0.12 and 5.37 \pm 0.16 cm, and 3.75 \pm 0.15, 4.88 \pm 0.04 and 6.26 \pm 0.10 cm in three age groups of studied goat and sheep. Statistical analysis revealed same trend of results as for right humerus among both species.

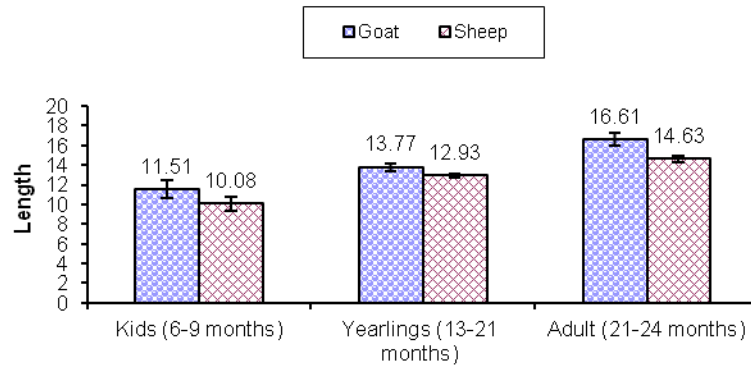


Figure 3. Mean \pm SEM of length (cm) of right humerus of different age groups of Bari goat and Dumbi sheep.

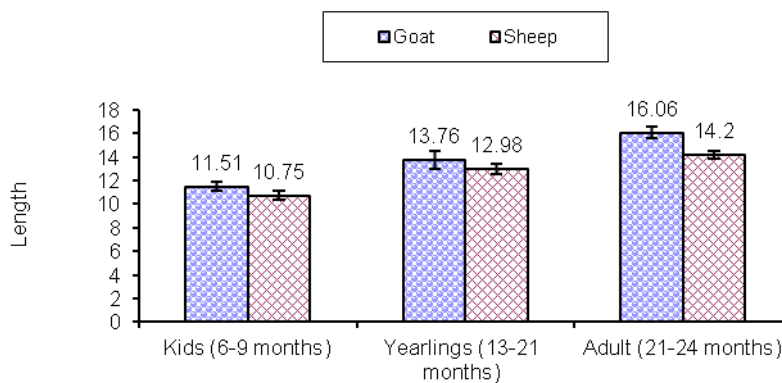


Figure 4. Mean \pm SEM of length (cm) of left humerus of different age groups of Bari goat and Dumbi sheep.

Comparative differences in humerus

Like other ruminants, the humerus of goat and sheep also possesses one shaft and two extremities (proximal and distal). The shaft is twisted cylindrical and presents four surfaces and makes “S” shape in goat and highly curved “S” shape in sheep. Head is small and rounded; fossa in front of head is deep and prominent in goat, whereas, the head is large with shallow fossa in case of sheep. Tricepetal line is more prominent in sheep but less so in goat. Deltoid tuberosity is less prominent and smooth in goat but more prominent and rough in sheep. The distal epiphysis is thin in Bari goat but thick in Dumbi Sheep (Plate 2)

The radial and olecranon fossae of the humerus of Bari goat are shallow, but deep in Dumbi sheep. At lateral aspect pit of lateral condyle is deep but the cavity of lateral condyle is broad and shallow (Plate 3). The epicondyloid crest of humerus is quite prominent in goat, but inconsistent in sheep (Plate 3).

DISCUSSION

The values of absolute weight, breadth of proximal end,

breadth of distal end, circumference and length of right and left humerus of both goat and sheep have been presented in the Figures 1 to 3 and Table 1. While comparing humerus at different variables revealed that the bones of Dumbi sheep are heavier, broader but shorter than those of Bari goat. Okpe and Adamu (2002) indicated that the bones of the Yankassa sheep were heavier and longer, with greater diameter than those of the Red Sokoto goat of the same age. Although the differences he found were not statistically significant ($p > 0.05$). The humerus of adult Black Bengal goat was found to be 12.06 ± 0.27 cm in length. The diameter of shaft at the level of nutrient foramen was 4.24 ± 0.05 cm. The breadth of humerus was 1.66 ± 0.06 cm. The deltoid tuberosity was less prominent and there was shallow radial and olecranon fossa (Siddiqui et al., 2008). Whereas, Hassan et al. (2007) measured the length (16.12 ± 0.41), breadth of the proximal end (4.41 ± 0.17), breadth of the distal end (3.49 ± 0.21) and breadth of diaphysis (1.77 ± 0.09) of humerus in adult female Morkaraman sheep, a local Turkish breed. Findings of present study are in agreement with Okpe and Adamu (2002) but partial agreement with those of Siddiqui et al.

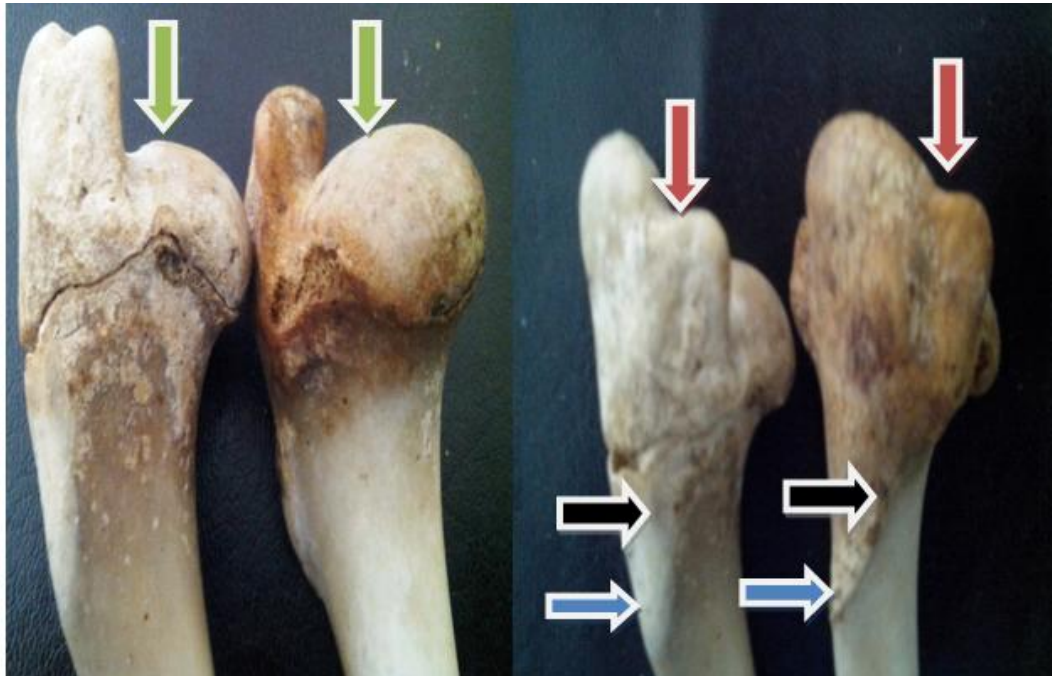


Plate 2. Comparative differences in head (Green arrows), inter tubercle groove (brown arrows), neck (B), deltoid tuberosity (Blue arrows) and tricepital line (Black arrows).

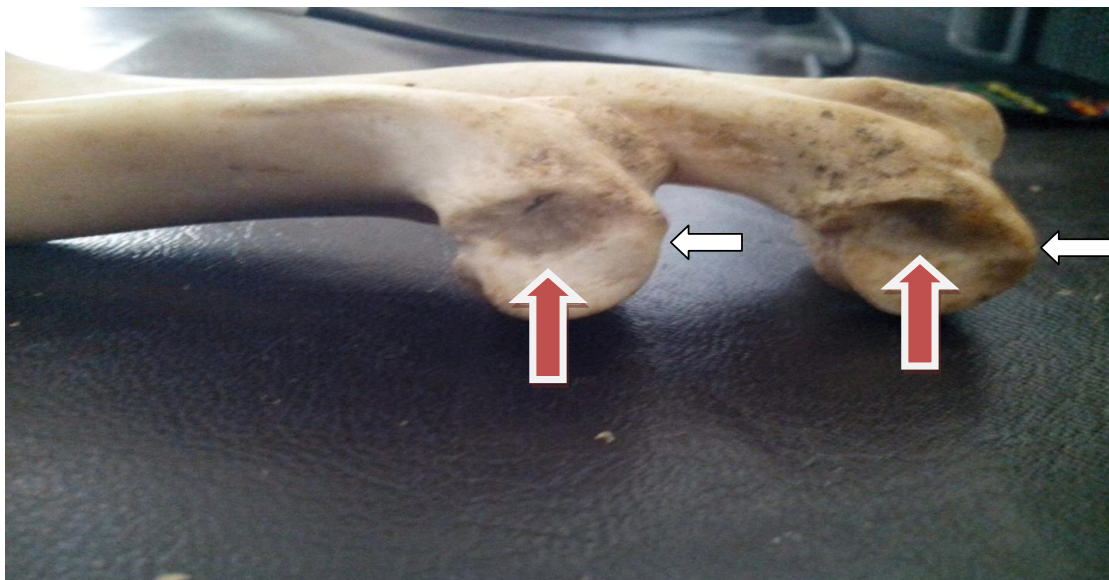


Plate 3. Shows the comparative differences in lateral aspect pit of lateral condyle (Brown arrows) and epicondyloid crest (White arrows).

(2008) and Hassan et al. (2007). The variation could be attributed to breed difference.

CONCLUSIONS AND SUGGESTIONS

On the basis of these findings and osteometric

differences in humerus of both goat and sheep it is quite apparent to explanation that: The humerus of Dumbi sheep observed to be massive in terms of weight, circumference and breadth of proximal and distal ends than that of Bari goat, when compared among three different age periods. Comparative analysis revealed major differences in the morphology of humerus bones

that could be used as a breakthrough in identification of a particular species.

The sturdy suggests:

1. Further studies are suggested to study other age groups like lambs below 06 months and old age group (Above 36-months) in Dumbi sheep and Bari goat.
2. These studies are also suggested in large breeds like Kamori, Beetal etc.
3. Comparative study of the long bones of hind limb so that a clear depiction of gross anatomical and morphometric studies of these bones can be observed.

Conflict of Interests

The author(s) have not declared any conflict of interests.

REFERENCES

- Anonymous (2003-04). Pakistan Livestock Economic Survey 2003-04. Agricultural Census Organization, Statistics Division, Government of Pakistan, Lahore.
- Anonymous (2010-11). Pakistan Livestock Economic Survey 2010-11. Statistics Division, Government of Pakistan, Lahore.
- Anonymous (2011-12). Pakistan Livestock Economic Survey 2010-11. Statistics Division, Government of Pakistan, Lahore.
- Guintard C, Lallemand M (2003). Osteometric study of metapodial bones in sheep (*Ovis aries*). *Ann. Anat.* 185:573-583. [http://dx.doi.org/10.1016/S0940-9602\(03\)80131-0](http://dx.doi.org/10.1016/S0940-9602(03)80131-0)
- Hassan A, Onar V, Mutus R (2007). The relationship between morphometric and long bone measurements of the Morkaraman sheep. *Turk. J. Vet. Anim. Sci.* 33(3):199-207.
- Isani GB, Baloch MN (1996). *Sheep and Goat Breeds of Pakistan*. Press Corporation of Pakistan, Karachi, pp. 1-95.
- Khan MF, Ashfaq F (2012). Dairy Goat in Pakistan: Potential, Opportunities and Challenges. Proceedings of the 1st Asia Dairy Goat Conference, Kuala Lumpur, Malaysia, 9–12 April 2012.
- Khan MS, Khan MA, Mahmood S (2008). Genetic resources and diversity in Pakistani goat. *Int. J. Agric. Biol.* 10(2):227-231. <http://dx.doi.org/10.1017/S1479262108994132>
- Makkaway NH, EL-Mezian A, Tawab MA (1988). A radiological appearance of prenatal ossification centers and epiphyseal lines of the thoracic limb in Egyptian buffaloes. *Zag Vet. J.* 16(4):310-322.
- Mohammad PW (2007). Trends and growth in livestock population in Sindh: A comparison of different censuses. *Ind. J. Manage. Soc. Sci.* 1(1):53-69.
- Oishi A, Yamada S, Sakamota H, Kamlya S, Yanagida K, Kubota C, Watanabe Y, Shimizu R (1996). Radiographical evaluation of bone maturation in Japanese black beef cattle. *J. Vet. Med. Sci.* 58:529-535. <http://dx.doi.org/10.1292/jvms.58.529>; PMID:8811621
- Okpe GC, Adamu SS (2002). Comparative anatomy of long bones of the appendicular skeleton of Yankassa sheep and Red Sokoto goat in Zaria Metropolis. *Global J. Agric. Sci.* 1(1):7-10.
- Outram A, Conwy PR (1998). Meat and marrow utility indices for horse. *J. Archaeol. Sci.* 25:839-849. <http://dx.doi.org/10.1006/jasc.1997.0229>
- Schewers JL, Musgrave JH, Evans SP (1980). The estimation of late fetal and prenatal age from limb bone length by linear and logarithmic regression. *Ann. Hum. Biol.* 7(3):257-266. <http://dx.doi.org/10.1080/03014468000004301>
- Shah SI, Bashir E, Bantel R, Khan BB, Isani GB (2001). *Animal Husbandry*. National Book Foundation Islamabad. p. 73.
- Siddiqui MSI, Khan MZI, Moonmoon S, Islam MN, Jahan MR (2008). Macro-anatomy of the bones of the forelimb of black Bengal goat (*Capra hircus*) *Bangl. J. Vet. Med.* 6(1):59-66. <http://dx.doi.org/10.3329/bjvm.v6i1.1340>
- Tariq MM, Bajwa MA, Babar S, Waheed A, Bukhari FA, Hameed T, Marghazani IB, Javed Y (2011). Effect of non-genetic and genetic factors on birth weight of Mengali sheep of Balochistan. *Can J. Appl. Sci.* 1(3):121-128.
- Vatta AF, Abbot MA, Villiers JF, Gumede SA, Harrison LJS, Krecek RC, Letty BA, Mapeyi N, Pearson RA (2006). *Goat keepers' animal health care manual*. Agricultural Research Council. Onderstepoort Veterinary Institute with Kwazulu-Natal Department of Agriculture and Environment, South Africa, 60 pp.

Full Length Research Paper

Capacity enhancement of multicarrier code division multiple access (MCCDMA) using orthogonal complete complementary codes and adaptive constellations

G. Senthilkumar^{1*} and R. Amutha²

¹Department of Electronics and Communication Engineering, Sri Chandrasekharendra Saraswathi Viswa Mahavidyalaya University, Kanchipuram, India.

²Department of Electronics and Communication Engineering, SSN College of Engineering, Chennai, India.

Received 28 November, 2013; Accepted 28 February, 2014

The multicarrier code division multiple access (MCCDMA) is a strong candidate for the future wireless mobile communication systems put forth by service quality and system capacity. In order to exploit the maximum possible channel diversity and desirable correlation properties, the modification of MCCDMA system is addressed here to pave the way to remove the multiple access interference (MAI) effect and to increase the spectral efficiency (SE) due to the possible integration of space-time block coding (STBC) and multi input multi output (MIMO) techniques with two-dimensional orthogonal complete complementary (OCC) codes. The impact on modifications in the MCCDMA system is studied. Due to frequency selective fading and multipath effects, MCCDMA suffers from MAI due to loss of orthogonality among the users. In this paper, the constellation movement scheme is proposed to break the interference limitation in order to increase the SE and system capacity. In this scheme, the constellation of one of the users is moved adaptively relative to the other by an optimal angle based on quantized estimation to counteract MAI, caused by multipath effects without varying the transmit power in order to satisfy minimum distance threshold at the detectors. The simulation result shows that this modified MCCDMA system and proposed constellation movement scheme achieves significant performance improvement in terms of bit error rate (BER) and SE compared to conventional MCCDMA systems using unitary spreading codes. It also shows that the proposed scheme combats MAI against frequency selective fading and multipath effects and achieves a significant improvement in user capacity as the number of users increased.

Key words: Multicarrier code division multiple access (MCCDMA), multiple access interference (MAI), orthogonal complete complementary (OCC) codes, channel states, adaptive constellations.

INTRODUCTION

With the ever increasing demands on bandwidth efficiency and system capacity, the multicarrier code

division multiple access (MCCDMA) has become strong technology for the current and next generation (5G)

*Corresponding author. E-mail: gskkanchi@gmail.com. Tel: +919994288266.

Author(s) agree that this article remain permanently open access under the terms of the [Creative Commons Attribution License 4.0 International License](http://creativecommons.org/licenses/by/4.0/)

wideband cellular mobile wireless communication systems where multimedia applications and flexible and high data rate services are standard. Among its many advantages, it is worth mentioning the high spectral efficiency (SE) deriving from the performance of orthogonal frequency division multiplexing (OFDM) in a Rayleigh fading environment (Varzakas, 2007) and the capability of collecting the received signal energy scattered in the frequency domain, which results into a remarkable frequency diversity gain (Hara and Prasad, 1999) to mitigate fading effect. In a MCCDMA system, the user's data are spread in the frequency domain using orthogonal spreading codes (Fazel and Kaiser, 2008).

After passing through a frequency selective channel, however, the received codes are no longer orthogonal due to non-ideal correlation properties of spreading codes and multiple access interference (MAI) will arise. Interference mitigation is traditionally accomplished at the receiver side by resorting to well-known multiuser detection schemes (Verdu, 1998). Due to heavy processing load as number of users' increases, these schemes may be unfamiliar. The problem of optimum Multiuser Detection (MUD) with less complexity in CDMA communication systems was considered in Abdulhamid and Hamidreza (2013) based on sign detector and longer code lengths. This improves the processing gain but there is no effect on system capacity. The code scheme based on the complementary code was proposed in Chen et al. (2006) to design a MAI-free CDMA system in a flat fading channel. These codes are derived from the sets of auto complementary codes, any two of which are cross complementary codes (Li and Huang, 2009). This can be constructed by using a \sqrt{N} -dimensional orthogonal matrix. Though this scheme achieves optimum spectrum efficiency using offset stacked spreading modulation than conventional CDMA system, the number of user supported is less. Interference suppression against MAI effect with respect to the number of users is achieved by inter-group complementary (IGC) codes (Jing et al., 2008). This increases complexity of the implementation due to user groupings. As an effective method to increase the diversity gain and combat the effects of fading, transmit diversity has been studied extensively in the past. The space-time block coding (STBC) (Alamouti, 1998) provides full diversity gain as well as full rate and does not sacrifice bandwidth efficiency. Space-time (S-T)-coding based multi input multi output (MIMO) systems (El-Hajjar and Lajos, 2010) have emerged as an extremely important enabling technology for 4G wireless to offer substantially improved detection efficiency and system throughput by exploiting its unique spatial diversity gain and spatial multiplexing capability without consuming extra spectrum. In order to exploit the maximum possible channel diversity and desirable correlation properties, the advantages offered by STBC and MIMO schemes are utilized in this paper for the modification of MCCDMA system employing two-dimensional orthogonal complete

complementary (OCC) codes to remove the MAI effect and to increase the SE. The development issues are addressed here. The impact on the performance of this modified MCCDMA system is studied in terms of bit error rate (BER) and SE for further improvement.

From the above study, this modified MCCDMA system fails to remove MAI completely in a multipath environment. It is observed that the overlapping of received symbols results at particular channel conditions due to the fact that received signals from multipath add destructively causing multi-user interference which results in high error rates. With increasing MAI, the transmission quality for all users worsens and the number of subscribers able to be facilitated (user capacity) is limited by a specified BER threshold. To overcome such propagation effects, channel estimation and compensation applied for it to reduce BER as the channel parameters varies randomly (Mario et al., 2007). Adaptive loading algorithms for OFDM system with imperfect channel state information (CSI) were proposed in Ye et al. (2006). The network coding approach was used to mitigate these random constellations for two way relay networks (Koike-Akino et al., 2009). In this approach, the performance of end to end throughput was achieved but requires complex optimization procedure. In Musavian et al. (2011), variable rate and the constellation size were adapted according to the channel conditions for reducing the error rates. Adaptive modulation scheme was proposed, which vary various transmission parameters based on different modulation schemes according to existing channel conditions to minimize the error rates (Kugalur and Veerappa, 2013). All these schemes failed to recover the faded overlapped symbols due to MAI caused by multipath effects at poor channel conditions and also it require complex perfect CSI at the transmitter. The perfect CSI at the transmitter is not easily feasible, as it would require additional processing for feedback. These factors severely limit the performance of the system. To solve these discussed problems, the MCCDMA system is modified in the architecture and effective constellation movement scheme is proposed.

The contributions of this paper are as follows:

- 1) Modification of MCCDMA system is presented which exploits the diversity gain and ideal correlation properties for mitigating MAI in order to increase the user capacity while considering the development issues on integration of MIMO and STBC in two-dimensional to support the group of OCC codes (in system model section).
- 2) The constellation movement scheme is proposed for the users which move the angle of constellation of one of the users adaptively with respect to the other based on simple quantized estimation in order to satisfy minimum distance threshold at the detectors.
- 3) Procedure for simple quantized estimation alternate to complex estimation of perfect CSI is developed. The procedure is illustrated for obtaining the quantized details

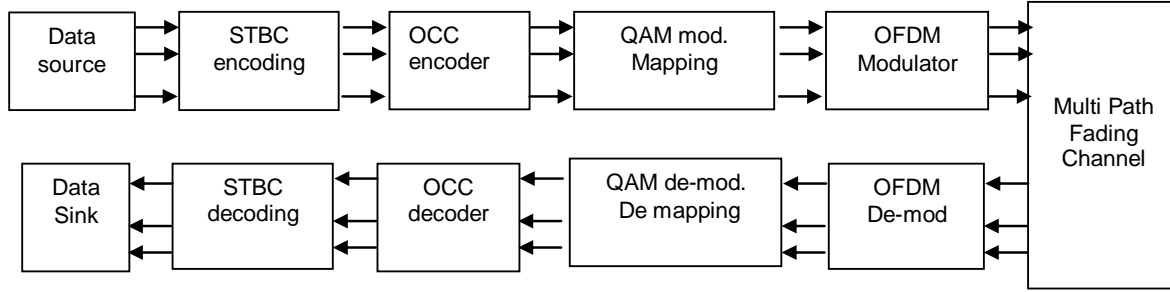


Figure 1. Simplified transceiver structure of MCCDMA system model.

of channel states to recover faded symbols.

- 4) The procedure to compute the optimal angle for movement is explained for the M-QAM signal set.
- 5) The threshold of minimum distance and condition to avoid overlapping are developed.
- 6) The modified MCCDMA system and proposed constellation movement scheme are evaluated for the performance improvement in terms of BER and SE
- 7) Simulation results are discussed to demonstrate the capability of the modified MCCDMA and proposed scheme to outperform the conventional MCCDMA system with unitary spreading codes.

METHODOLOGY

System model

Figure 1 illustrates a simplified transceiver structure of modified MCCDMA system model. The modification of MCCDMA system is addressed here in addition to the system description to counteract the loss of orthogonality in frequency selective fading and multipath environment for increasing the interference mitigation efficiency. Modification exploits ideal correlation properties of spreading code, the diversity gain and chip based modulation to minimize the correlation among the users, reduce the error rate and increase the SE, respectively.

Orthogonal complete complementary (OCC) codes

For minimum correlation among the users, the OCC code is employed based on ideal correlation properties which spread user data in time and frequency domains. The OCC codes are kind of ideal orthogonal code and defined by three parameters, set size (K), flock size (M) and element code length (N). The processing gain of OCC code is $N.M=N\sqrt{N}$ since each symbol bit will be spread by the whole set of CC code sequences instead of a single sequence. The system robustness against the adverse effects of the channel and the division among users depends on the orthogonality of the spreading codes. The orthogonality of this code is based on its correlation functions. The auto correlation function (ACF) of the OCC codes is zero for any shifts except zero shift which help to remove the delayed version of received signals due to multipath propagation and its cross correlation function (CCF) is zero for any possible number of shifts which allow the receiver to remove undesired other user's signals. The correlation function of the OCC code is based on a group of element codes jointly. This

implies that each user should use group of M element codes as its spreading code instead of a single code.

STBC encoding

For diversity gain, STBC encoding integrates STBC in two-dimensional with OCC encoding with M subcarriers modulation using OFDM architecture. The signal spectrum is modulated by an OCC code set, which is unique for each user. The flock of M element codes, $\{c_{k,1}, c_{k,2}, \dots, c_{k,M}\}$ are allocated to K users. Each element code $c_{k,m}$ consists of N chips where $k \in (1, K)$ and $m \in (1, M)$. The information symbols which are typically coming from the outputs of data source are first space-time block-encoded into P parallel independent symbol streams. Based on the Alamouti STBC algorithm, an encoded signal block for the m^{th} element code of the k^{th} user in this MCCDMA system can be written as:

$$S_{1,k,m} = (b_{1,o} c_{o,k,m} + b_{1,e} c_{e,k,m}), \quad (1)$$

$$S_{2,k,m} = (b_{1,e} c_{o,k,m} - b_{1,o} c_{e,k,m}), \quad (2)$$

The P parallel symbol streams are fed into OCC encoding module that consists of M OCC encoding branches, each of which has P OCC slices. There are in total up to M replicas of P parallel symbol streams encoded by different OCC code sets to implement diversity order of P and parallel transmission order of M . Therefore, the family size of the OCC must be at least MP .

OCC encoding

For SE, OCC encoding configures chip based spreading modulation and QAM modulation based on group of OCC codes. This MCCDMA combines its OCC spread-coded bits together using chip based spreading modulator. This modulator improves the SE which is defined in unit of bit(s) per chip to measure the bandwidth efficiency. The spreading modulator used by every user in which the input data stream is from the k^{th} user, $b_k = (b_{k,1}, b_{k,2}, \dots, b_{k,j}, \dots)$. The input bit sequence of each user is spread with the corresponding element code, $c_{km} = (c_{1km}, c_{2km}, \dots, c_{Nkm})$. Also, each information bit is shifted by one chip relative to one another and then added. The OCC encoding output from user k is expressed as:

$$d_{k,m}(t) = \sum_{i=0}^{\infty} \cdot \sum_{n=0}^{N-1} b_{K,i} c_{m,n} \Pi_{T_c} \left(\frac{(t-(i+n+\frac{1}{2})T_c)}{T_c} \right) \times \Pi_{\frac{T}{T}} \left(\frac{(t-(\frac{T}{2})-iT_c)}{T} \right), \quad (3)$$

Where

$$\Pi\left(\frac{t}{T\omega}\right) = \begin{cases} 1, & t \in \left(-\frac{T\omega}{2}, \frac{T\omega}{2}\right), \\ 0, & \text{otherwise} \end{cases} \quad (4)$$

where $d_{K,m}(t)$ represents the m^{th} OCC encoding output from user K , $b_{K,i}$ denotes the i^{th} information bit from user K , $C_{m,n}$ denotes the n^{th} chip of the m^{th} element code and T_c and T denote chip and bit duration, respectively. Then, each element code, c_{km} is carrier modulated with sub-carrier, fm . Thus, in effect, the user data information has been spread in both the time and frequency domains. The time domain spreading is carried out by each individual element code, while the frequency spreading is fulfilled across different sub-carriers in different carrier frequencies. The two-dimensional spreading offers much more degrees of freedom to achieve orthogonality of the spreading codes in both the time and frequency domains.

To maintain good performance in the presence of fading, for the element code length of 'N' of the OCC code the chip based spreading modulator is followed by a QAM map to transmit the $L=(N-1)$ different levels in symbol duration for its robustness in detection efficiency. In the case of the downlink, the m^{th} OCC encoding output is the sum of all OCC spread streams from all the users associated with the m^{th} element code of each code family; for example, $A_0, B_0, C_0,$ and D_0 belong to family 0. It is expressed as:

$$s_m(t) = \sum_{k=0}^{M-1} d_{K,m}(t), \quad (5)$$

Where M denotes the flock size, $K=M=\sqrt{N}$.

To maintain good performance in the presence of frequency selective fading and hardware architecture simplification, the transmitter is implemented using OFDM architecture. Each transmitter will use M different subcarriers to transmit M element codes and the whole MCCDMA system will share the same M sub-carriers. The sub-carriers carry the same data information but encoded by different element codes belonging to the same code flock. It is assumed to use only two antennas ($n_t = P = 2$) to achieve transmitter diversity. It is also assumed that signals from different antennas in a transmitter experience independent Rayleigh fading and additive white Gaussian noise (AWGN).

At a receiver, the received symbol streams go to maximum ratio combining (MRC) from M replicas to extract P parallel symbol streams. The combining of outputs from the M chip matched-filters using MRC improves the frequency diversity gain. Also, the correlation properties of element sequences along with MRC scheme achieve a MAI-free performance (Wei et al., 2013). The carrier demodulation should be carried out first, and then the correlation takes place between local sub-codes and the incoming signals in the M sub-channels, and is given by:

$$\text{Cor}_K(t) = \sum_{m=0}^M r_K(t) * C_{K,m}, \quad (6)$$

Where $r_K(t) * C_{K,m}$ is the correlation between the received signal of user K and element code m of the flock assigned to user K . The M correlation outputs are then added together to obtain the decision variable. The receiver performs coherent decoding with perfect or estimated CSI. Then,

$$b_{K,i}(t) = \text{sgn}(\text{cor}_K(t)), \quad (7)$$

Where $b_{K,i}(t)$ denotes the i^{th} demodulated information bit of user K and $\text{sgn}(\cdot)$ denotes signum function.

Proposed constellation movement scheme

The overlapped symbols results at particular channel conditions due to the fact that received signals from multi-paths add destructively causing multi-user interference. This results in high error rates, worst transmission quality for all users and the number of subscribers able to be facilitated (user capacity) is limited. The constellation movement scheme is proposed to break the multi-user interference limitation in order to improve the performance in terms of SE and system capacity. In this scheme, the constellation angle is adaptively controlled by moving the constellation of one of the users relative to the other with an optimal angle based on simple quantized estimation so that the distance between the symbols can be increased above the minimum distance threshold at the detectors without varying the transmit power. This will increase the interference mitigation efficiency against multipath effects.

It is assumed that destination knows details of channel gains, h_k for the users- k separately. The channel amplitude ratio, $\gamma = \left| \frac{h_B}{h_A} \right|$ and phase difference $\theta = \frac{\angle h_B}{\angle h_A}$, are calculated. The pair (γ, θ) is used to represent the channel state, $\gamma e^{j\theta}$ in the complex plane (Γ, Φ) . The received symbols are represented collectively as additive constellation, $S_{\text{ADD}}(h_A, h_B) = \sqrt{P_A} h_A S_{\text{grp}}(\gamma, \theta)$ where $S_{\text{grp}}(\gamma, \theta)$ is group constellation, $(S_A + \gamma e^{j\theta} S_B)$.

Minimum distance threshold

The minimum squared Euclidean distance between the transmitted data $(S_A, S_B)_{\text{ADD}}$ and its candidate $(S'_A, S'_B)_{\text{ADD}}$ is measured as performance metric at the destination. The normalized squared distance can be written as:

$$d^2_{(S_A, S_B) \leftrightarrow (S'_A, S'_B)} = \left| (S_A - S'_A) + \gamma e^{j\theta} (S_B - S'_B) \right|^2, \quad (8)$$

At particular channel conditions, the squared Euclidean distance $d^2_{(S_A, S_B) \leftrightarrow (S'_A, S'_B)}$ goes to zero whenever,

$$\gamma e^{j\theta} = -\frac{(S_A - S'_A)}{(S_B - S'_B)} \quad (9)$$

That is, the two received symbols are overlapped due to MAI caused by multipath effects. These values of γ and θ are called singular channel fade state at which the minimum distance, d_{min} is zero or very low, resulting in poor error performance at the destination. Thus, it is necessary to fix the threshold of minimum distance, δ to reduce the error rate such that any channel states (γ, θ) lying close to any singular channel states should be controlled so that $d_{\text{min}} > \delta$. This requires identification of channel fade states which reduce minimum distance below distance threshold and avoiding this using adaptive control of constellation angle of one of the users relative to the other based on channel quantized estimation and adaptive control of constellation angle.

Procedure for quantized estimation

The proposed idea of the quantized estimation is to collect the quantized details of channel states using channel distance mapping with respect to the singular channel states, indicate the details of channel states which reduce minimum distance to the users.

The set of singular channel states (γ_i, θ_i) are obtained for the QAM signal set in the plane for $\gamma \geq 1$ and $\theta \in [0, \pi/M]$ where $1 \leq i \leq$

N_S and the number of singular channel state, $N_S = \frac{M^2}{8} - \frac{M}{4} + 1$. The channel states are mapped into distance d_{ci} using the distance functions which gives the value of the distance between the transmitted data $(S_A, S_B)_{ADD}$ and its candidate $(S'_A, S'_B)_{ADD}$ for the channel states. The same distance pair of elements are collectively called as distance class, $d_c(\gamma, \theta)$ and corresponding region in complex plane is C . For each singular channel states (γ_i, θ_i) , the distance set of minimum class distance functions $d_{C_{imin}}(\gamma, \theta)$ are obtained among the sets of class distance functions, $d_{C_{ij}}(\gamma, \theta)$, $1 \leq i \leq N_S$, $1 \leq j \leq J$ which gives zero value of the distance between the two additive constellation points. The minimum distance threshold $d_{min}(S)$ is also obtained. The partitions $P_S(C_i)$ corresponding to $d_{C_{imin}}(\gamma, \theta)$ are found by equating the curves $d^2_{C_i} = d^2_{C'_i}$, $1 \leq i \neq j \leq N_S$ and $d^2_{C_i} = d^2_{min}(S)$. The partition exterior to all these partitions, is denoted as $P_S(C_{dmin})$ lying within the space $[0, \pi/M]$. In this way, the channel states are mapped into partitions. It is thus required to identify the channel states (γ, θ) which lies inside the partitions, centered at the singular channel state (γ_i, θ_i) and radius $\delta/|s_{2,i} - s'_{2,i}|$ where the distance function values, $d_{C_i}(\gamma, \theta)$ below threshold, that is,

$$|\gamma e^{j\theta} - \gamma_i e^{j\theta_i}| < \frac{\delta}{|(S_{B,i} - S'_{B,i})|}, \quad (10)$$

These partitions are called as disturbance circles because the minimum distance requirement of $S_{grp}(\gamma, \theta)$ is disturbed. Therefore, the minimum distance, d_{min} should be maximized above minimum distance threshold, δ in order to increase the interference mitigation efficiency.

Next, the position of the channel states is indicated to the users whether inside/outside the disturbance circles. This needs a feedback of $|\log_2(N_S + 1)| = 5$ bits for 16QAM in this scheme such that the incurred overhead is minimum compared to feedback required for perfect CSI at transmitter in other systems.

Adaptive control of constellation angle

The proposed idea is to move the constellation of user- j adaptively by an optimal angle β relative to the adjacent user without changing the transmit power if the channel state (γ, θ) lies inside any of the disturbance circles in order to meet the minimum distance threshold and no constellation movement is required for channel states outside the disturbance circles.

In order to obtain the optimal angle of movement $\beta_{i,opt}$ for channel state lies inside the disturbance circle, it is required to compute the value of optimal phase $\theta = \theta_{i,opt}$, $\theta \in [0, \pi/M]$ which maximizes the minimum distance and transforms channel state from θ to $\theta + \beta$ lies outside the disturbance circles after movement. During the movement of constellation phase away from θ_i but with fixed radius, γ_i , the phase and minimum distance are computed at the points of intersection of the arc $\gamma = \gamma_i$ and the boundaries between the partitions surrounding other singular channel states. Among all the above points, the maximum of minimum distance is selected for the channel state corresponding to that point of intersection $(\gamma_i, \theta_{intersect})$. The optimal phase $\theta_{i,opt} = \theta_{intersect}$. Then, the optimal angle of movement $\beta_{i,opt}$ for the constellation of user-A relative to user-B is calculated based on optimal phase $\theta_{i,opt}$ as:

If $\theta_i = \pi/M$, then, $\beta_{i,opt} = \pi/M - \theta_{i,opt}$ in a clockwise direction.
If $\theta_i = 0$, then, $\beta_{i,opt} = \theta_{i,opt}$ in an anticlockwise direction.

Thus after movement, the disturbance circle is called as the changed circle since its center at (γ_i, θ_i) is changed to $(\gamma_i, \theta_{i,opt})$.

In order to avoid the overlap during the movement of angle of

constellation with other states, it is necessary that the distance between the center of each of the changed circle $(\gamma_i, \theta_{i,opt})$, $1 \leq i \leq N_S$ and other singular channel states (γ_j, θ_j) , $1 \leq j \leq N_S$ should be at least equal to the sum of the radius of the changed circle and the radius of the disturbance circles centered at (γ_j, θ_j) . This can be written as:

$$r(\gamma_i, \theta_i) + r(\gamma_j, \theta_j) \leq d_{(\gamma_i, \theta_{i,opt}) \leftrightarrow (\gamma_j, \theta_j)}, \forall 1 \leq j \leq N_S \quad (11)$$

Thus, the proposed constellation movement scheme mitigates the MAI effect through adaptive control of constellation angle by keeping the squared Euclidean distance between the transmitted data and its received candidate above minimum distance threshold. The quantized estimation reduces the complexity by considering only the quantized details of channel states and send to the user for controlling the constellation angle.

RESULTS AND DISCUSSION

Based on the discussion given in the earlier sections, the performance of this modified MCCDMA systems and proposed constellation movement scheme are evaluated in terms of BER and SE using MATLAB against signal to noise-ratio (SNR) with different spreading codes such as Walsh, Gold and OCC codes. In the simulations, downlink frequency selective Rayleigh fading channel with AWGN floor and multipath environments are considered. It is assumed that the path components are different and independent for all paths. The receiver had perfect knowledge of the CSI. The Gold and Walsh codes are taken as examples for traditional quasi-orthogonal codes and typical orthogonal codes, respectively. The data packet of 256 symbols, the symbol length of 64, the modulation of 16-QAM, the number of subcarriers of 128 and the following key parameters of those spreading codes used in the simulations are:

- 1) OCC: flock size (M) = 4, element code length (G) = 16, Sequence length $N = 64$,
- 2) Walsh code: sequence length $G = N = 64$
- 3) Gold code: sequence length $G = N = 63$

Figure 2 shows the BER curves simulated against SNR among the MCCDMA system with different spreading codes for increased number of users ($K = 16$) under a two-ray multipath channel with its delay profile being $[1/2, 0, 1/2]$ and one chip inter path delay. The BER curves for the unitary spreading codes (Walsh and Gold codes) deteriorate obviously because of loss of orthogonality due to increased MAI in frequency selective fading, while OCC code performs nearly the same as that in the single user scenario. Hence, the orthogonality of the spectral modulated signal using OCC code is retained. Thus, the user capacity increases due to this increased interference mitigation efficiency.

The higher processing gain can be possible when element code length increases but it does not increase

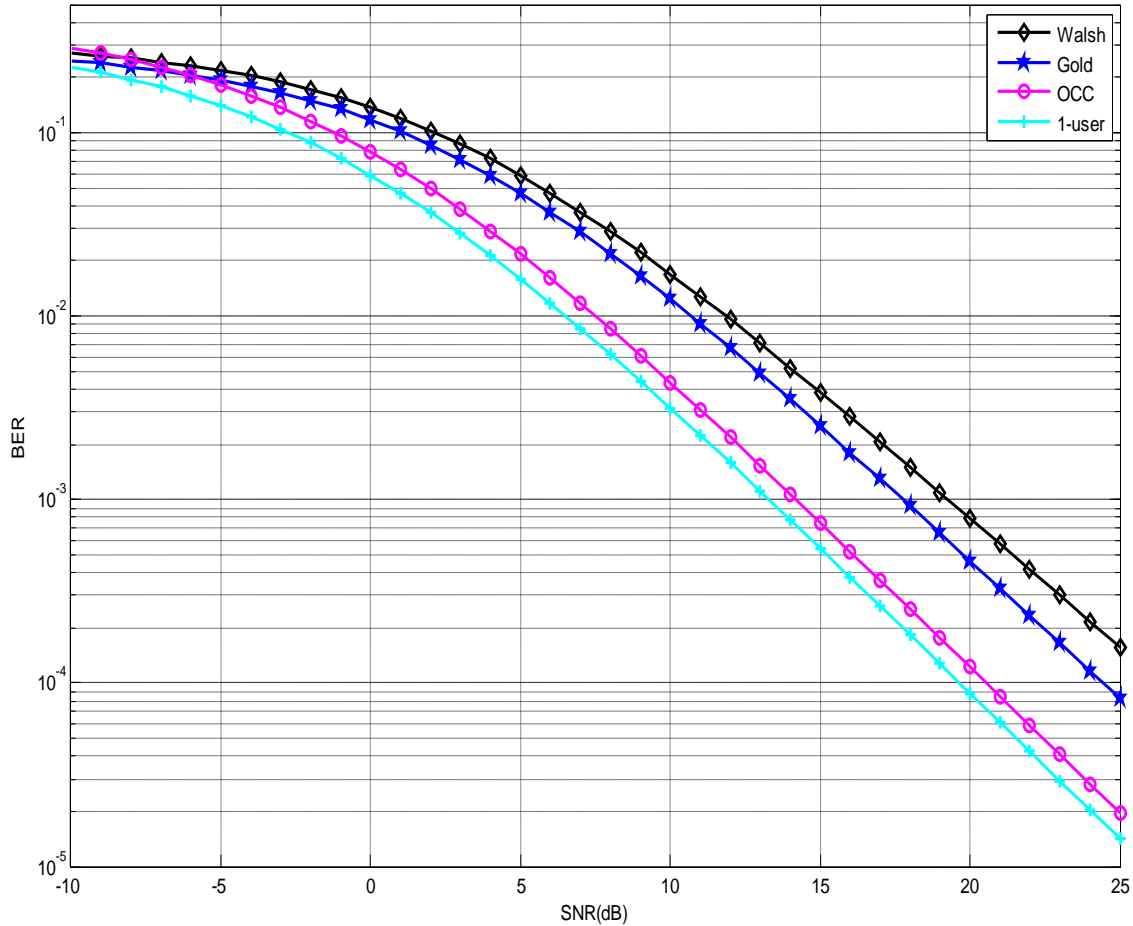


Figure 2. BER comparison for the increased number of users (16) among MCCDMA system with different spreading codes.

the system capacity. The user capacity and frequency diversity can be increased further when the flock size of OCC code and corresponding number of subcarriers increases but complexity of the system grows. So, it is one design issue.

It was assumed that perfect channel knowledge is available at the coherent Rake receiver using pilot-based channel estimation. However, the time varying conditions in the mobile communication channels limits the performance and system capacity. The channel conditions should be estimated and compensated using equalization methods based on the fading statistics for minimizing the error rates. This equalization method for multiple carriers and multiple antennas in multiuser application is difficult and computationally intensive to estimate the amplitude and phase shift caused by the multipath propagation effects. As the number of users' increases, the performance is degraded due to the non-ideal channel estimation results and increased multiuser interference. The complex estimation is demanded. This increases computational complexity in the order of $O(2^K)$ with K users.

BER performance is compared for MAI robustness among the MCCDMA system using Walsh and OCC codes with and without constellation movement in Figure 3 for increased number of users ($K = 16$). The BER curves for the Walsh codes deteriorate obviously due to increased MAI, whereas the system with OCC code outperforms that with Walsh codes due to good correlation among the users provided by OCC codes and diversity gain. It is observed that the performance gain of SNR of 3 dB is achieved using constellation movement scheme compared to that without this scheme. It shows that the detrimental effects of MAI are reduced by keeping the squared Euclidean distance between the transmitted data and its received candidate above minimum distance threshold. This increases the interference mitigation efficiency against random constellations caused by multipath effects so that the receiver can decode the messages very easily from the received symbols. The results reveal that the minimum distance threshold ensures large channel amplitude ratio $\{\gamma = \frac{|h_B|}{|h_A|}\}$. This results in more reliable communications;

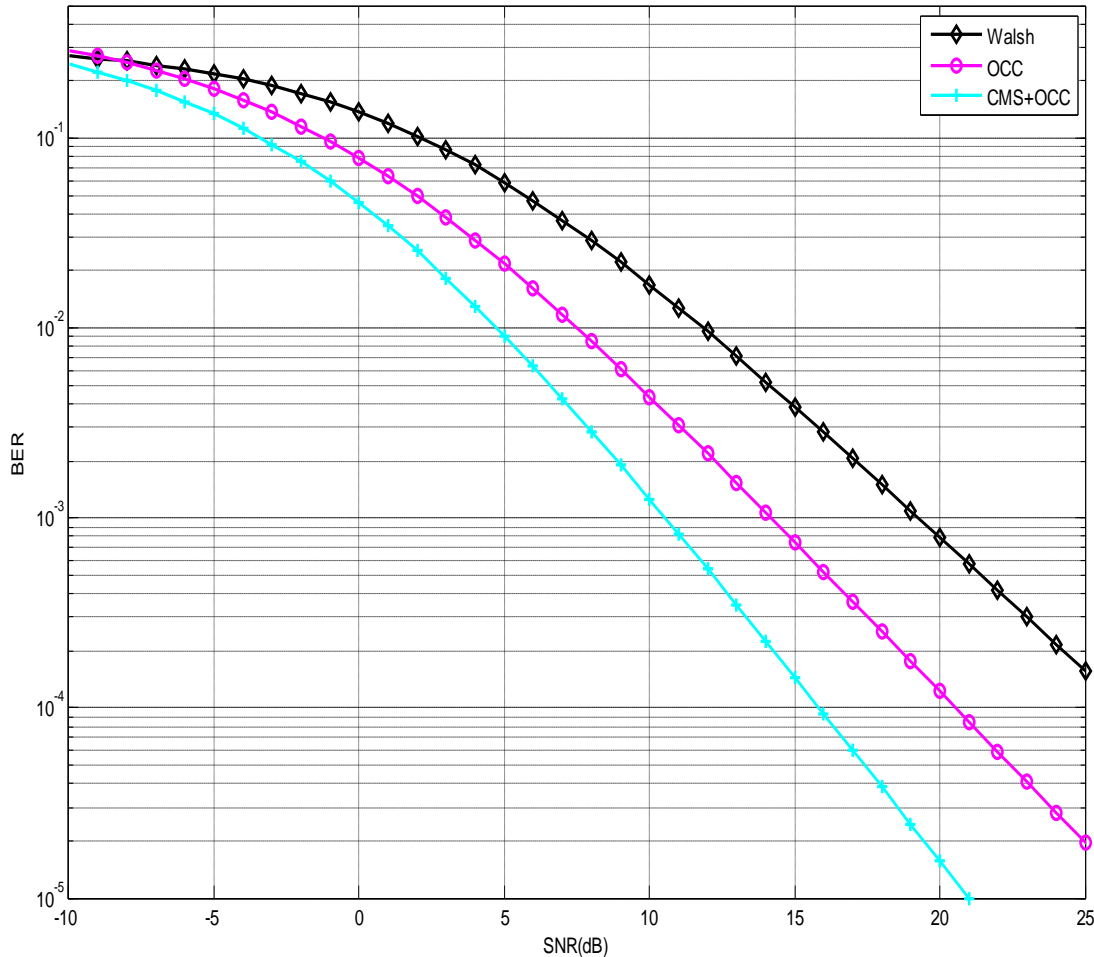


Figure 3. BER comparison for MAI robustness against SNR among MCCDMA system using Walsh and OCC codes with and without constellation movement scheme.

In order to solve the channel estimation issues and reduce the computational complexity based on the above discussion, the simple quantized modified estimation design strategy based on the minimum distance criterion is implemented in the proposed constellation movement scheme. This simple estimation and constellation movement scheme can provide much robustness to amplitude and phase shifts caused by difficult multipath effects.

Another significant dividend of quantized estimation method is that it limits the amount of required channel information at the users so that associated overhead is nominal compared to perfect CSI requirement.

The feedback of $|\log_2(N_s + 1)| = 5$ bits for 16QAM signal set is required as channel estimation load in this simplified quantized estimation procedure. When comparing with the perfect CSI, the required bits for feedback of channel states to the users reduces from 16 symbols to 5 bits and that the required computational complexity reduces from the order of $O(2^k)$ to $O(k)$ with K users by the simple quantized modified estimation.

Figure 4 compares average SEs of MCCDMA system using Walsh and OCC codes with and without constellation movement scheme against SNR. The SEs for Walsh code cannot be improved further beyond some high SNR due to the excessive interferences. Obviously, the SE of the MCCDMA system using OCC code outperforms that using the Walsh codes. This improvement in SE is obtained jointly by the chip width of the chip based spreading modulation through increased processing gain and the desirable correlation properties of OCC code. The MCCDMA system using constellation movement scheme outperforms that using OCC code without this scheme. This scheme achieves SNR gain of 2 dB compared to system using OCC code and of 4 dB compared to system using Walsh code for achieving an average SE of 1.8 bits/ch.use (90%). This is certainly obtained through adaptive control of position of the constellation angle against random constellation. This result shows significant improvement of SE due to interference mitigation efficiency of the proposed adaptive constellation movement scheme.

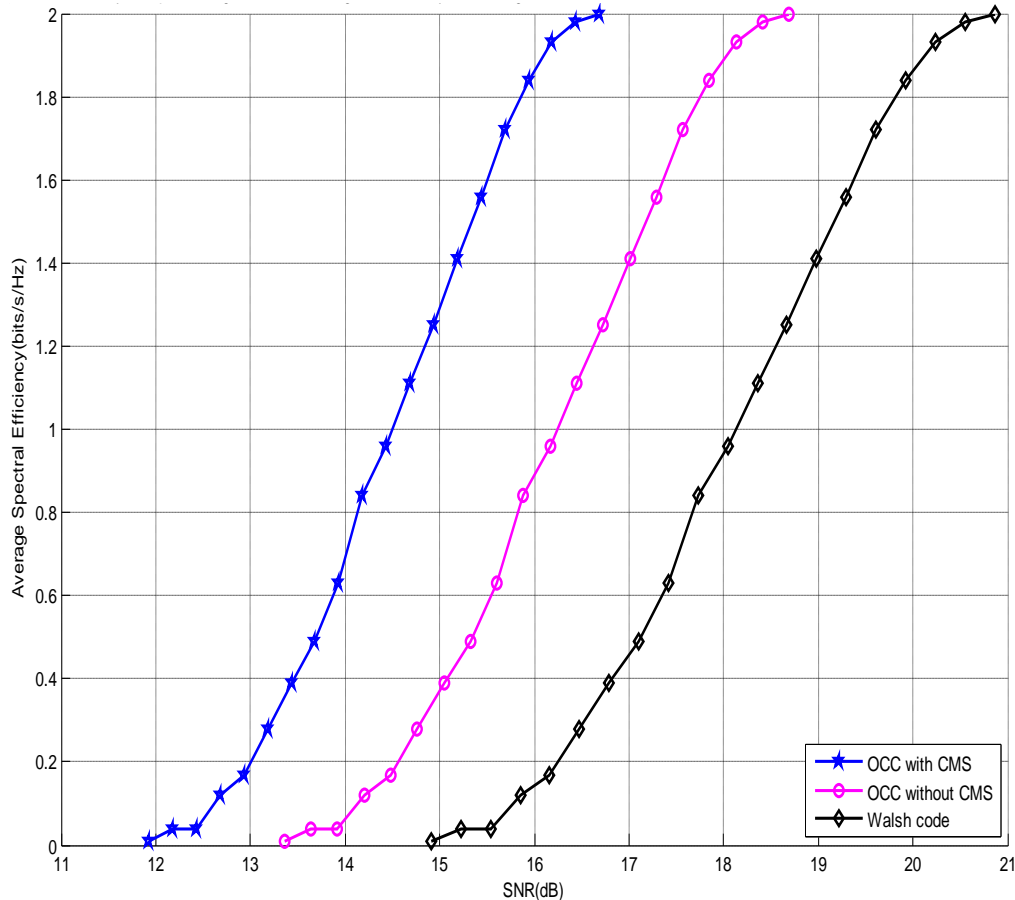


Figure 4. Spectral Efficiency comparison against SNR among MCCDMA system using Walsh and OCC codes with and without constellation movement scheme.

The modified MCCDMA and constellation movement scheme have several advantages compared to conventional MCCDMA systems with unitary spreading codes. The robustness to difficult multipath channel and interference mitigation efficiency are increased. The SE improvement and reduced error rate are achieved.

On the other hand, complexity of the system is increased. However, the complexity of the simple quantized estimation is reduced compared to the perfect CSI. Generally, the complexity of estimation scheme increases for large constellations if the required CSI is large, which implies that the constellation movement scheme might be feasible for the scenario intended for large signaling constellations.

Moreover, it is power efficient because it does not require extra power to control the constellation angle adaptively in the proposed constellation movement scheme where only the phase is changed with same amplitude.

Conclusion

In this paper, the modification of MCCDMA system is

studied for ideal correlation properties and maximum channel diversity gain to solve the problem of loss of orthogonality among the users due to MAI in frequency selective fading channel in order to increase the user capacity. The constellation movement scheme is proposed in the MCCDMA system to recover the overlapped symbols due to random constellation caused by MAI at particular channel conditions in order to increase the SE and the user capacity. The performance of modified MCCDMA and constellation movement scheme are evaluated in terms of BER and SE and it outperforms the conventional MCCDMA systems. The interference mitigation efficiency of the system improved against the frequency selective fading effects by the orthogonality of the OCC codes and OCC encoding of the modified MCCDMA system and by the adaptive control of random constellation in the constellation movement scheme. The system robustness to multipath effects improved by combined quantized estimation and adaptive control of random constellation in the constellation movement scheme and correlation properties of OCC codes. Furthermore, the issues for modification of MCCDMA system, procedure for simple quantized

estimation, procedure to compute the optimal angle for movement are given. Design criterions such as condition for singular channel fade states; minimum distance threshold and condition to avoid overlapping with other channel states for MQAM signal set are developed. Thus, this modified MCCDMA system has MAI-free capability regardless of the number of users and so, the user capacity is increased.

Conflict of Interests

The author(s) have not declared any conflict of interests.

REFERENCES

- Abdulhamid Z, Hamidreza B (2013). Novel MAI reduction method using longer m-sequences for multiuser detection in DS/CDMA communication systems. *Int. J. Commun.* 2(1):12-20.
- Alamouti SM (1998). A simple transmit diversity technique for wireless communications. *IEEE J. Sel. Areas Commun.* 16(8):1451-1458. <http://dx.doi.org/10.1109/49.730453>
- Chen HH, Chiu HW, Guizani M (2006). Orthogonal complementary codes for interference free CDMA technologies. *IEEE Wireless Commun.* 13(1):68-79. <http://dx.doi.org/10.1109/MWC.2006.1593527>
- El-Hajjar M, Lajos H (2010). Multifunctional MIMO systems: A combined diversity and multiplexing design perspective. *IEEE Commun. Mag.* pp. 73- 79.
- Fazel K, Kaiser S (2008). *Multi-Carrier and Spread Spectrum System*. 2nd edn. John Wiley and Sons. <http://dx.doi.org/10.1002/9780470714249>
- Hara S, Prasad R (1999). Design and performance of multicarrier CDMA system in frequency selective Rayleigh fading channels. *IEEE Trans. Vehicular Technol.* 48(5):1584-1595. <http://dx.doi.org/10.1109/25.790535>
- Jing Li, Aiping H, Mohsen G, Chen HH (2008). Inter-Group complementary codes for interference-resistant CDMA wireless communications. *IEEE Trans. Wireless Commun.* 7(1):166-174.
- Koike-Akino T, Popovski P, Tarokh V (2009). Optimized constellation for two-way wireless relaying with physical network coding. *IEEE J. Sel. Areas Commun.* 27:773-787. <http://dx.doi.org/10.1109/JSAC.2009.090617>
- Kugalur MP, Veerappa GP (2013). The optimistic adaptive modulation technique for future wireless communication. *J. Comput. Sci.* 9(4):500-513. <http://dx.doi.org/10.3844/jcssp.2013.500.513>
- Li Y, Huang YW (2009). New QAM Golay sequences with unequal sequence power. *IEEE Int. Symp. Inf. Theory Seoul*.
- Mario ME, Thunyawat R, Daniel H, Hsiao HC (2007). Design of an MC-CDMA system that uses complete complementary orthogonal spreading codes. *IEEE Trans. Vehicular Technol.* 56(5):2976-2989. <http://dx.doi.org/10.1109/TVT.2007.900359>
- Musavian L, Aissa S, Lambotharan S (2011). Adaptive Modulation in Spectrum-Sharing Channels Under Delay Quality-of-Service Constraints. *IEEE Trans. Vehicular Technol.* 60(3):901-911. <http://dx.doi.org/10.1109/TVT.2010.2097282>
- Varzakas P (2007). Optimization of an OFDM Rayleigh fading system. *International J. Commun. Syst.* 20(1):1-7. <http://dx.doi.org/10.1002/dac.807>
- Verdu S (1998). *Multiuser detection*. Cambridge University Press.
- Wei XM, Si YS, Hsiao-Hwa C, Jin Qiang L (2013). Multi-user interference cancellation in complementary coded CDMA with diversity gain. *IEEE Wireless Commun. Lett.* 2(3):303-306. <http://dx.doi.org/10.1109/WCL.2013.030613.130016>
- Ye S, Blum RS, Cimini LJ (2006). Adaptive OFDM systems with imperfect channel state information. *IEEE Trans. Wireless Commun.* 5(11):3255-3265. <http://dx.doi.org/10.1109/TWC.2006.05004>

Full Length Research Paper

Sorption mechanism of some heavy metal ions from aqueous waste solution by polyacrylamide ferric antimonate

I. M. El-Naggar¹, E. A. Mowafy¹, Y. F. El-Aryan¹ and M. G. Abd El-Wahed^{1,2*}

¹Atomic Energy Authority, Hot Laboratories Center, P. No. 13759, Cairo, Egypt.

²Chemistry Department, Faculty of Science, Zagazig University, Egypt.

Received 30 December, 2013; Accepted 12 March, 2014

Incorporation of a polymer material into an inorganic ion exchanger provides a class of hybrid ion exchangers with a good ion exchange capacity, high stability and high selectivity for heavy metals. We can see these properties in the present study. The kinetic of Fe (III), Pb (II), Cd (II), Cu (II), and Zn (II) ions on polyacrylamide ferric antimonate has been studied. The thermodynamic parameters such as activation energy (E_a), entropy of activation ΔS^* and diffusion coefficient (D_o) have been evaluated and a correlation has been made of these parameters with the ion exchange characteristics of the material.

Key words: Synthesis, polyacrylamide ferric antimonite, adsorption, isotherm, diffusion, heavy metals.

INTRODUCTION

In recent years, the search for a new class of high performance and high functional organic-inorganic composite ion-exchangers were developed by the incorporation of organic conducting polymers into inorganic precipitates (Khan et al., 2003, 2003; Khan and Alam, 2004). Heavy metals contamination exists in aqueous waste stream from many industries such as metal plating, mining, tanneries, and painting, car radiator manufacturing, as well as agricultural sources where fertilizers and fungicidal spray were intensively used. The removal of heavy metal in an effective manner from water and waste water is, thus, ecologically very important. There are many reported and established technologies for the recovery of metals from waste water, which include chemical precipitation, flotation, electrolytic recovery, membrane separation and activated carbon adsorption. In recent years, the search for a new class

of high performance and high functional organic-inorganic composite ion-exchangers were developed by the incorporation of organic conducting polymers into inorganic precipitates (Khan et al., 2004). These materials were found selective for heavy toxic metal ions and utilized for analysis of water pollution as such materials have a great deal of attention because of their special mechanical and chemical stabilities (Khan et al., 2004). The newly developed composite offered a high capacity and faster sorption kinetics for the metal ions such as Fe (III), Pb (II), Cd (II), Cu (II), and Zn (II) ions.

EXPERIMENTALS

Materials

All chemicals used in this work were of analytical grade and used

*Corresponding author. Email: mabdelamid@yahoo.com. Fax: 202-462-0608.

Author(s) agree that this article remain permanently open access under the terms of the [Creative Commons Attribution License 4.0 International License](http://creativecommons.org/licenses/by/4.0/)

without further purification.

Preparation of polyacrylamide

Polyacrylamide was prepared by mixing equal volume of 20% acrylamide prepared in distilled water with 0.1 M potassium persulfate ($K_2S_2O_8$) prepared in 1 M HCl, a viscous solution was obtained by heating the mixture gently at $70 \pm 5^\circ\text{C}$ with continuous stirring.

Preparation of ferric antimonate

Ferric antimonate prepared from 0.5 M of ferric chloride was dissolved in distilled water and adding the same volume of 0.5 M antimony metal dissolved in aqua regia slowly with constant stirring using a magnetic stirrer at a temperature of $70 \pm 5^\circ\text{C}$. The resulting solution was precipitated by using ammonia solution drop by drop until the pH was about 0.13. This results in formation of red brown precipitate.

Preparation of polyacrylamide ferric antimonate

Polyacrylamide ferric antimonate was formed by adding a precipitate of ferric antimonate to polyacrylamide with stirrer by using magnetic stirrer to obtain homogenous precipitate. The precipitates were left to age in the mother liquor overnight, the precipitate was washed with distilled water several times. The supernatant liquid was decanted and the gel filtered using a centrifuge (about 10^4 rpm) and dried at $50 \pm 1^\circ\text{C}$. The product was crashed and sieved to obtain different mesh sizes of 0.12 to 1.00 mm. The weight loss of polyacrylamide ferric antimonate in the different forms such as H(I), Pb (II), Fe (III), Cd (II), Cu (II) and Zn (II) ions at 1000°C were determined using thermal analysis technique (TG and DTA) to be 34.9, 17.33, 19.81, 21.55, 21.22 and 21.33% w/w, respectively.

Chemical stability

Chemical stability of polyacrylamide ferric antimonate ion exchangers were studied in water, nitric and hydrochloric acid [1, 2, 3, 4, 5 and 6 M], as well as in potassium and sodium hydroxide (0.1, 1 M) by mixing 50 mg of ion exchanger samples and 50 ml of the desired solution with intermittent shaking for approximately three weeks at $25 \pm 1^\circ\text{C}$.

Data analysis

Pb (II), Fe (III), Cd (II), Cu (II) and Zn (II) ions were measured using ICPS-7500 and atomic absorption flame emission spectrophotometer (AA- 6701F).

RESULTS AND DISCUSSION

The ion exchange capacity of polyacrylamide ferric antimonate for Pb (II), Fe (III), Cd (II), Cu (II) and Zn (II) ions were found to be 5.33, 4.31, 3.12, 2.51 and 2.35 respectively. It is indicated that the affinity sequence for all cations is $\text{Pb}^{2+} > \text{Fe}^{3+} > \text{Cu}^{2+} > \text{Cd}^{2+} > \text{Zn}^{2+}$. This trend may be due to the electronegativity of $\text{Pb}^{2+} > \text{Fe}^{3+}$, Cu^{2+} , Cd^{2+} and Zn^{2+} and may be due to the hydrated ionic radii

according to the fact that increasing atomic number results in decreasing hydrated ionic radii (Abou-Mesalam and El-Naggar, 2003).

The effect of particle sizes on the rate of exchange of Pb (II), Fe (III), Cd (II), Cu (II) and Zn (II) ions on polyacrylamide ferric antimonate was studied at $25 \pm 1^\circ\text{C}$. Straight lines passing through the origin are obtained, which were taken as indication of a particle diffusion mechanism as shown in Figure 1. The results and figures of Lead were taken as example for the sake of brevity), a relation between F and Bt against time. Similar trend was observed by El-Naggar et al. (2007, 2012).

The plots of Bt and F against t for the exchange of Pb (II), Fe (III), Cd (II), Cu (II) and Zn (II) ions at different reaction temperatures (25, 45 and $65 \pm 1^\circ\text{C}$) on polyacrylamide ferric antimonate are presented in Figure 2. The results and figures of Lead were taken as example for the sake of brevity). straight lines were observed to be passing through the origin. This confirms that the phenomenon is particle diffusion controlled, and the rate of exchange increases by increasing the reaction temperatures from 25 to $65 \pm 1^\circ\text{C}$. The relatively small activation energy values (E_a) obtained in Table 1, for Pb (II), Fe (III), Cd (II), Cu (II) and Zn (II) ions, indicated that the rate of exchange is particle diffusion mechanism (El-Naggar et al., 2012).

Adsorption isotherm

The Langmuir adsorption isotherm assumes that adsorption takes place at specific homogeneous sites within the adsorbent and has found successful applications in many adsorption processes of monolayer adsorption. For the case of adsorption in solution, the equation is represented by the following (Langmuir, 1916).

$$\frac{C_e}{q_e} = \frac{1}{q_{\max} k_L} + \frac{C_e}{q_{\max}}$$

Where q_e (mol g^{-1}) is the adsorption capacity for Pb(II), Fe(III), Cd(II), Cu(II) and Zn(II) ions on the adsorbent at the equilibrium, C_e (mol dm^{-3}) is the equilibrium ions concentration in the solution, q_{\max} is the monolayer adsorption capacity of the adsorbent, and k_L is the Langmuir adsorption constant. The plots of C_e/q_e vs. C_e for the adsorption of Pb(II) ion onto composite Figure 3 give a straight line of the slope $\frac{1}{q_{\max}}$ and intercept $\frac{1}{q_{\max} k_L}$.

We took the results and figures of lead as example for the sake of brevity. The Freundlich isotherm is an empirical equation employed to describe heterogeneous systems The plot of $\ln K_L$ vs. $1/T$ for Pb(II), Fe(III), Cd(II), Cu(II) and Zn(II) ions is given in Figure 4. Accordingly the values of ΔH at saturation are calculated

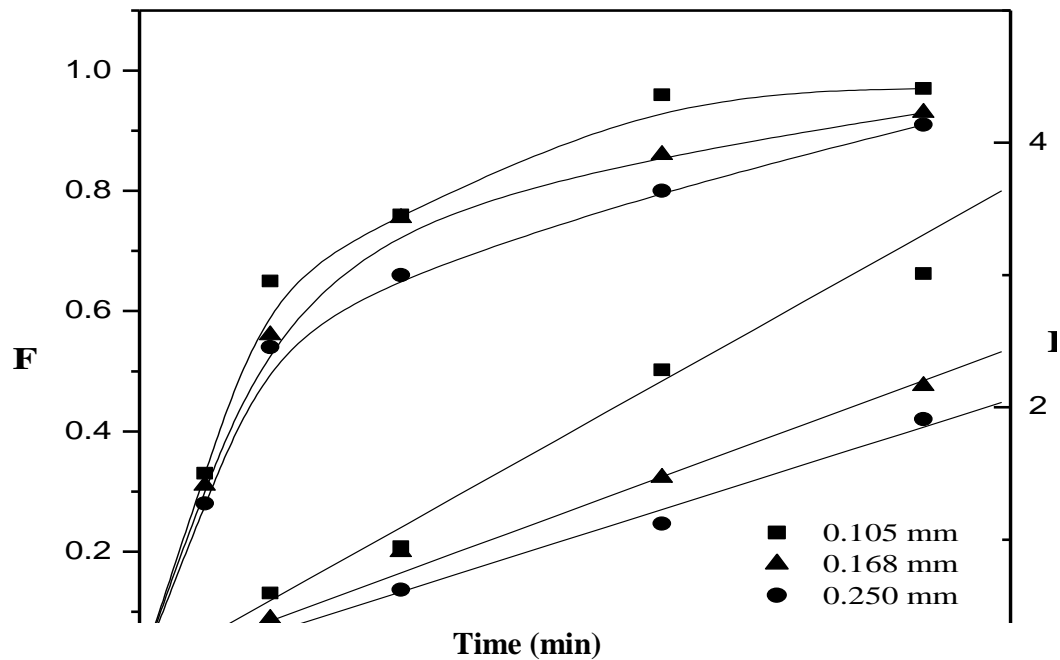


Figure 1. Plots of F and Bt against time for exchange of Pb(II) on polycrylamid ferric antimonate at different particle diameters.

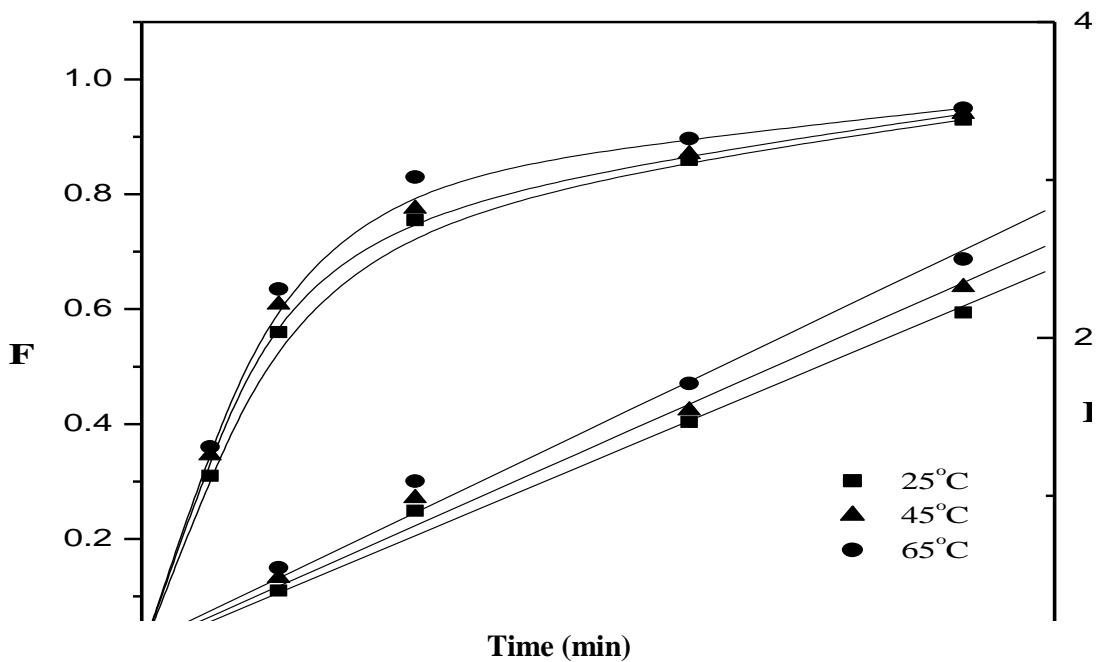
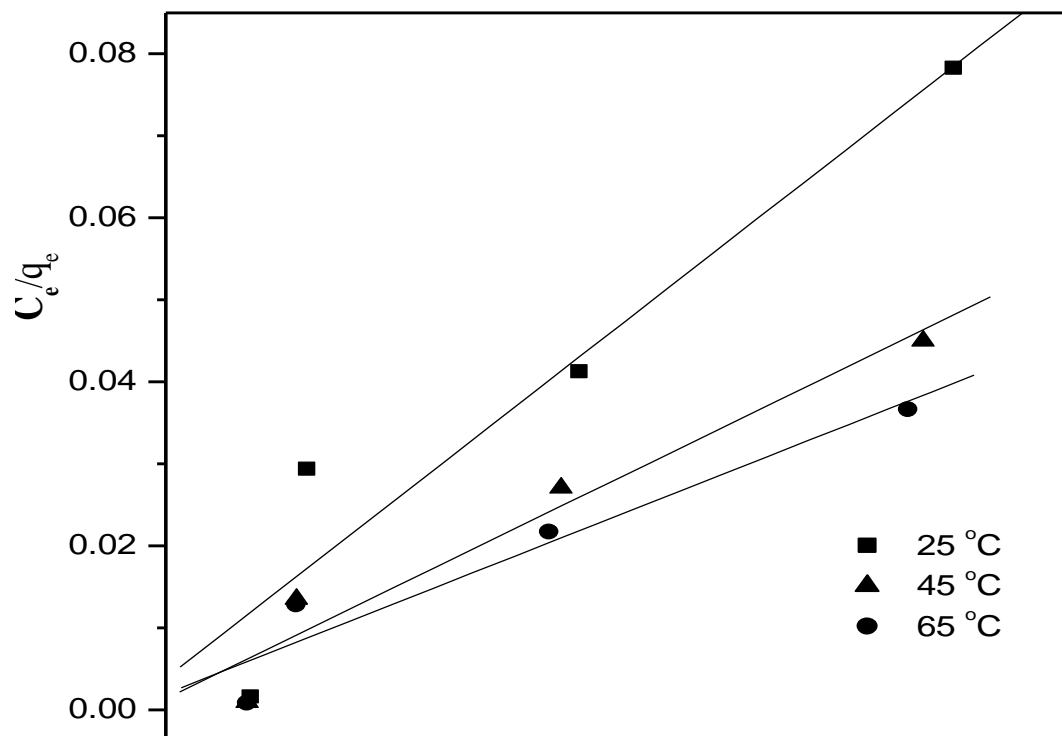


Figure 2. Plots of F and Bt against time for exchange of Pb(II) on polycrylamid ferric antimonate at different reaction temperatures.

Table 1. Thermodynamic parameters for the exchange of Fe³⁺, Pb²⁺, Cd²⁺, Cu²⁺, and Zn²⁺ on polyacrylamide ferric antimonate, at different reaction temperatures.

Metal ion	Reaction temperature	$D_i \times 10^8$ (cm ² s ⁻¹)	$D_o \times 10^5$ (cm ² s ⁻¹)	E_a (KJ mol ⁻¹)	ΔS^* (mol ⁻¹ k ⁻¹)
Pb(II)	25	0.57	1.83	2.86	-121
	45	0.61	1.82		-122.3
	65	0.65	1.83		-122.8
Cd(II)	25	0.59	3.44	4.37	-116.4
	45	0.67	3.54		-116.8
	65	0.73	3.44		-117.6
Zn(II)	25	0.59	3.8	4.56	-115.7
	45	0.69	3.89		-116
	65	0.75	3.8		-116.8
Cu(II)	25	0.81	8.55	6.27	-107.2
	45	1.04	9.3		-107.4
	65	1.08	8.56		-108.6
Fe(III)	25	0.44	17.9	9.14	-102.8
	45	0.62	20.04		-102.4
	65	0.67	17.9		-103.9

**Figure 3.** Plots of C_e / q_e against C_e for exchange of Pb(II) on polyacrylamid ferric antimonate at different reaction temperatures.

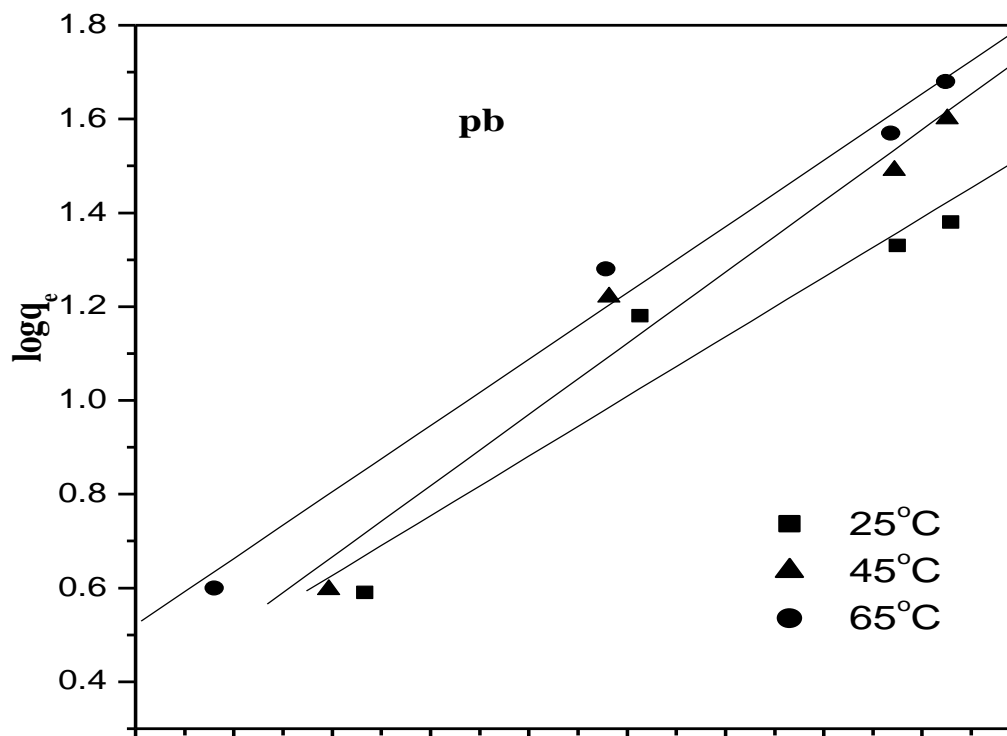


Figure 4. Freundlich adsorption isotherm for the sorption of Fe(III), Pb(II), Cd(II), Cu(II) and Zn(II) ions on polyacrylamid ferric antimonate at different reaction temperatures.

for Pb(II), Fe(III), Cd(II), Cu(II) and Zn(II) ions on polyacrylamide ferric antimonate and represented in the Table 2. These values indicate the exothermic behavior of polyacrylamide ferric antimonate. The linearized form of the Freundlich isotherm equation (Freundlich, 1906) is.

$$\log q_e = \log k_F + \frac{1}{n} \log C_e$$

Where K_F ($\text{dm}^3 \text{g}^{-1}$) and n (dimensionless) are Freundlich adsorption isotherm constants, being indicative of the extent of the adsorption and the degree of nonlinearity between solution concentration and adsorption, respectively.

The free energy ΔG° were associated to the adsorption process and were determined using the following equation

$$\Delta G^\circ = -RT \ln K_L$$

The results given in Table 2 show that the change of free energy for physisorption is generally between -20 and 0 kJ mol^{-1} ; the physisorption together with chemisorption is at the range of -20 to -80 kJ mol^{-1} and chemisorptions is

at a range of -80 to -400 kJ mol^{-1} (Jaycock and Parfitt, 1981). The negative value of the enthalpy change of Pb(II) ion indicates an exothermic behavior; the positive value of the enthalpy change indicates that the adsorption process is endothermic and this value also indicates that the adsorption follows a physisorption mechanism in nature involving weak forces of attraction between the adsorbed [Pb(II), Fe(III), Cd(II), Cu(II) and Zn(II)] ions and composite, thereby demonstrating that the adsorption process is stable energetically (Yu et al., 2001). The Freundlich constant n is a measure of the deviation from linearity of the adsorption. If a value for n is below unity, this implies that adsorption process is governed by a chemical mechanism; however, if a value for n is above unity, adsorption is favorably a physical process. The K_F and n were calculated from the slopes of the Freundlich plots as shown in Figure 4. The results and figures of Lead were taken as example for the sake of brevity) and were found to be (1.64 to 2.57) and (2.70 to 4.76) respectively. The magnitudes of K_F and n show easy separation of heavy metal ion from wastewater and high adsorption capacity (Saifuddin and Raziah, 2007). The value of n , which is related to the distribution of bonded ions on the sorbent surface, represent beneficial adsorption if it is between 1 and 10 (Kadirvelu and

Table 2. Isotherm parameters for adsorption of Pb (II), Fe (III), Cd (II), Cu (II) and Zn (II) ions on polyacrylamid ferric antimonate.

Elements	Langmuir		Freundlich	
	ΔH (KJ/mol)	ΔG° (KJ/mol)	K_F	n
Pb	-3.34	-10.33	1.64	4.76
Fe	21.17	-10.55	2.57	2.33
Cu	8.09	-9.98	1.87	2.77
Cd	32.5	-10.60	1.67	3.45
Zn	14.78	-11	1.84	2.70

Namasivayam, 2000; Solener et al., 2008). The values of n at equilibrium represents favorable adsorption at studied temperatures and therefore this would seem to suggest that a physical mechanism, referred to as the adsorption bond becomes weak (Jiang et al., 2002) and conducted with van der Waals forces. Table 2 gives the isotherm parameters for both Langmuir and Freundlich isotherms. From these parameters of the adsorption isotherm, it was noted that the Freundlich isotherm model exhibits better data than the Langmuir isotherm model.

Conclusion

The present study shows that polyacrylamide ferric antimonate is an effective adsorbent for the removal of Pb(II), Fe(III), Cd(II), Cu(II) and Zn(II) ions from aqueous solutions. The following results have thus been obtained:

- 1) Polyacrylamide ferric antimonate has a good ion exchange capacity, high stability and high selectivity for Pb(II) and Fe(III) than Cd(II), Cu(II) and Zn(II) ions.
- 2) The adsorption follows a physisorption mechanism in nature involving weak forces of attraction between the adsorbed [Pb(II), Fe(III), Cd(II), Cu(II) and Zn(II)] ions and polyacrylamide ferric antimonite.
- 3) It was noted that the Freundlich isotherm model exhibits better data than the Langmuir isotherm model.

Conflict of Interests

The author(s) have not declared any conflict of interests.

ACKNOWLEDGEMENTS

The authors are thankful to Prof. El-Naggar, Head of Hot Laboratory Center and Prof. Abd El-Wahed, Dean of Faculty of Science, Zagazig University, Egypt.

REFERENCES

Abou-Mesalam MM, El-Naggar IM (2003). Diffusion mechanism of Cs⁺, Zn²⁺ and Eu³⁺ ions in the particles of zirconium titanate ion exchanger

using radioactive tracers. Eng. Aspects. 215:205. [http://dx.doi.org/10.1016/S0927-7757\(02\)00443-0](http://dx.doi.org/10.1016/S0927-7757(02)00443-0)

El-Naggar IM, Mowafy EA, Abdel-Galil EA (2007). Diffusion mechanism of certain fission products in the particles of silico(IV)titanate. Coll. Surf. A: Physicochem. Eng. Aspects 307:77. <http://dx.doi.org/10.1016/j.colsurfa.2007.05.004>

El-Naggar IM, Mowafy EA, El-Kenany WM (2010). Kinetics and adsorption isotherm of some heavy metal ions from aqueous waste solutions by crystalline antimonite acid. Arab. J. Nucl. Sci. Appl. 43(2):97-106.

El-Naggar IM, Zakaria ES, Ali IM, Khalil M, El-Shahat MF (2012). Kinetic modeling analysis for the removal of cesium ions from aqueous solutions using polyaniline/titanate. Arabian J. Chem. 5:109-119. <http://dx.doi.org/10.1016/j.arabjc.2010.09.028>

Freundlich HMF (1906). Über die adsorption in losungen. Z. Phys. Chem. 57:385.

Jaycock MJ, Parfitt GD (1981). Chemistry of Interfaces. Ellis Horwood Ltd., Onichester, P. 625.

Jiang J-Q, Cooper C, Ouki S (2002). Comparison of modified montmorillonite adsorbents — Part I: Preparation, characterization and phenol adsorption. Chemosphere 47:711. [http://dx.doi.org/10.1016/S0045-6535\(02\)00011-5](http://dx.doi.org/10.1016/S0045-6535(02)00011-5)

Kadirvelu K, Namasivayam C (2000). Agricultural by-products as metal adsorbents: Sorption of lead (II) from aqueous solutions onto coir-pith carbon. Environ. Technol. 21:1091. <http://dx.doi.org/10.1080/09593330.2000.9618995>

Kadirvelu K, Namasivayam C (2000). Agricultural by-products as metal adsorbents: Sorption of lead (II) from aqueous solutions onto coir-pith carbon. Environ. Technol. 21:1091. <http://dx.doi.org/10.1080/09593330.2000.9618995>

Khan AA, Alam MM, Inamuddin (2004). Preparation, characterization and analytical applications of a new and novel electrically conducting fibrous type polymeric-inorganic composite material: Polypyrrole/Th(IV) phosphate used as a cation-exchanger and Pb(II) ion-selective membrane electrode. Mater. Res. Bull. 40:289. <http://dx.doi.org/10.1016/j.materresbull.2004.10.014>

Khan AA, Alam MM, Inamuddin, Mohammad F (2004). Electrical conductivity and ion-exchange kinetic studies of a crystalline type 'organic-inorganic' cation-exchange material: Polypyrrole/polyantimonite acid composite system (Sb₂O₅) (–C₄H₂NH–) • nH₂O. Electroanal. Chem. 572:67.

Khan AA, Alam MM, Mohammad F (2003). Ion-exchange kinetics and electrical conductivity studies of polyaniline/Sn(IV) tungstoarsenate; (SnO₂)(WO₃)(As₂O₅)₄(–C₆H₅–NH–)₂•nH₂O: A new semi-crystalline 'polymeric-inorganic' composite cation-exchange material. Electrochim. Acta, 48 (2003) 2463. [http://dx.doi.org/10.1016/S0013-4686\(03\)00272-X](http://dx.doi.org/10.1016/S0013-4686(03)00272-X)

Langmuir I (1916). The adsorption of gases on plansurfaces of glass, mica and platinum. J. Am. Chem. Soc. 40:2221-2295. <http://dx.doi.org/10.1021/ja02268a002>

Solener M, Tunali S, SafaOzcan A, Ozcan A, Gedikbey T (2008). Adsorption characteristics of lead(II) ions onto the clay/poly(methoxyethyl)acrylamide (PMEA) composite from aqueous solutions; Desalination. 223:308-322. <http://dx.doi.org/10.1016/j.desal.2007.01.221>

Yu Y, Zhuang YY, Wang ZH (2001). Adsorption of water-soluble dye onto functionalized resin. *J. Coll. Interf. Sci.* 242:288. <http://dx.doi.org/10.1006/jcis.2001.7780>
Yusan S, Gok C, Erenturk S, Aytas S (2012). Adsorptive removal of

thorium (IV) using calcined and flux calcined diatomite from Turkey: Evaluation of equilibrium, kinetic and thermodynamic data. *Appl. Clay Sci.* 67-68:106–116. <http://dx.doi.org/10.1016/j.clay.2012.05.012>



Related Journals Published by Academic Journals

- International NGO Journal
- International Journal of Peace and Development Studies